AD-A252 435

Spring 1992   THESIS/DISSERTATION

Initiation and Development of Creeping Thermal Plumes

①

David L. Coulliette, Major

AFIT Student Attending: Florida State University   AFIT/CI/CIA- 92-003D

AFIT/CI
Wright-Patterson AFB OH 45433-6583

Approved for Public Release IAW 190-1
Distributed Unlimited
ERNEST A. HAYGOOD, Captain, USAF
Executive Officer

92-17916

92 7 0   0 0 9

111

THE FLORIDA STATE UNIVERSITY

COLLEGE OF ARTS AND SCIENCES

INITIATION AND DEVELOPMENT OF CREEPING THERMAL PLUMES

By

DAVID L. COULLIETTE

A dissertation submitted to the Department of Mathematics
in partial fulfillment of the requirements for the degree of
Doctor of Philosophy

Degree Awarded:
Spring Semester, 1992

The members of the Committee approve the dissertation of David

L. Coulliette defended on 7 January 1992.

David E. Loper
Professor Directing Dissertation

Manfred Koch
Outside Committee Member

Louis N. Howard
Committee Member

Steven L. Blumsack
Committee Member

I. M. Navon
Committee Member

Table of Contents

Acknowledgements

I wish to express my gratitude to Professor D. Loper for his guidance and friendship during my graduate study at the Florida State University. His exceptional curiosity and unselfish assistance will serve as a continuing model for me in my academic life.

I am also grateful to Professor M. Koch for his extensive assistance in my numerical work. It would have been very difficult for me to complete my degree without his direction. I thank Professor L. Howard, Professor S. Blumsack, and Professor I. M. Navon for their kindness in sitting in the committee. Their comments and suggestions are deeply appreciated.

I want to thank the Geophysical Fluid Dynamics Institute for laboratory and computer support, and the Antarctic Marine Research Facility for providing space for my experiment. R. Gaetano and G. Arnold provided invaluable assistance in performing the experiments. Professor J. Telotte of the Department of Chemical Engineering assisted me in developing a model for viscosity.

Finally, I wish to thank my family and all of my friends in Tallahassee for their encouragement, moral support, and prayers during my program of study.

List of Tables

List of Figures

ABSTRACT

The study of the formation and growth of thermal plumes is motivated by the proposed existence of such plumes in the Earth's mantle. During the initial stages of plume development, a plume consists of a large buoyant ball trailing a narrow feeder conduit. This study presents laboratory, analytical, and numerical models of this flow. The experimental model generates the plumes using a heater in a syrup whose viscosity is highly temperature-dependent. The resulting data provides a measure of the effectiveness of the analytical and numerical models. The analytical model, based on mass and energy conservation, shows a significant improvement in the flow prediction compared to previous models. The numerical model uses the finite-element method to produce a flow solution that successfully predicts the flow to within the experimental error.

CHAPTER 1

INTRODUCTION AND LITERATURE REVIEW

1.1 Introduction

The initiation and development of creeping thermal plumes in a medium whose viscosity is highly temperature-dependent presents an interesting and challenging problem in low Reynolds number flow. The problem gains increased significance, however, when considering the application of such flow to geophysical fluid dynamics and mantle convection.

Three methods of investigation were used to research this problem: experimental, numerical, and analytical. A brief description of the experimental apparatus will serve to provide a concrete example of the problem. A large container was filled with a thick corn syrup whose viscosity varies greatly with temperature. A small heater placed in the bottom of the container provided the heat input to generate a thermally buoyant plume which formed with a balloon-on-a-string shape (figures 4c, 5c). We call this plume structure a starting plume. The goal of this project was to predict analytically and numerically the motion of the fluid in the tank. Of particular interest was the rise time of the plume.

This problem provides a first-approximation model of deep Earth-mantle plumes. Morgan (1971) first proposed the existence of mantle plumes extending from the deep mantle to the asthenosphere. While several regions have been suggested as the source of mantle plumes, the most plausible appears to be the D" layer (Stacey and Loper, 1983). Seismic studies have identified the D" layer as a distinct layer at

1

the base of the mantle. Yuen and Peltier (1980) used linear stability analysis to show that for a wide range of conditions, the D" layer is dynamically unstable. They postulated that this instability could evolve into deep mantle plumes. Stacey and Loper (1983) modelled the D" layer as a dynamically active layer with a flow pattern that is distinct from that in the lower mantle. This layer, maintained by the heat flux from the core, provides a source of buoyant, low viscosity fluid for plume activity. At the high pressures and temperatures in the Earth's interior, the rock-like mantle exhibits fluid properties. A key characteristic of the mantle material is its highly temperature-dependent viscosity. The corn syrup in the experimental tank, then, represents the Earth's mantle. The heater is the core and the heated fluid layer just above the heater is the D" layer. While this crude model neglects many complicating factors such as a stably-stratified mantle, this problem serves as a good initial step in the solution of the larger, more complicated problem.

1.2 Literature Review

Most of the previous work has concentrated on specific aspects of the problem of plume initiation and growth; few have attempted to integrate these aspects. The efforts may be grouped into two categories: experimental/analytical investigations and numerical investigations.

1.2.1 Experimental/Analytical Investigations

The earliest experimental/analytical effort appears to be that of Whitehead and Luther (1975). Many of the results were summarized in Whitehead (1986). Their experiment involved injecting a less dense, less viscous fluid into a denser, more viscous fluid. The viscosity contrast (μ_{large}/μ_{small}) of the two fluids was 6 x 10^3. They found that a ball formed on the spout of the injector, and then lifted off from the spout, trailing a thin feeder conduit. This structure is very similar to that

observed in the research experiment. One key difference in the experiments is that Whitehead and Luther (1975) used two immiscible fluids, so no diffusion occurred. They developed an analytical model for speed, height and radius of the ball of the plume as a function of time, which predicts that height varies as $t^{5/3}$. Their experimental results showed good quantitative agreement with the model.

A similar study is that of Olson and Singer (1985). They also continuously injected a less dense, less viscous fluid into a more viscous, denser fluid, but they formed the less dense fluid by diluting the denser fluid (glucose syrup) with water forming a plume of miscible fluid. They found experimentally that height varied as $t^{7/5}$ and that the plume rose slower than for the Whitehead and Luther (1975) case. This slower rate may be due to diffusion. Note that the compositional diffusion of the Olson and Singer (1985) experiment is very slow relative to the thermal diffusion of the experiment in the current study.

Diffusion of buoyancy is a key factor in the thermal plume problem, as indicated in the research of Morris (1982) and Ansari and Morris (1985). These studies isolated the effects of strongly temperature-dependent viscosity on slow flow past a rigid sphere. These investigations were motivated by the observation that a sphere of hot magma would require a time equivalent to the Earth's age to move through the lithosphere in a Stokes-flow regime. Morris showed that if a rigid sphere is maintained at a high temperature in a medium with highly temperature-dependent viscosity, then it will transfer heat to the surrounding medium and create a lower viscosity path for the sphere to follow. In this 'lubrication limit', the sphere moves faster than in Stokes flow. In fact, Morris found for the lubrication limit that a smaller sphere rises faster than a larger sphere, an effect opposite to Stokes flow. This result was confirmed experimentally by Ribe (1983). Ribe also determined that the ascent speed will increase by 25% (for Stokes flow) to 100% (lubrication limit)

for each order-of-magnitude change in viscosity contrast. These results show that a sphere of magma would rise faster than predicted by Stokes flow, if the temperature of the sphere were constant. In reality, such a sphere would cool quickly and stop its upward motion.

Griffiths (1986a-d) made an experimental investigation that also concentrated on the effects of diffusion. In contrast to the continuously injected plumes of Whitehead and Luther (1975) and Olson and Singer (1985), he injected a fixed volume of warmer oil into a larger container of the same oil at a lower temperature. These 'thermals' grew in size due to entrainment of the ambient fluid, while the speed decreased with time. By assuming that all of the heated ambient fluid is entrained (i.e., buoyancy is conserved), Griffiths developed analytical expressions indicating that height varied as $t^{1/2}$ and speed varied as $t^{-1/2}$. This rise law agreed qualitatively and quantitatively with his experimental results.

Recent work by Griffiths and Campbell (1990) more closely models the proposed experimental study. This work also represents the first attempt to integrate all aspects of the thermal-plume problem. They injected a continuous stream of warmer, less viscous fluid into an overlying layer of more dense, more viscous fluid. By assuming that all of the heated ambient fluid is entrained, they developed a rise law predicting that the height of the plume would vary as $t^{5/4}$. Although this assumption is not physically realistic, they stated that this rise law adequately predicted their experimental results, but presented no data to support this statement.

1.2.2 Numerical Investigations

Just as the previous experimental/analytical work isolated various factors of the plume flow, much of the numerical work emphasized selected physical phenomena. Some of the numerical work, however, attempts to attack the full problem in methods similar to the proposed research. Table 1 summarizes the

Table 1. Comparison of related numerical studies.

Name	Scheme	Domain	Ra	μ_c/μ_h	Note
Parmentier (75)	FDM	axisym	10^6	10^2- 10^6	steady state
Daly and Raefsky (85)	FEM	axisym	0	10^6	rigid sphere
Schubert and Anderson (85)	FEM	planar	107	n/a	constant viscosity
Jarvis (84)	FDM	planar	10^8	n/a	constant viscosity
Boss and Sacks (85)	FDM	planar	10^7	20	stream funct- ion
Olson, Schubert, Anderson (87)	FEM	planar	10^4	10^3- 10^4	
Zhao and Yuen (87)	FEM	planar axisym	10^7	100	viscous heating

characteristics of previous related numerical work. Both finite-difference methods and finite-element studies are described in the literature. In general, the more recent works prefer the finite-element method due to the grid flexibility which allows high resolution in the boundary layers that commonly occur in such flows. Sato and Thompson (1976) discuss some of the specific advantages of the finite-element method for this application. Parmentier, et al. (1975) made the first significant numerical study on the structure of mantle plumes. They used a finite-difference method, which incorporated the Boussinesq approximation and an infinite-Prandtl-number (Pr) assumption, to solve the steady-state axisymmetric problem. They solved the energy and vorticity transport equations containing two parameters, Rayleigh number (Ra) and viscosity contrast (μ_c) where:

where:

$$Ra = \frac{\alpha g \Delta T h^3}{\nu_r \kappa} \qquad Pr = \frac{\nu_r}{\kappa} \qquad \mu_c = \frac{\mu_r}{\mu}$$

α is the coefficient of thermal expansion

g is the acceleration of gravity

ΔT is the temperature difference

h is the height

κ is the thermal diffusivity

μ_r is the reference dynamic viscosity of the cold fluid

μ is the dynamic viscosity of the hot fluid

ν_r is the reference kinematic viscosity of cold fluid.

Although they assumed flow was restricted to the upper mantle (700 km), some of their conclusions are equally valid for deep mantle plumes. They found, for instance, that the medium must be heated at the base for plumes to occur; internal heating would not produce the narrow structure. They also showed that variable viscosity was necessary for narrow plumes. Finally, they investigated the effect of varying the Rayleigh number from 10^4 to 10^6. They showed that as the Rayleigh number increased, the plume neck width decreased.

Daly and Raefsky (1985) performed a numerical study of the situation described asymptotically by Morris (1982) and experimentally by Ribe (1983), i.e., the motion of a rigid sphere in a highly temperature-dependent medium. They used a finite-element method on the momentum and energy equations, incorporating some of the same assumptions as Parmentier, et al. (1975), specifically the Boussinesq approximation and infinite-Prandtl-number assumption, but they included time

dependency in the energy equation. They also, incidentally, used a primitive-variable approach with a penalty-function formulation in place of the vorticity approach. Their results showed excellent agreement with the results of Morris (1982), Ribe (1983), and Ansari and Morris (1983). Additionally, they were able to investigate a wider parameter range: viscosity variation up to 10^5 and Peclet number (Pe) from 10^{-1} to 10^3, where

$$Pe = \frac{Ua}{\kappa}$$

where:

U is the speed of the sphere

a is the sphere radius.

Daly and Raefsky (1985) assumed the fluid was mechanically driven for their work. They concluded that although the drag reduces with viscosity variation (as compared to Stokes flow with constant viscosity), the heat transport is also more efficient, so a blob of magma will not rise farther than a diameter or two through the mantle or lithosphere without cooling to ambient levels.

Many studies concentrate on overall mantle convection but don't investigate plume structure in detail. Several studies, while concentrating on overall mantle convection, mention the role of plumes in their results. Schubert and Anderson (1985) investigated two-dimensional convection with heating from below as well as internal heating at high Rayleigh numbers using the finite-element method. They compare their results favorably with earlier finite-difference studies of Jarvis and Peltier (1982). While they made progress in using a high Rayleigh number that would be typical of whole-mantle convection, their model assumed constant viscosity in the mantle. Jarvis (1984) was able to study flow at even higher Rayleigh numbers

using a finite-difference method and a stream-function approach to the two-dimensional problem, but he also assumed constant viscosity. He also concentrated on behavior of developed plumes, not plume initiation.

Four papers are most closely related to the numerical approach used in this research. They each make the Boussinesq approximation and infinite Prandtl number assumption in a two-dimensional planar domain. As demonstrated by the common occurrence of these assumptions in the papers described earlier, these assumptions are well accepted for models of mantle convection. Boss and Sacks (1985) solve a stream-function formulation of the problem with a finite-difference method. They initiated plumes by introducing a perturbation into broad-scale mantle convection as well as a static mantle, in an attempt to determine which core-mantle boundary perturbations produced plumes. They concluded that deep-mantle plumes require 50-100 my to penetrate the mantle. This time scale was confirmed by Christensen's (1984) study. Olson, Schubert and Anderson (1987) use a finite-element code to model plume initiation in the lower mantle, with viscosity contrasts of 10^3 and 10^4. Zhao and Yuen (1987) introduced another phenomenon by studying the effects of adiabatic and viscous heating on plumes. They also are the only authors to use an axisymmetric finite-element formulation in addition to a two-dimensional Cartesian formulation for the time-dependent problem. They found that for a uniform thermal expansivity, α, an increase in the adiabatic and viscous heating contributions impedes plume growth. Only with α decreasing with depth does plume structure return in this model. They also observed that the same plume structure appears in the Cartesian two-dimensional and axisymmetric cases, the only quantitative difference being that the temperature in the center of the plume is slightly higher in the two-dimensional case than in the axisymmetric case.

CHAPTER 2

EXPERIMENTAL INVESTIGATION

2.1 Purpose

The goal of the experimental study was to measure the rise speed and to observe the development of starting thermal plumes. As indicated in the literature review, a key aspect of this study was the combination of the buoyancy effects seen in the continuously-fed compositional plume studies of Whitehead and Luther (1975) and Olson and Singer (1985) with the entrainment effects demonstrated by the pulse-fed 'thermals' of Griffiths (1986a-d). Griffiths and Campbell (1990) first studied this combination of buoyancy and diffusive effects experimentally. The current experimental work differs from theirs in two ways: the plumes are generated via thermal input rather than mass input and the viscosity contrast between the fluids is larger than their case. This work at higher viscosity contrasts may be helpful in drawing conclusions about plume behavior at the very large viscosity contrasts which may occur in the mantle.

2.2 Apparatus

The spherical caps of thermally generated starting plumes have larger diameter than those of compositionally generated plumes (Olson and Singer, 1985). This difference is due to the larger value of thermal diffusivity as compared to compositional diffusivity and the resulting entrainment described by Griffiths

9

(1986a-d). Thus, compositional plumes may be studied in a smaller container with minimal wall effects. For the present study, wall effects are minimized for thermal plumes by using a large tank (figure 1).

The tank (designed to be the maximum size that will move through a standard doorway) has dimensions 78.8 X 78.8 X 69.4 cm high. The plume was generated by a 62.2 mm diameter thermo-foil heater which has 265 ohm resistance. The heater was mounted on a metal block; a 7 mm thick layer of plexiglass separated the heater from the block. Vertical length scales on the front and rear of the tank provided a means of measuring the plume height from the photographic record of the experiment.

Table 2. Physical properties of syrup.

thermal diffusivity	2.2×10^{-3} cm^2/sec
specific heat	.7 cal/gm/deg
thermal expansion @22C	3.5×10^{-4} deg^{-1}
thermal expansion @40C	4.5×10^{-4} deg^{-1}
density @-26.1C	1.45 g/cm^3
density @.1C	1.43 g/cm^3
density @25C	1.42 g/cm^3
density @100C	1.39 g/cm^3
dynamic viscosity @-26.1C	2.59×10^{10} mPa-sec
dynamic viscosity @.1C	7.4×10^6 mPa-sec
dynamic viscosity @25C	91104 mPa-sec
dynamic viscosity @100C	223.9 mPa-sec

The fluid used in the tank was ADM 36/43 industrial corn sweetener. A summary of some of its important physical properties is given in table 2. This syrup has a highly temperature-dependent viscosity (figure 2), a key characteristic of

78 cm

69 cm

78 cm

Corn Syrup

height

Heater Foil

6.2 cm
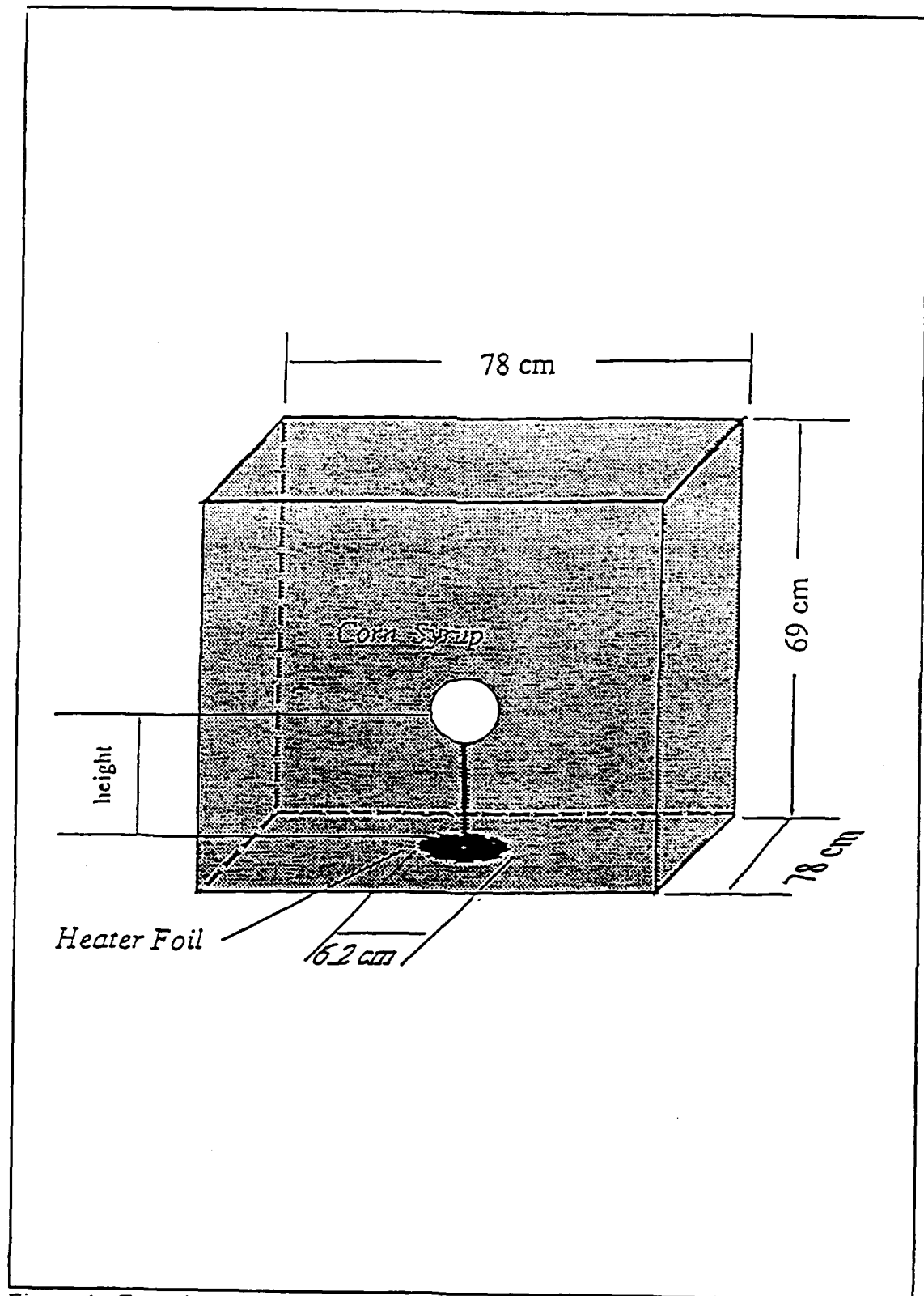
Figure 1. Experimental apparatus.

mantle material. The table also indicates a significant change in the thermal expansion coefficient with temperature. For simplification in analytical and numerical modelling, however, we assumed a constant value for each case. Another useful property of this syrup is that when heated in the experiment, many small vapor bubbles form, apparently the residual of larger bubbles that formed on the surface of the heater and quickly collapsed as they migrated away from the heater. These remnants serve as excellent tracers for flow visualization, yet they do not appear to affect the flow properties. This observation has also been noted by Ansari and Morris (1985). If these bubbles occupied a large percentage volume of the plume, then they would significantly reduce the density in the plume. The experimental photographs indicate, however, that these bubbles probably do not occupy a significant volume percentage. This assumption is based on the observation that one can see through the syrup/bubble mixture fairly easily. A large percentage of bubbles would obscure the view. As a result, we do not account for bubble density in the plume density calculations.

2.3 Procedure

The continuous-feed experiments involved setting the heater to full power in the tank of quiescent, isothermal syrup. The record of the ball shape, volume and height as a function of time was kept photographically (figures 4c, 5c, and 6b). The experiments were run repeatedly for various viscosity contrasts, which were induced by changing the ambient temperature of the tank. Three convenient environments existed to run the experiment with different viscosity contrasts. One, of course, was room temperature. This environment had an ambient temperature of 24.8C and this temperature generated a viscosity contrast (μ_{cold}/μ_{hot}) of 406.9. The other two environments come as a result of access to the National Science Foundation's
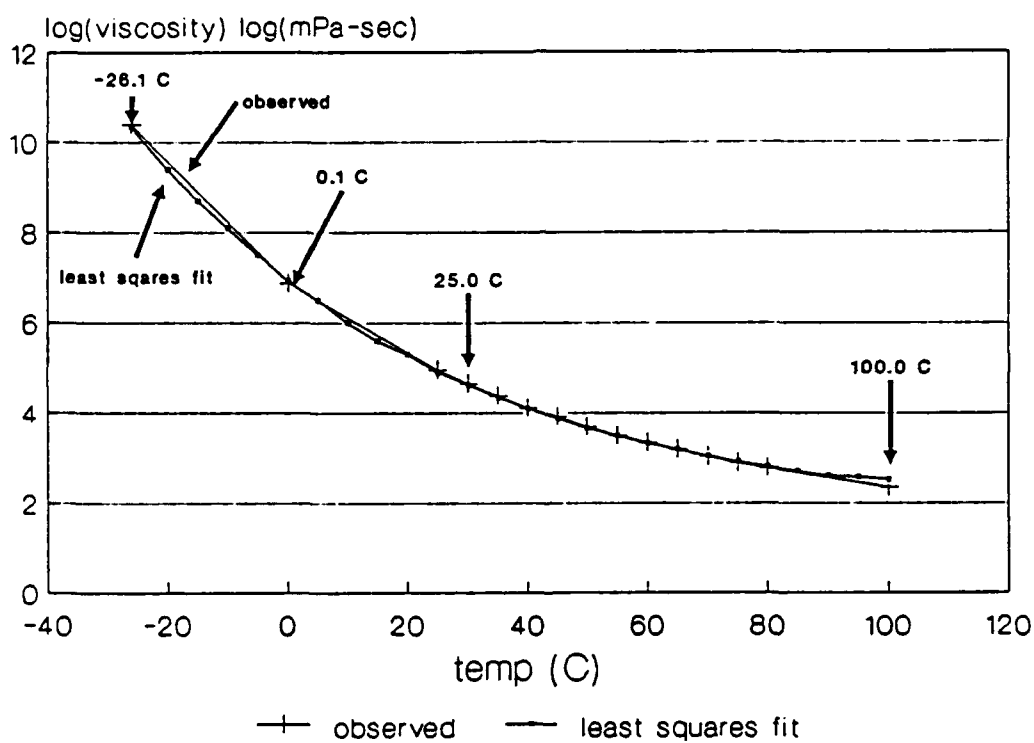
Figure 2. Viscosity variation with temperature for syrup. Least squares fit equation is $\log_{10}(\mu) = 20.6 - 14.99(1000/T) + 3.0762(1000/T)^2$

Antarctic Marine Research Facility on the campus of Florida State University. This facility has large cold storage areas that will accommodate the tank. One storage area is maintained at .1C, generating a viscosity contrast of 3.3 X 10^4. A smaller storage area, maintained at -26.1C, generates a viscosity contrast of 1.1 X 10^8. For comparison, note that the Griffiths and Campbell (1990) experiments used a maximum viscosity contrast of 333.

In addition to the continuous-feed cases that were run at different viscosities, a control pulse-feed case was run at ambient temperature of .1C. In this case, the heater was turned off as soon as the sphere formed above the heater, just before the time when the ball would rise away from the heater, trailing a narrow neck in the continuous-feed case. (We define this time as the liftoff time.) This case was very similar to the experimental study of 'thermals' made by Griffiths (1986a-d) in which he injected a fixed volume of warmer fluid into the ambient fluid. Comparison of the results to those of Griffiths (1986a-d) provided a good test of the experimental apparatus and procedure.

2.4 Results

The results of the control pulse-feed case are presented in figure 3a. A photograph of the typical structure of the thermal is shown in figure 3b. The general agreement of these results with those of Griffiths (1986a-d) indicates that the experimental apparatus and procedure were adequate. Furthermore, this agreement suggests that plume formation via thermal input (heater) occurs similarly to plume formation via injection of warmer fluid as in Griffiths (1986a-d) and Griffiths and Campbell (1990).

Typical results for the continuous-feed cases for all three environments are given in figures 4, 5, and 6. The most accurate measurements were those of height

versus time. These results are given in figures 4a, 5a, and 6a. The measurements of

volume versus time are much less accurate; these results are given in figures 4b and

5b. Corresponding photographs of the typical structures in each environment are

shown in figures 4c, 5c, and 6b. Along with the experimental results, plots of the

rise laws of Whitehead and Luther (1975), Olson and Singer (1985), and Griffiths and

Campbell (1990) are included in figures 4a, 4b, 5a, 5b, and 6a. Note the error bars on

the graphs. The agreement of these rise laws with the experimental data depends

largely upon where the plot begins. In order to have a fair comparison, the plot of

each rise law starts at the liftoff time and passes through the first two observational

points. These plots provide a graphical means of comparing the effectiveness of the

rise laws. Additionally, table 3 provides a quantitative means of comparing these

models (using height vs. time data). By computing the experimental standard

deviation of the least-squares fit for each rise law, a numerical value may be

assigned which indicates how well each rise law models the experimental result.

Note that these results represent curves that are different from those in figures 4a,

5a, and 6a. The continuous-feed case with viscosity contrast of 1.1×10^8 shown in

figure 6a and 6b displayed a different morphology than previous cases; the ball

never lifted away from the heater.

The graphical comparison of these plots with the experimental data and the

results presented in table 3 lead to a few observations. First, the rise law of

Whitehead and Luther (1975) is the poorest model of the experimental data. This

poor performance is expected, however, since Whitehead and Luther did not

incorporate any diffusive effects in their model, nor should they since they were

dealing with immiscible fluids. Griffiths' (1986a-d) work clearly shows that

diffusion and subsequent entrainment of ambient fluid accelerate the growth of the

sphere and slow the sphere rise when compared to the no diffusion case, so
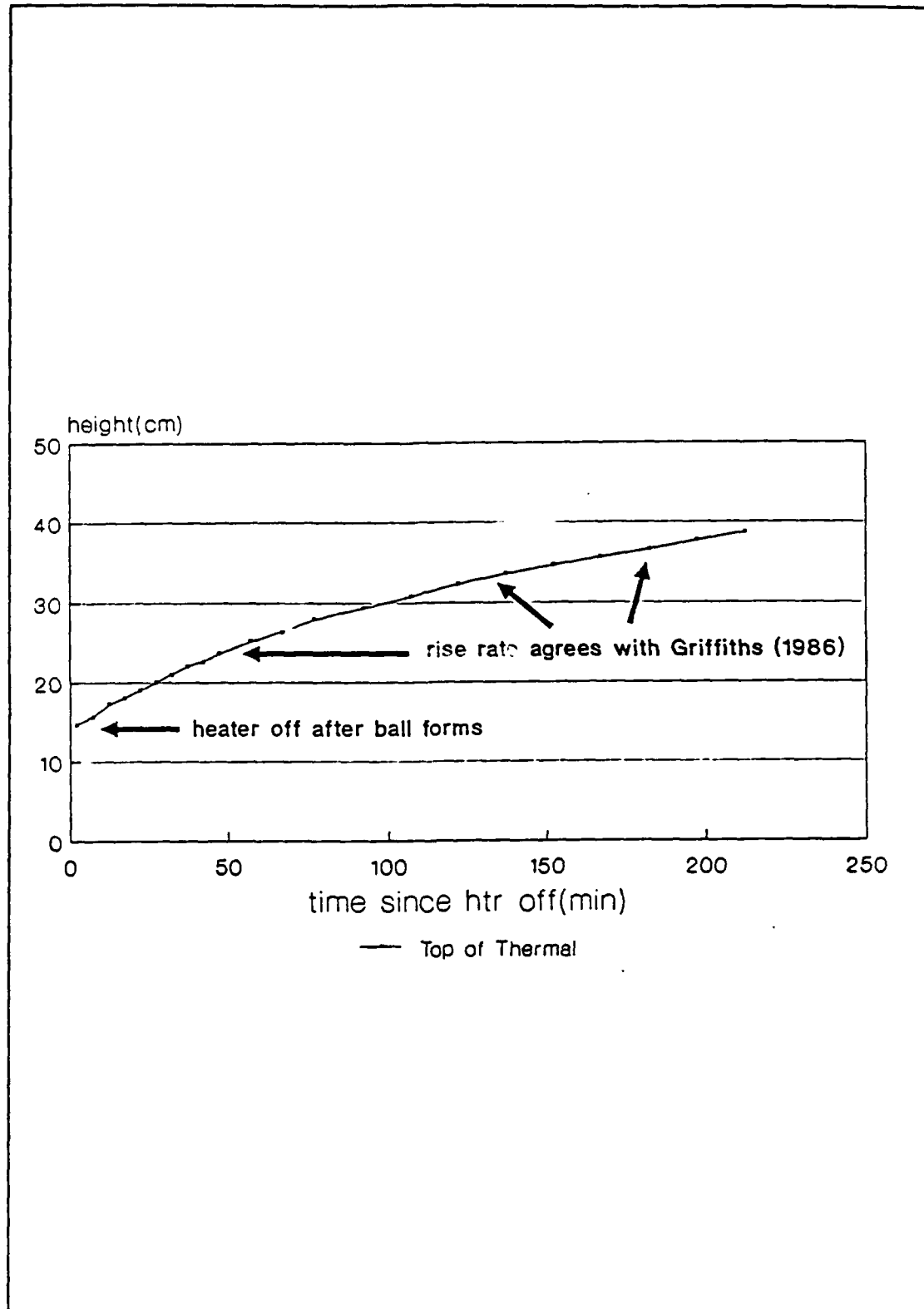
Figure3a. Results of pulse feed experiment.
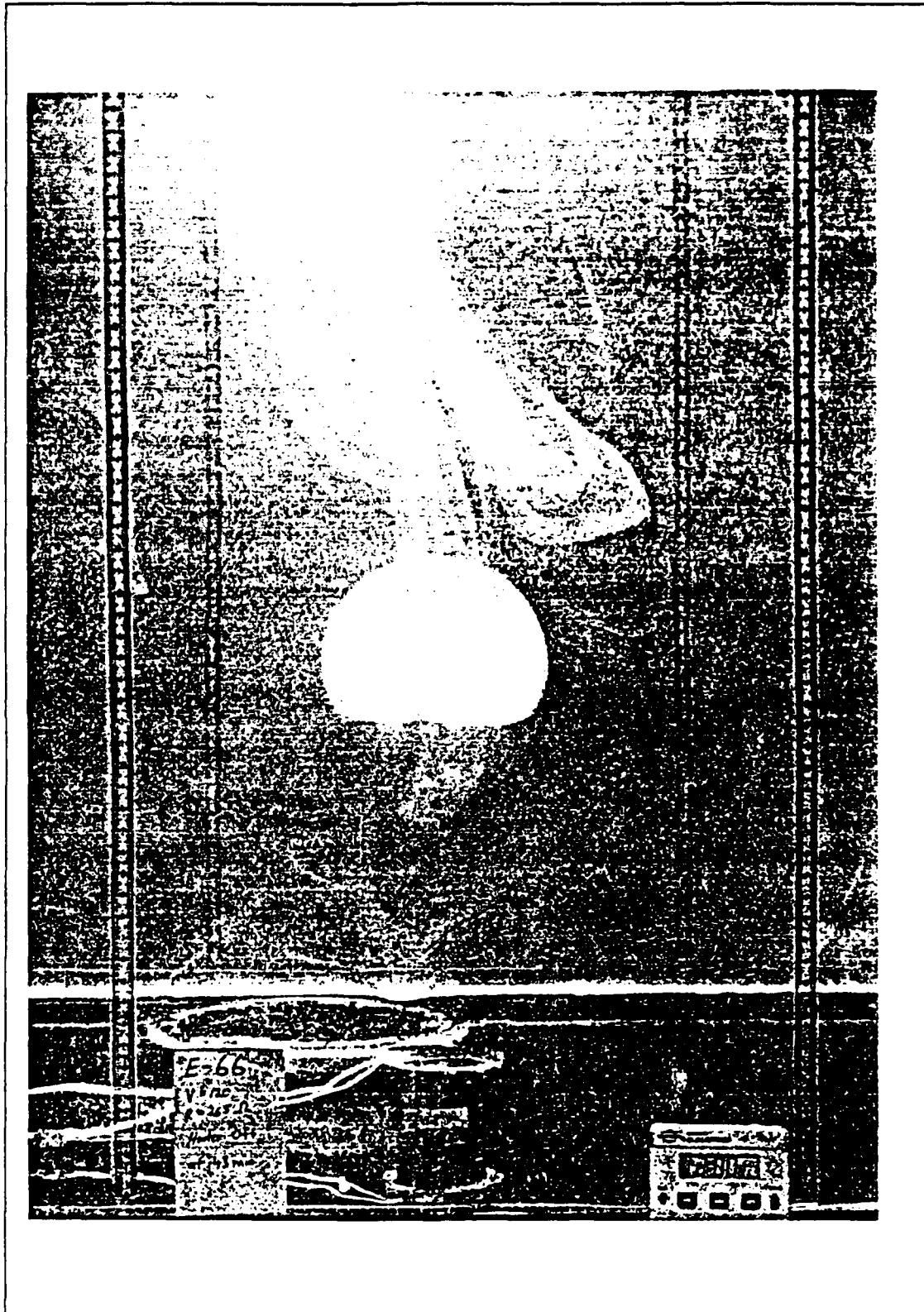
Figure 3b. Typical structure of pulse feed diapir.
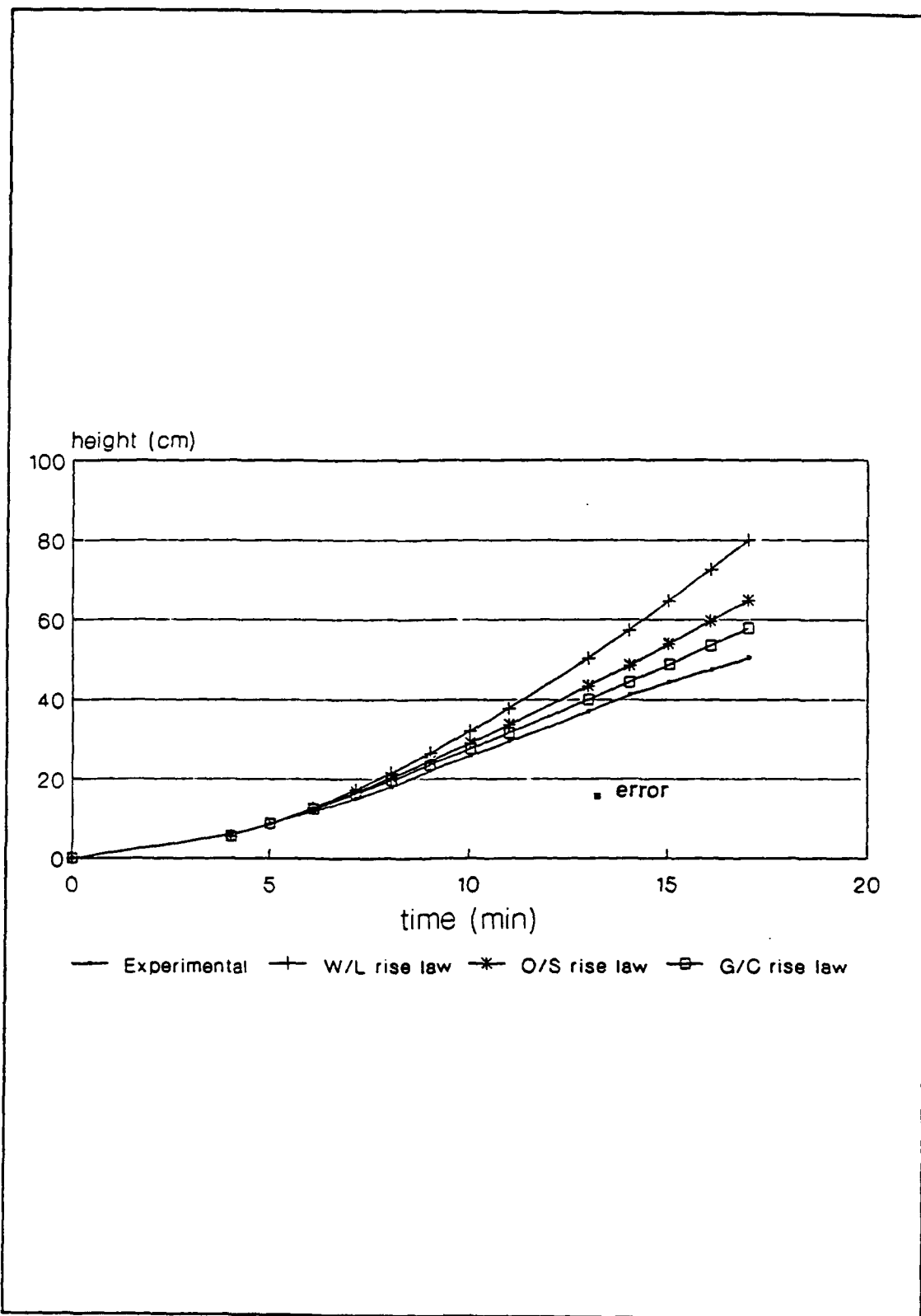
Figure 4a. Height vs. time, $T_{amb}=25C$.
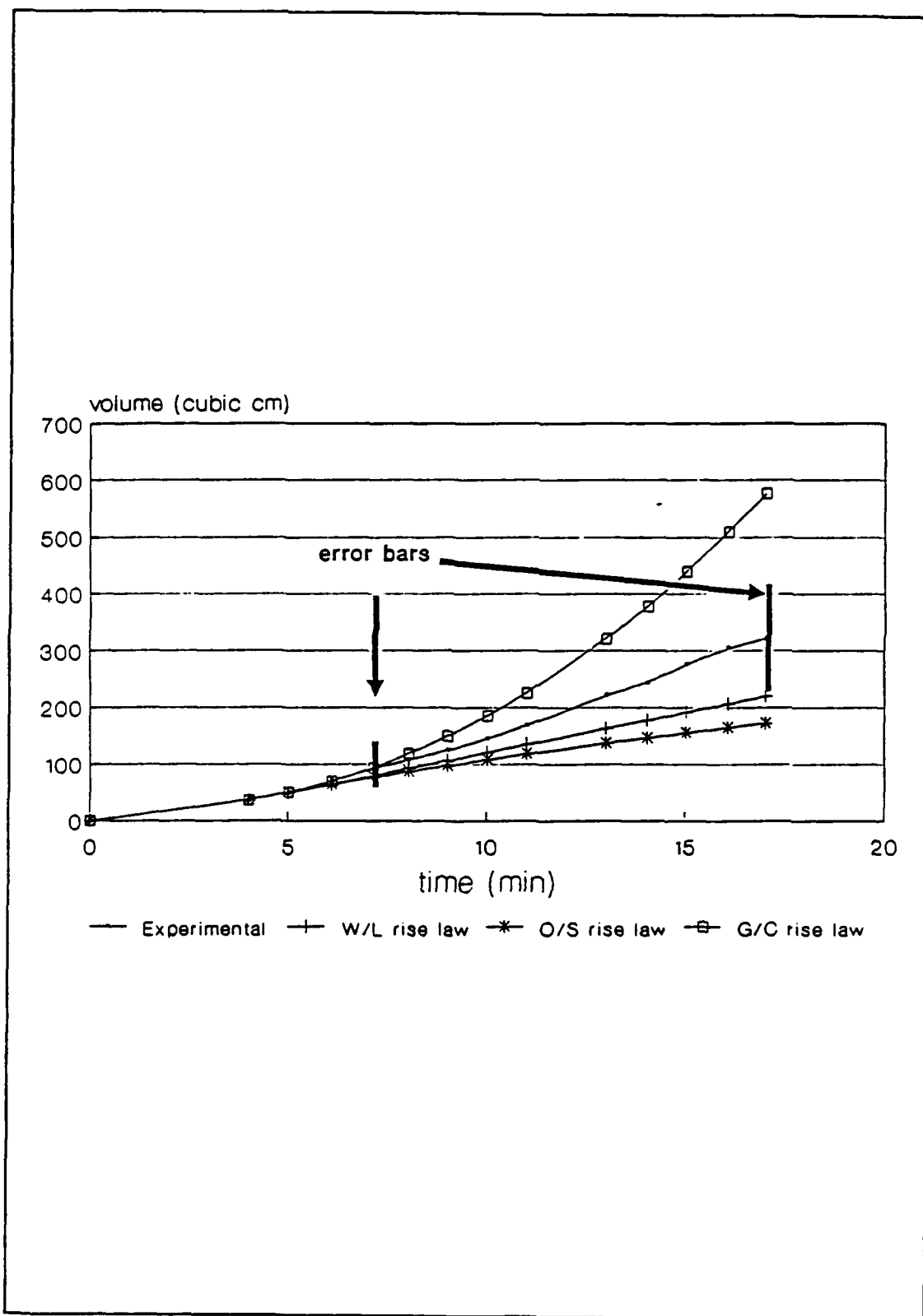
Figure 4b. Volume vs. time, $T_{amb} = 25C$.
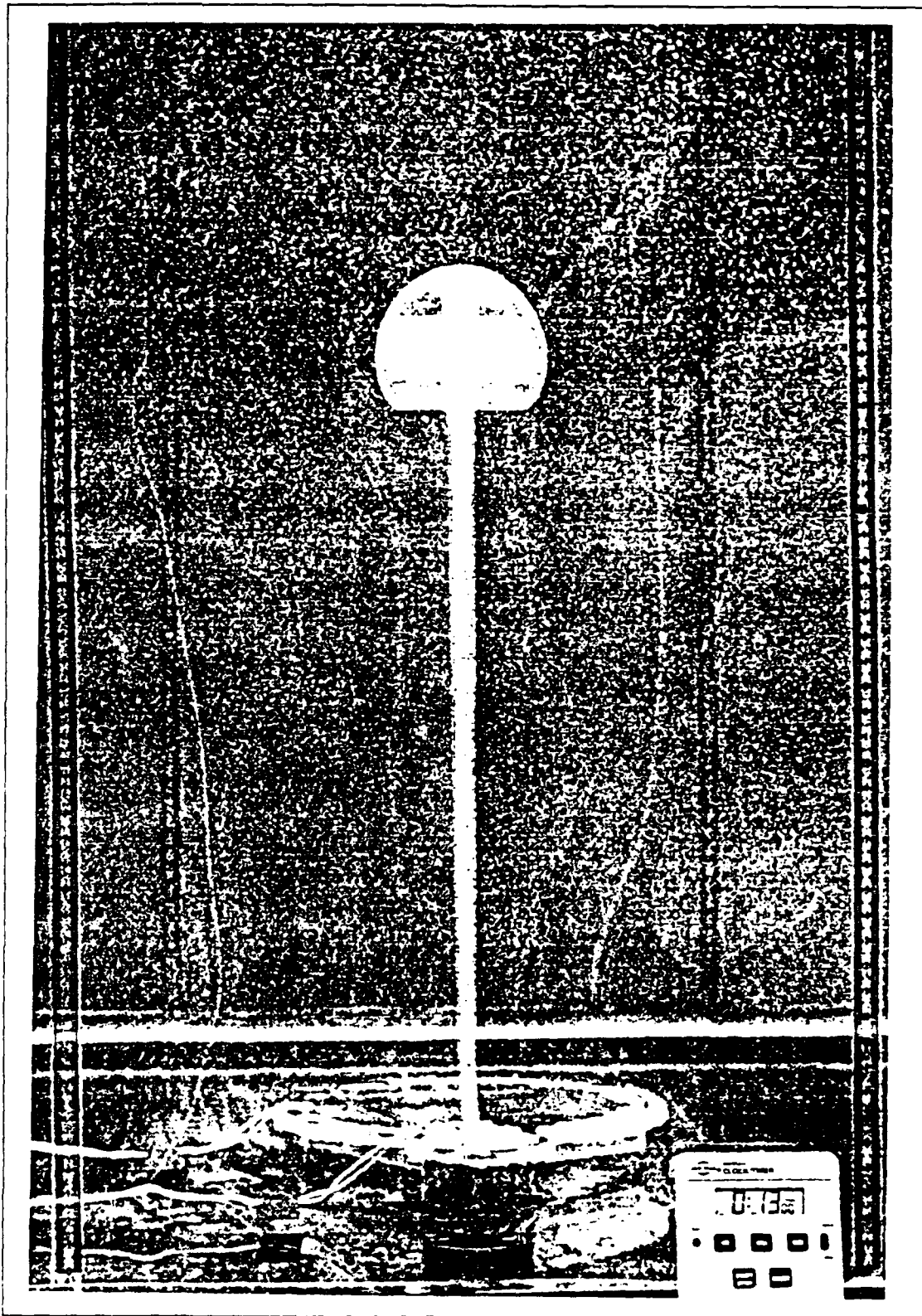
Figure 4c. Typical structure for $T_{amb}=25C$ case.
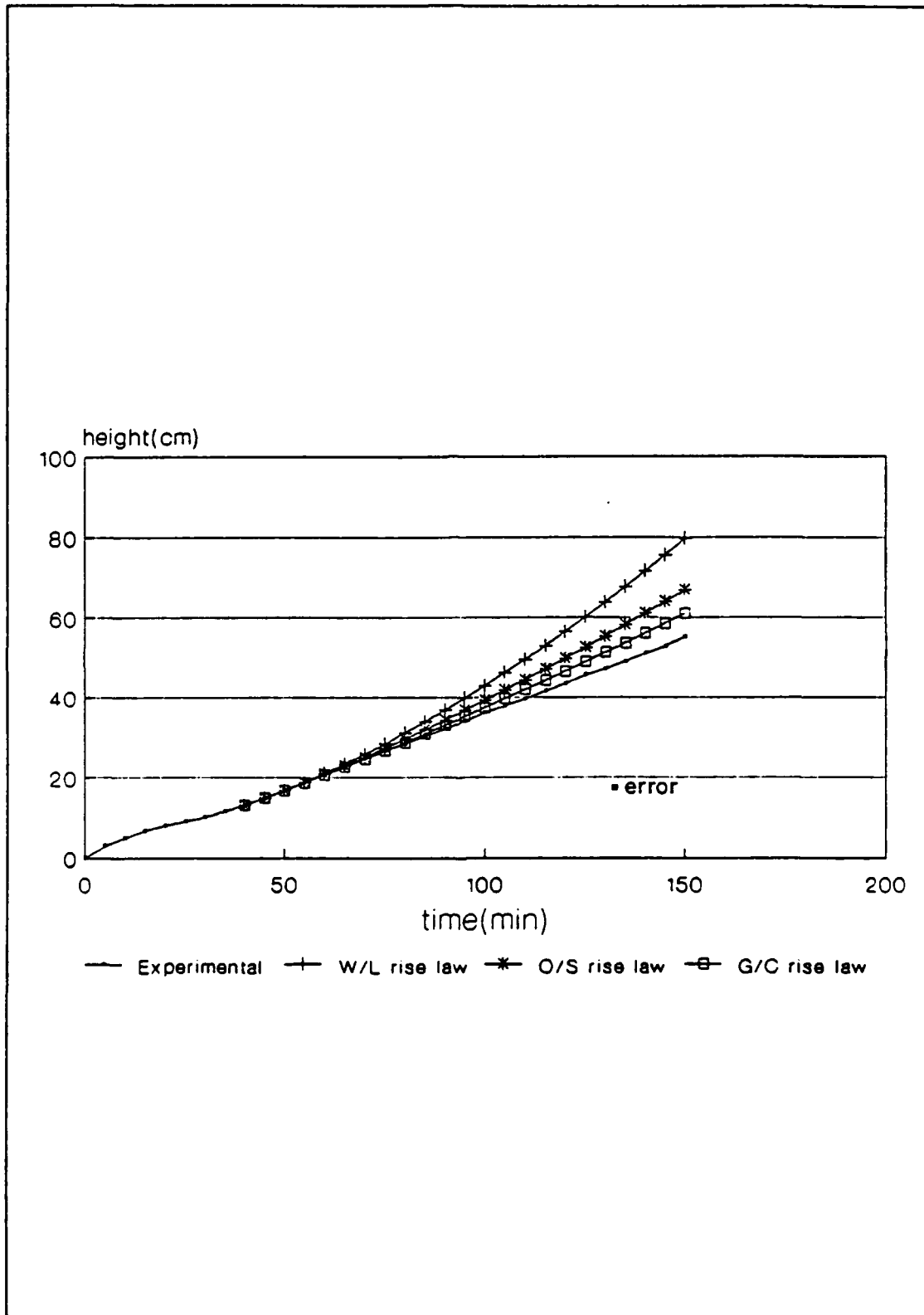
Figure 5a. Height vs. time, $T_{amb} = 0.1C.$
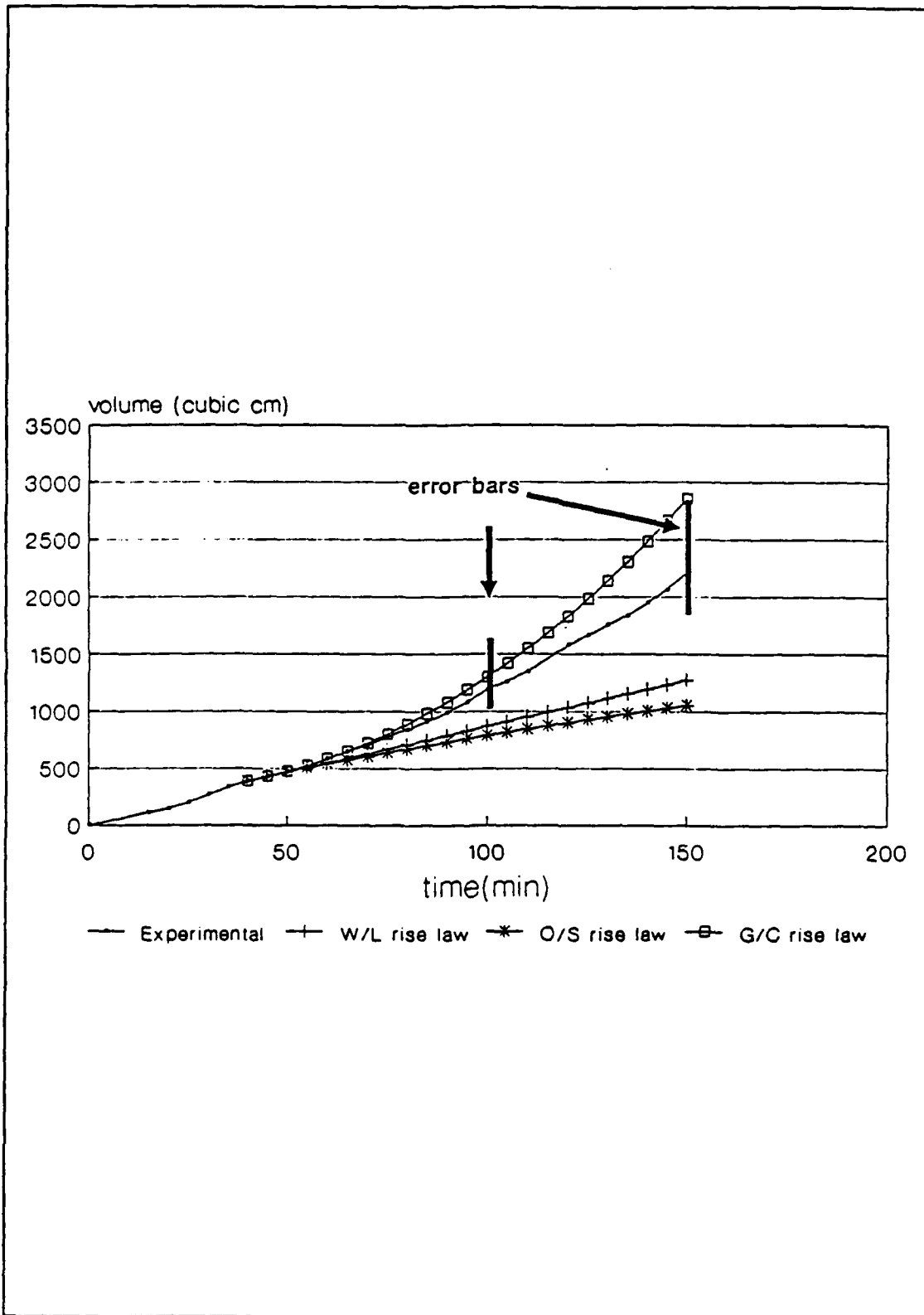
Figure 5b. Volume vs. time, $T_{amb} = 0.1C$.
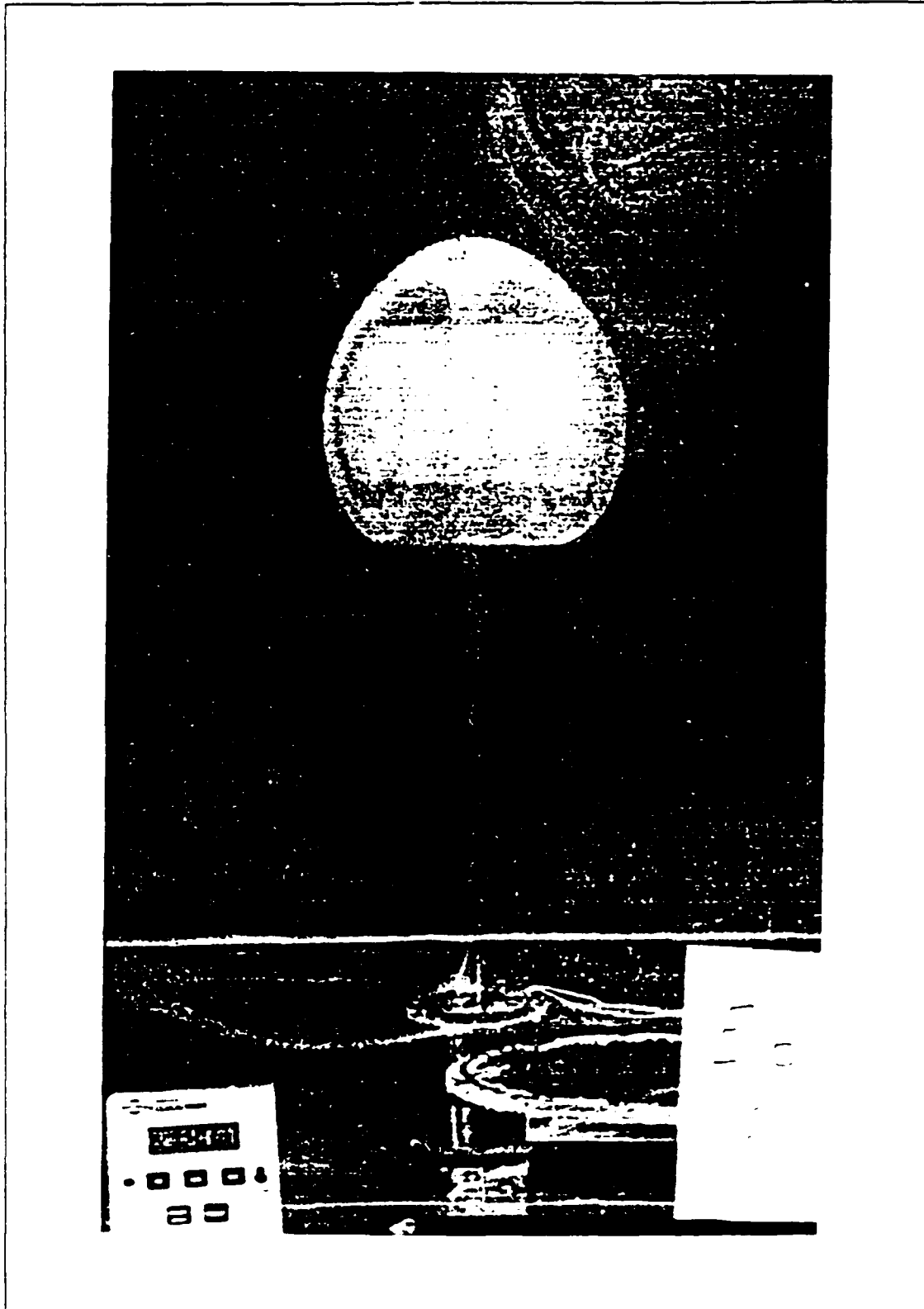
Figure 5c. Typical structure of $T_{amb} = 0.1C$ case.
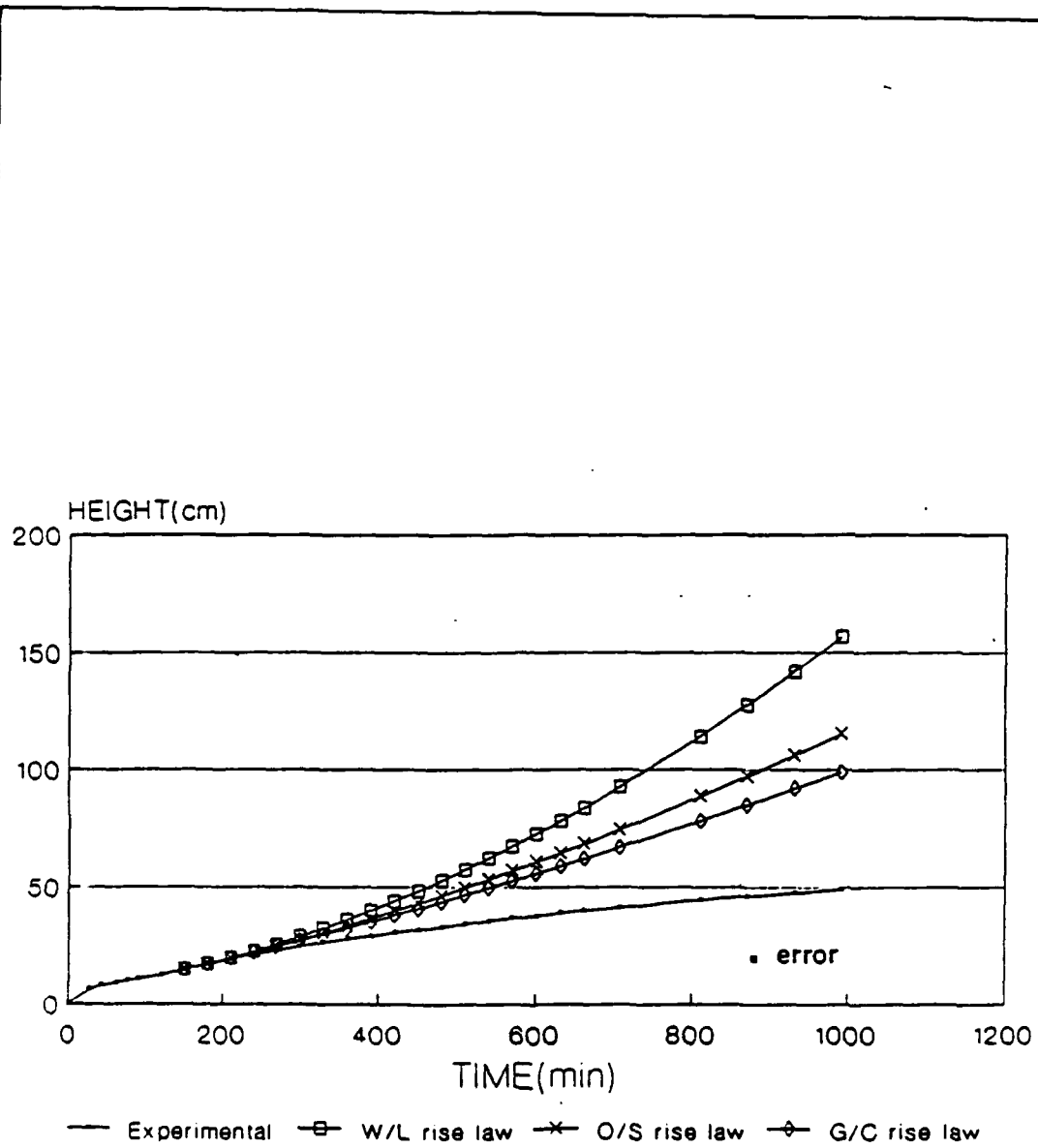
Figure 6a. Height vs. time, T_{amb}=-26.1C.
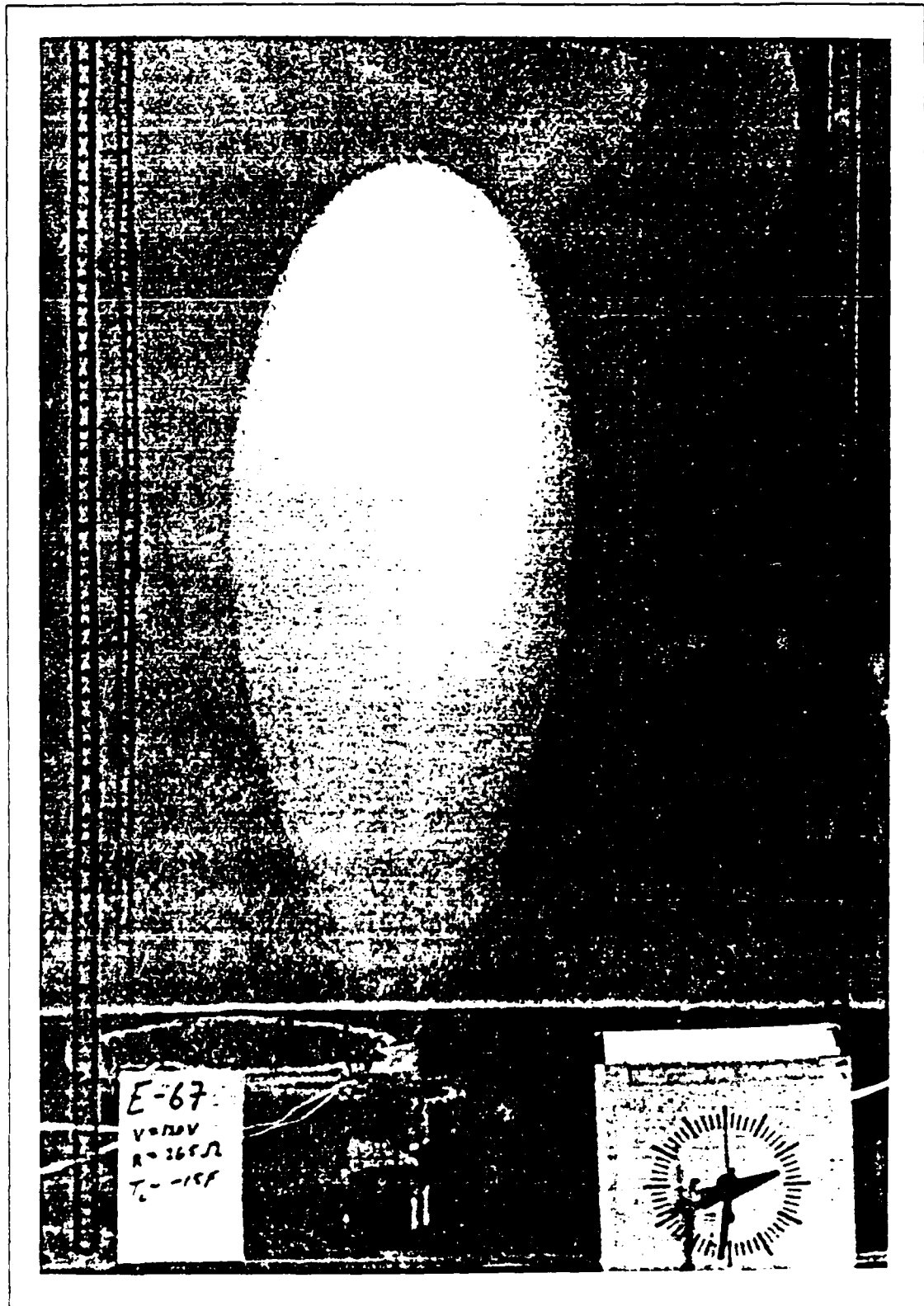
Figure 6r. Typical structure for $T_{amb} = -26.1C$ case.

r the thermal plume will result in larger rise speeds. The

75) law, consequently, shows an increasing speed since the

oy the slowing effects of diffusion. The volume of the ball

maller for this case since their model only accounts for the

nduit, i. e., no ambient material is entrained. The rise law

) performs better than that of Whitehead and Luther

dequate. Their rise law is based on experimental

onal analysis, and does not consider the dynamics of the

plumes were generated using a compositional difference of

did not include compositional diffusion as a factor in their

eir experimental results, however, showed some slowing and

to the Whitehead and Luthei (1975) rise law. These

small amount of compositional diffusion between the two

al diffusion is a slow process relative to thermal diffusion,

ly, the best model to date is that of Griffiths and Campbell

s the effect of thermal diffusion. A key assumption of

hat all of the heat diffusing from the ball is re-entrained in

ves the ball. Their model predicts a higher speed and a

time than the experimental results indicate, as shown in

ble 3 lists the minimum standard deviation for an

exponential rise law is one where height ~ time $^{\xi}$. Each of

ws is an exponential rise law ($\xi = 5/3$ for

5 for Olson/Singer, and $\xi = 5/4$ for Griffiths/Campbell).

the exponential rise law that predicts the experimental

as $\xi = 1.047$. For the $T_{amb} = 0.1C$ case, $\xi = 1.125$, and for

Table 3. Quantitative model comparison.

MODEL	STANDARD DEVIATION		
	$T_{amb}=25C$	$T_{amb}=0.1C$	$T_{amb=-26.1}$
Whitehead/Luther	1.44602	1.02836	3.47298
Olson/Singer	.94595	.60531	2.87026
Griffiths/Campbell	.69916	.40745	2.5039
optimal exponential	.5304	.3348	.17538

the T_{amb} = -26.1C case, ξ = .3743. The Olson and Singer (1985) experimental rise law gives a 54% improvement (for the T_{amb} = 25c case) and 61% improvement (for the T_{amb} = 0.1C case) over the Whitehead and Luther (1975) rise law when compared to this optimal exponential case. The Griffiths and Campbell (1990) addition of diffusion to the model shows a larger improvement in the model's performance when compared to these optimal exponential rise laws. Their model accounted for 81.6% (in the T_{amb} = 25C case) and 89.5% (in the T_{amb} = 0.1C case) of the difference between the Whitehead and Luther (1975) model and the best exponential rise law. Note that for the T_{amb} = -26.1C case, the Olson and Singer (1985) rise law shows an 18.2% improvement over the Whitehead and Luther (1975) prediction. The Griffiths and Campbell (1990) model gives an improvement of 29%, but the relatively large standard deviations in all the models indicate that none of the previously developed rise laws is adequate for this case.

These results show the importance of including diffusive effects in an analytical model of plume rise. They also indicate the possibility of improving the model by relaxing some of the assumptions used by Griffiths and Campbell (1990). Figure 6b suggests that their assumption of total heat entrainment may be too strong. In this T_{amb} = -26.1C case, clearly much of the heat input to the plume is lost from

the 'ball'. This result suggests that, to a lesser degree, some heat may be lost from the ball in the other two cases. A logical step for improving their model is to relax this assumption.

CHAPTER 3

ANALYTICAL MODELLING

3.1 Key Physical Interactions

One of the major reasons for performing an experimental investigation of this problem was to develop some sense of the important physical interactions that occur in plume initiation and development. The experimental results clearly indicate that one important interaction is thermal diffusion and entrainment. The hot fluid rising from the heater heats the ambient fluid and entrains some of it into the sphere. Griffiths (1986a-d) showed that this entrainment alone causes the sphere to grow in size and slow in speed as time progresses. In the experimental results of chapter 2 (figures 4a and 5a), the performance of the model that included diffusion (Griffiths and Campbell, 1990) was superior to the models that neglected diffusion (Whitehead and Luther, 1975; Olson and Singer, 1985). Another important interaction that the experiment illustrated was heat loss. In the $T_{amb} = -26.1C$ case (figure 6b), a large fraction of heat was lost from the 'ball'. This factor may also play a significant role in the cases with smaller viscosity contrast.

The complications introduced by these interactions make analytical investigation difficult. For example, boundary layer analysis is complicated by the fact that the thermal layer is wound into the interior of the ball. While these interactions make many types of analysis difficult or impossible, they also force a very fundamental approach to the study. The goal of this analysis is to produce a first order or 'engineering' approximation to the fluid behavior. This approximation

29

will be tested against the experimental results presented in chapter two.

3.2 System Description

Figure 7 presents a sketch used to define the system under study. The system

consists of that portion of the (radius c) ball of the plume marked by the stippled

region. The center of the ball serves as the origin of the frame of reference for the

system, with the far-field velocity, U, approaching the ball from above. A dividing

streamline, marked with the letter D, separates the ambient fluid that is entrained

from that which is left behind. The system is defined so that all entrained fluid

enters the system through the annular region marked by B. The warm fluid from the

heater enters the system through the annular region marked by A. The symbol ζ

represents the entrained-layer thickness, δ represents the thermal-boundary-layer

thickness, F is the (constant) source volume flux into the system, r_c is the radius of

the feeder conduit, and T_s is the temperature of the source material. T_{amb}, ρ_∞ and

μ_∞ represent the (constant) quantities of ambient temperature, density, and viscosity.

3.3 Assumptions

With the system so defined, make the following simplifying assumptions for

the analytical model:

(1) Heat loss in the conduit is negligible compared to heat loss in the

ball.

(2) The temperature, density, and viscosity inside the ball may be

approximated by average values. Let T, ρ, and μ represent the average

temperature, density, and viscosity, respectively, of the fluid inside

the system.

(3) The temperature in the thermal layer of thickness δ varies only in
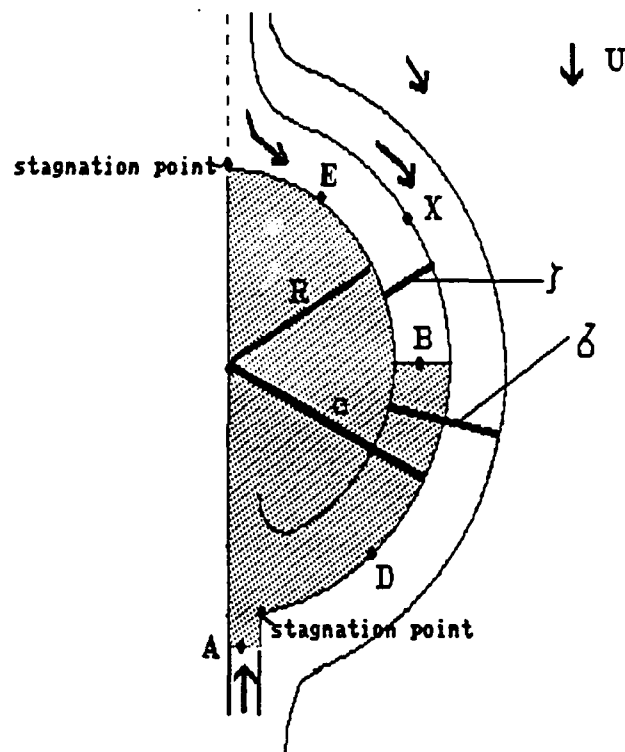
Figure 7. System used in analytical solution

the radial direction. Furthermore, the temperature profile across this layer is linear.

(4) Negligible differences exist between the values of density and specific heat in the heated and ambient fluids for mass conservation considerations.

(5) For asymptotic calculations, the entrained layer is thin, i. e., c ~ R or $\zeta \ll 1$.

(6) $\mu_\infty \gg \mu$, so Stokes law (Batchelor, 1967) may be written as,

$$U = \frac{g\alpha R^2 \Delta T}{3v_\infty} \qquad (1)$$

where:

  α is the coefficient of thermal expansion

  g is the acceleration of gravity.

  v_∞ is the ambient kinematic viscosity

  ΔT is $T - T_{amb}$.

(7) The portion of mass input from the heater that goes into the lengthening conduit is negligible ($A_c U \ll F$).

(8) The average speed of fluid in the conduit (U_c) is greater than U.

3.4 Thermal Power Balance

Applying the principle of conservation of energy to the stippled volume in figure 7 yields the following general relationship for thermal energy stored in the system

where:

$$\frac{dQ}{dt} = \dot{Q}_{in} - \dot{Q}_{out} \tag{2}$$

"." symbolizes rate of change per unit time

$\dot{Q}_{in}$ is the rate of heat transferred into the system

$\dot{Q}_{out}$ is the rate of heat transferred out of the system

Q is the thermal energy stored in the system.

Now, the heat input to the system comes as a result of the warm fluid entering through the circular region marked by A (from the source) and through the annular surface region marked by B (from entrainment). Symbolically,

$$\dot{Q}_{in} = \dot{Q}_A + \dot{Q}_B \tag{3}$$

Heat leaves the system via conduction through the surfaces of the hemispheres marked by E and D. So,

$$\dot{Q}_{out} = \dot{Q}_E + \dot{Q}_D. \tag{4}$$

Note hemisphere E has radius R while hemisphere D has radius c (=R + ζ). The heat transferred through E is greater than that transferred through the surface of the hemisphere marked by X, with the difference being the amount entrained through the annular surface marked by B, i. e.,

$$\dot{Q}_B = \dot{Q}_E - \dot{Q}_X \tag{5}$$

Now, substituting (3), (4), (5), into (2) gives

$$\frac{dQ}{dt} = \dot{Q}_A - \dot{Q}_X - \dot{Q}_D. \tag{6}$$

Assumption (1) allows us to write

$$\dot{Q}_A = F\Delta T_s \rho c_p \qquad (7)$$

where: c_p is the specific heat at constant pressure.

$\Delta T_s = T_s - T_{amb}$ (constant)

To find an expression for the heat lost from the system at the surface of the sphere marked by X and D (radius = c), use assumptions (2) and (3). Then,

$$\dot{Q}_X + \dot{Q}_D = 4\pi kc^2\frac{dT}{dr}\Big|_{r=c} \sim 4\pi k\gamma(\frac{c^2\Delta T}{\delta}) \qquad (8)$$

where:

k is the thermal conductivity

γ is a dimensionless parameter, defined so that γ^2 is the ratio of heat loss from the sphere of radius c to total heat loss from the sphere of radius R. Note that $0 \le \gamma \le 1$.

Making these substitutions for $\dot{Q}_A$, $\dot{Q}_X$, and $\dot{Q}_D$, equation (6) becomes

$$\frac{d(Q)}{dt} = \rho c_p F\Delta T_s - 4\pi K\gamma(\frac{c^2\Delta T}{\delta}) \qquad (9)$$

The thermal energy, Q, stored in the system is

$$Q = \rho c_p V\Delta T \qquad (10)$$

where V is the volume of the system.

Substituting this expression into (9), using assumption (4), and recalling that k =

$\rho c_p \kappa$ gives

$$\frac{\partial(V\Delta T)}{\partial t} = F\Delta T_s - 4\pi\kappa\gamma\left(\frac{c^2\Delta T}{\delta}\right). \tag{11}$$

where κ is thermal diffusivity.

Note that if the heat loss term, $\dot{Q}_X + \dot{Q}_D$, is zero, this equation reduces to the

energy balance used in the Griffiths and Campbell (1990) model.

3.5 Mass Balance

Using assumptions (4) and (7), the application of the principle of conservation

of mass to the system yields

$$\frac{dV}{dt} = F + e \tag{12}$$

where: e is the rate of entrained fluid entering the system, and A_c is the area

of the conduit.

Since the speed of the fluid at the equator of the ball is U/2 (Happel and

Brenner, 1965), ambient fluid is entrained at B at the rate $e = \pi RU\zeta$. So, equation

(12) becomes

$$\frac{dV}{dt} = F + \pi RU\zeta. \tag{13}$$

3.6 Simplification

We can estimate the thickness of the thermal boundary layer, δ, by $(\kappa t)^{1/2}$.

The time that the hot and cold fluids are in contact is proportional to R/U. So,

$$\delta = k_1\left(\frac{\kappa R}{U}\right)^{1/2} \tag{14}$$

where k_1 is a dimensionless constant.

In the best model available, Griffiths and Campbell (1990) assumed that all of the heat added to the system was entrained in the ball of the plume. In the present notation, this is equivalent to setting ζ equal to δ, i. e., all of the thermal boundary layer is entrained. The experimental study in chapter 2 suggested that not all of the heat added to the system was entrained in the system. This heatloss is most vivid in the $T_{amb} = -26.1$C case (figure 6b). Heat loss will also, however, play a role in the other two cases considered. In all of these cases, only a portion of the thermal boundary layer will be swept into the ball, i. e., $\zeta < \delta$. Define a ratio between ζ and δ using a dimensionless parameter η where

$$\zeta = \eta\delta \tag{15}$$

Note $0 \le \eta \le 1$ so $\eta = 0$ means no entrainment and $\eta = 1$ means no heat loss.

This new parameter, η, is related to the location of the rear stagnation point in figure 7. The streamline around the ball that ends at this stagnation point is the dividing line between entrained fluid and that left behind. The position of this stagnation point will vary depending on the size of U relative to the speed of the fluid coming up the conduit (U_c). A reasonable relationship that incorporates this

speed dependence is

$$\eta = 1 - (U/U_c)^\beta \tag{16}$$

where:

β is a nonnegative dimensionless constant

U_c (= F/A_c) is the average speed of fluid in the conduit.

For a continually fed plume, $U < U_c$, so $\eta < 1$, as required. The constant β provides a measure of the effect that the U/U_c ratio has on η. As β approaches infinity, η approaches 1 and we again have the case in which all of the thermal layer is entrained (Griffiths and Campbell, 1990). For $\beta = 0$, $\eta = 0$ and none of the heated ambient fluid is entrained into the ball. For our purposes, the appropriate value of β will be determined from experimental data or numerical computation data.

The previously defined dimensionless quantity, γ, in equation (8) can be expressed in terms of η. Since γ^2 is the ratio of heat lost from the system at the surface of the sphere of radius c to the total heat lost through the surface of the sphere of radius R (figure 8), we have

$$\gamma^2 = \frac{H_L}{H_T} = \frac{(\zeta - \delta)^2}{\delta^2} = (1 - \eta)^2 = \left(\frac{U}{U_c}\right)^{2\beta} \tag{17}$$

Using Stokes law (1), the thermal boundary layer approximations (14) and the
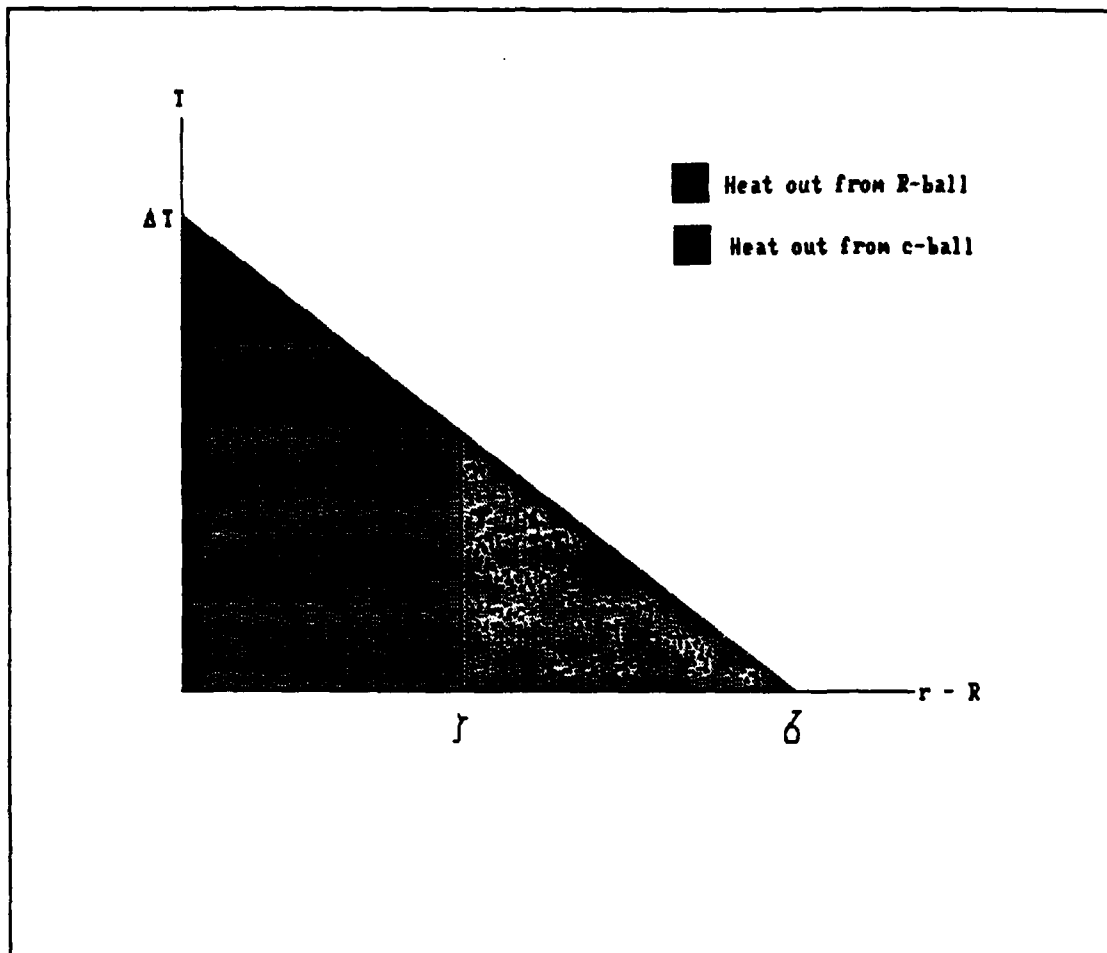
Figure 8. Simplified temperature profile through the thermal boundary layer.

thermal/fluid boundary layer relationships (15-17), and assumption (5) yields:

$$mass: \quad \frac{dV}{dt} = F + \pi k_1 \kappa^{1/2}\left(1-\left(\frac{U}{U_c}\right)^{\beta}\right)U^{1/2}R^{3/2} \tag{18}$$

$$energy: \quad \frac{d(V\Delta T)}{dt} = F\Delta T_s - \frac{12\pi\kappa^{1/2}v}{k_1 g \alpha}\left(\frac{U}{U_c}\right)^{\beta}\frac{U^{3/2}}{R^{1/2}} \tag{19}$$

3.7 Asymptotic Analysis

Nondimensionalize equations (18) and (19) by setting

$$r = \frac{R}{R_\infty}, \quad \tau = \frac{t}{t_\infty}, \quad \theta = \frac{\Delta T}{\Delta T_s}, \quad u = \frac{U}{U_c}, \quad v = \frac{V}{V_\infty} \tag{20}$$

where,

$$R_\infty = \left(\frac{9 v_\infty F}{8 \pi g \alpha \Delta T_s} \right)^{1/4}, \quad V_\infty = 4/3 \pi R_\infty^3, \quad t_\infty = \frac{V_\infty}{F} \tag{21}$$

R_∞ is the asymptotic radius of the ball for the case of no entrainment or no heat loss (Whitehead and Luther, 1975). In that case, the radius of the ball will grow no larger than R_∞. V_∞ is the volume of a sphere of radius R_∞ and t_∞ is the time required to fill this volume at a flow rate of F. Using assumption (7), the resulting dimensionless equations are

$$\frac{dv}{d\tau} = 1 + \left(\frac{P}{S^{3/8}} \right) r^{3/2} u^{1/2} (1 - u^\beta) \tag{22}$$
$$(a) \quad (b) \qquad\qquad (c)$$

$$\frac{d(v\theta)}{d\tau} = 1 - \left(\frac{CP^3}{S^{7/8}} \right) \frac{u^{3/2}}{r^{1/2}} u^\beta \tag{23}$$
$$(e) \qquad (f) \qquad (g)$$

where,

$$P = \pi k_1 \left(\frac{9}{8\pi} \right)^{3/8} \left(\frac{F U_c}{\kappa^2} \right)^{1/2}, \quad S = \frac{g \alpha \Delta T_s F^3}{v_\infty \kappa^4},$$
$$C = \frac{3}{2 \pi k_1^4} \left(\frac{8\pi}{9} \right)^{5/4} = \frac{1.7236}{k_1^4}, \quad v = r^3 \tag{24}$$

Note S has been defined to be analogous to the standard Rayleigh number. The Stokes equation (1) in dimensionless form is

$$u = \left(\frac{DS^{1/2}}{P^2}\right)r^2\theta \tag{25}$$

where,

$$D = \frac{1}{8\sqrt{2}\pi^{5/2}k_1^2}\left(\frac{8\pi}{9}\right)^{3/4} = \frac{0.011}{k_1^2} \tag{26}$$

At small times, before ball liftoff, the entrainment term (c) in equation (22) and the heat loss term (g) of equation (23) can be neglected. With these simplifications, these equations yield a rise law identical to that of Whitehead and Luther (1975):

$$\begin{aligned} \theta &\sim 1 \\ r &\sim \tau^{1/3} \\ u &\sim \tau^{2/3} \end{aligned} \tag{27}$$

These relationships hold for $\tau < \tau_1$, where

$$\tau_1 \sim S^{9/20}P^{-6/5} \tag{28}$$

For $\tau > \tau_1$, the entrainment term (c) becomes important in the mass equation (22). In this case, the rise law is identical to Griffiths and Campbell (1990):

$$\begin{aligned} r &\sim \tau^{3/4} \\ \theta &\sim \tau^{-5/4} \\ u &\sim \tau^{1/4}. \end{aligned} \tag{29}$$

This result will hold as long as the heat loss term (g) is negligible, i.e., for $\tau_1 < \tau < \tau_2$, where

$$\tau_2 \sim \left(\frac{S^{3/\beta} - {}^{1/4}D^{2/\beta} + 1}{C^{4/\beta}P^{12/\beta}} \right). \tag{30}$$

When $\tau > \tau_2$, heat loss (g) balances input (f) in the energy equation (23) and entrainment (c) balances the rate of storage (a) in the mass equation (22), giving a new result

$$\begin{aligned} r &\sim \tau^{\frac{3+2\beta}{4+3\beta}} \\ \theta &\sim \tau^{-\frac{5+4\beta}{4+3\beta}} \\ u &\sim \tau^{\frac{1}{4+3\beta}}. \end{aligned} \tag{31}$$

3.8 Comparison with Experimental Result

The asymptotic model developed in this chapter modifies the Griffiths and Campbell (1990) model by adding the effects of heat lost from the ball. This addition results in a smaller asymptotic rise speed (equation 31) for any finite β, compared to the best previous model (Griffiths and Campbell, 1990). Since the speed of the experimental results was roughly constant, and the Griffiths and Campbell (1990) rise law predicted slightly increasing speeds, any finite choice of β will bring the new model closer to the experimental results.

This improvement may be measured quantitatively by computing the percentage of the difference between the Whitehead and Luther (1975) model and the optimal exponential model. This same comparison was used to evaluate the performance of the Olson and Singer (1985) and the Griffiths and Campbell (1990)

models in chapter 2 where the best percentage improvement (Griffiths and Campbell, 1990) was 81.6% for the $T_{amb} = 25C$ data and 89.5% for the $T_{amb} = 0.1C$ case. The new asymptotic model allows β to be chosen to match the optimal exponential model, so for $\beta = 5.76$ (for $T_{amb} = 25C$) and $\beta = 1.33$ (for $T_{amb} = 0.1C$), the percentage improvement is 100%. The rise laws for these cases are plotted in figures 9 and 10. (The corresponding volume versus time plots are given in figures 11 and 12.) These choices of β indicate a measurable improvement, however, they also suggest that the addition of heat loss to the model is not as significant a contribution as the addition of entrainment. The addition of entrainment alone (Griffiths and Campbell, 1990) accounts for the majority of the difference from the experimental results. For the $T_{amb} = -26.1C$ case, β must be chosen as -1.866 in order to match the optimal exponential model. This choice of a negative β violates our assumption that $\beta > 0$ and makes the new model invalid for this case.

The determination of β may be based on comparison with experimental or numerical data, or on some knowledge of the relationship between the thermal and fluid boundary layers for a given set of parameters. Any positive, finite choice of β will improve the model. For example, $\beta = 1$ results in a 95% improvement for the T_{amb} case and a 99% improvement in the $T_{amb} = 0.1C$ case. This general improvement in these two cases for all positive, finite β confirms that the heat loss effect is an important refinement of the model when the plume has the balloon-on-a-string structure.

3.9 Limits of Applicability

In deriving the new rise law (31), we made several simplifying assumptions. The new rise law will become invalid when these assumptions no longer reflect the physical situation. Two of these assumptions, one implicit and one explicit, appear
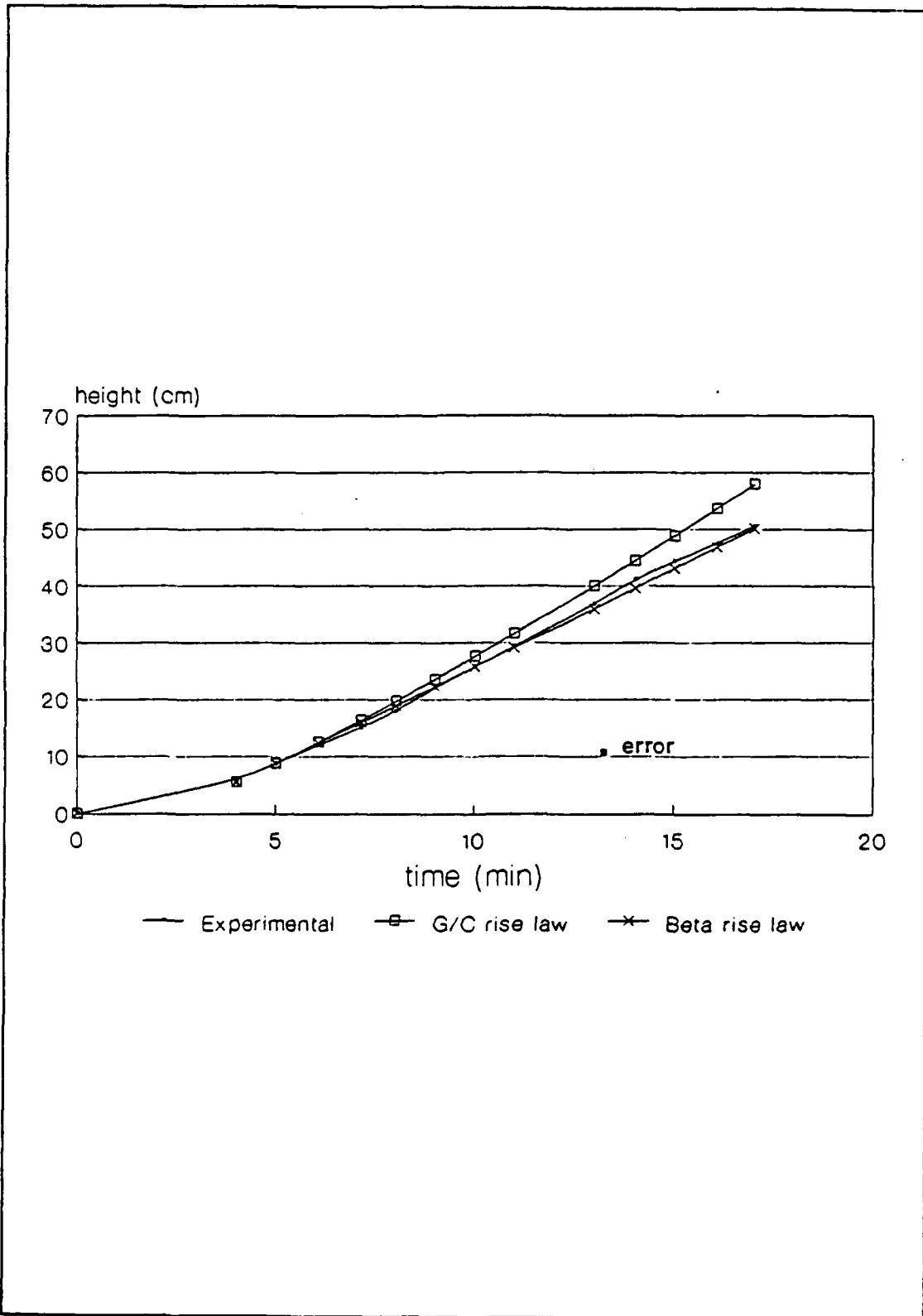
Figure 9. Comparison of new rise law and experiment, $T_{amb}=25C$.
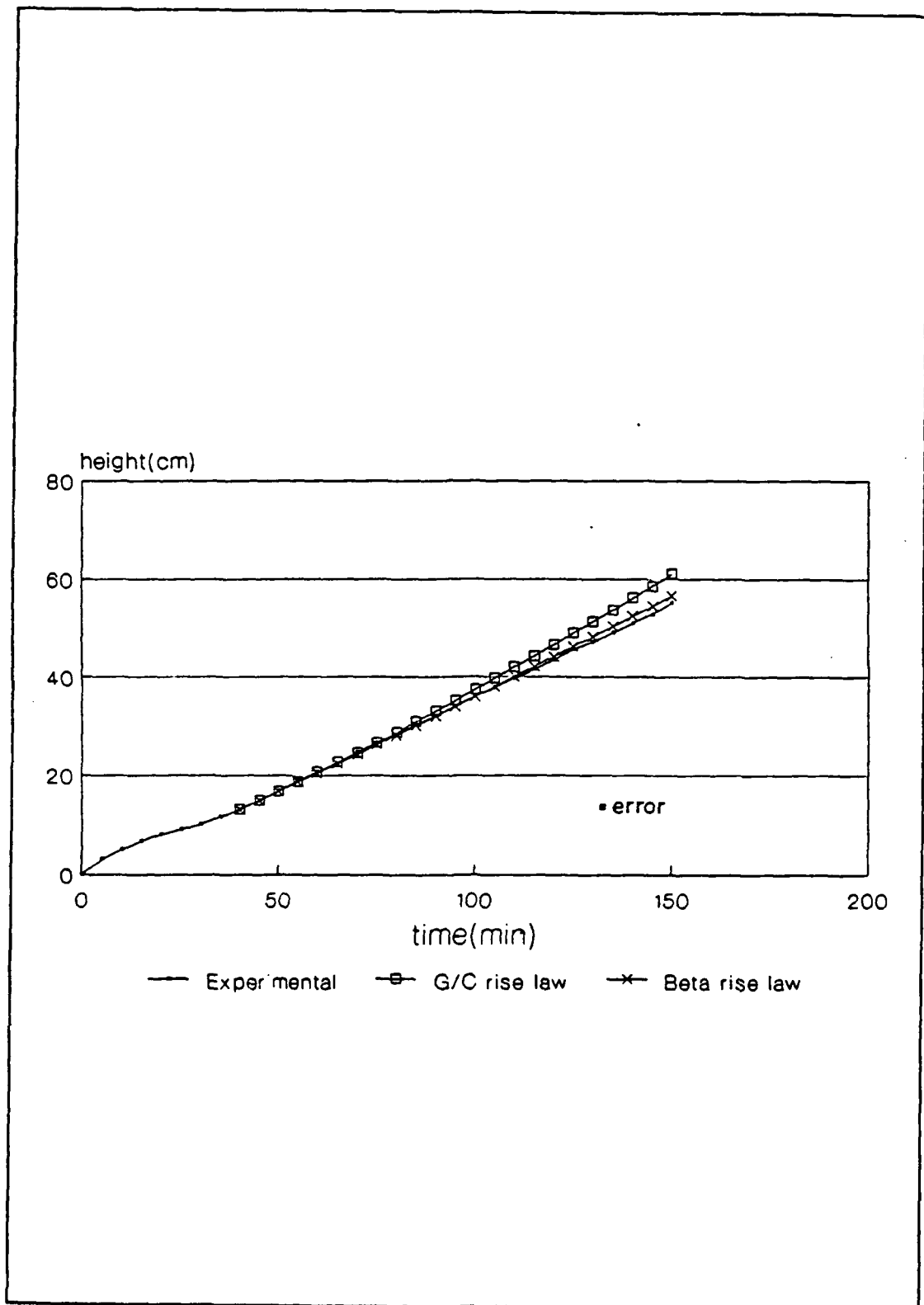
Figure 10. Comparison of new rise law with experiment, $T_{amb}=0.1C$.
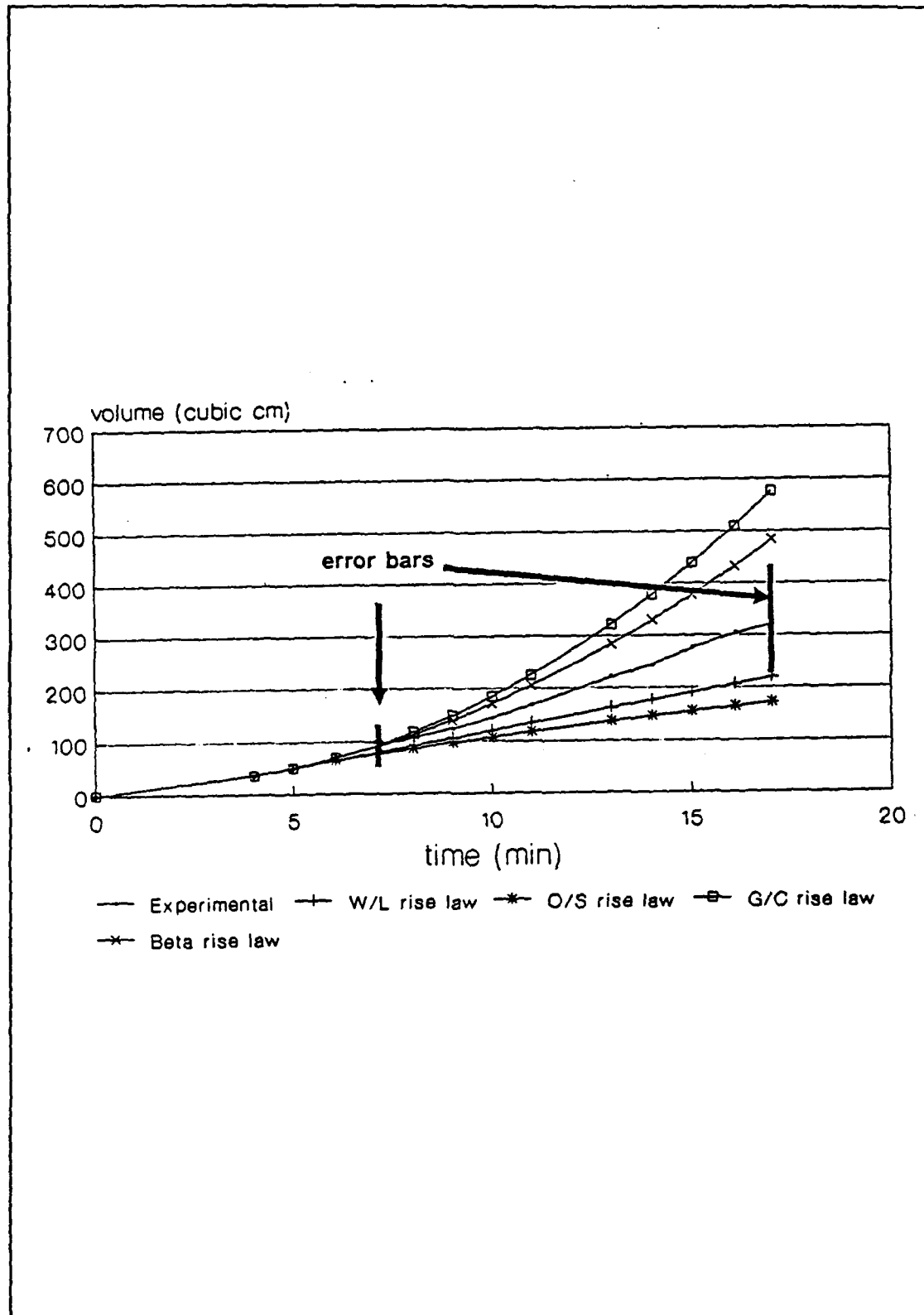
Figure 11. Volume comparison of new rise law and experiment, $T_{amb}=25C$.
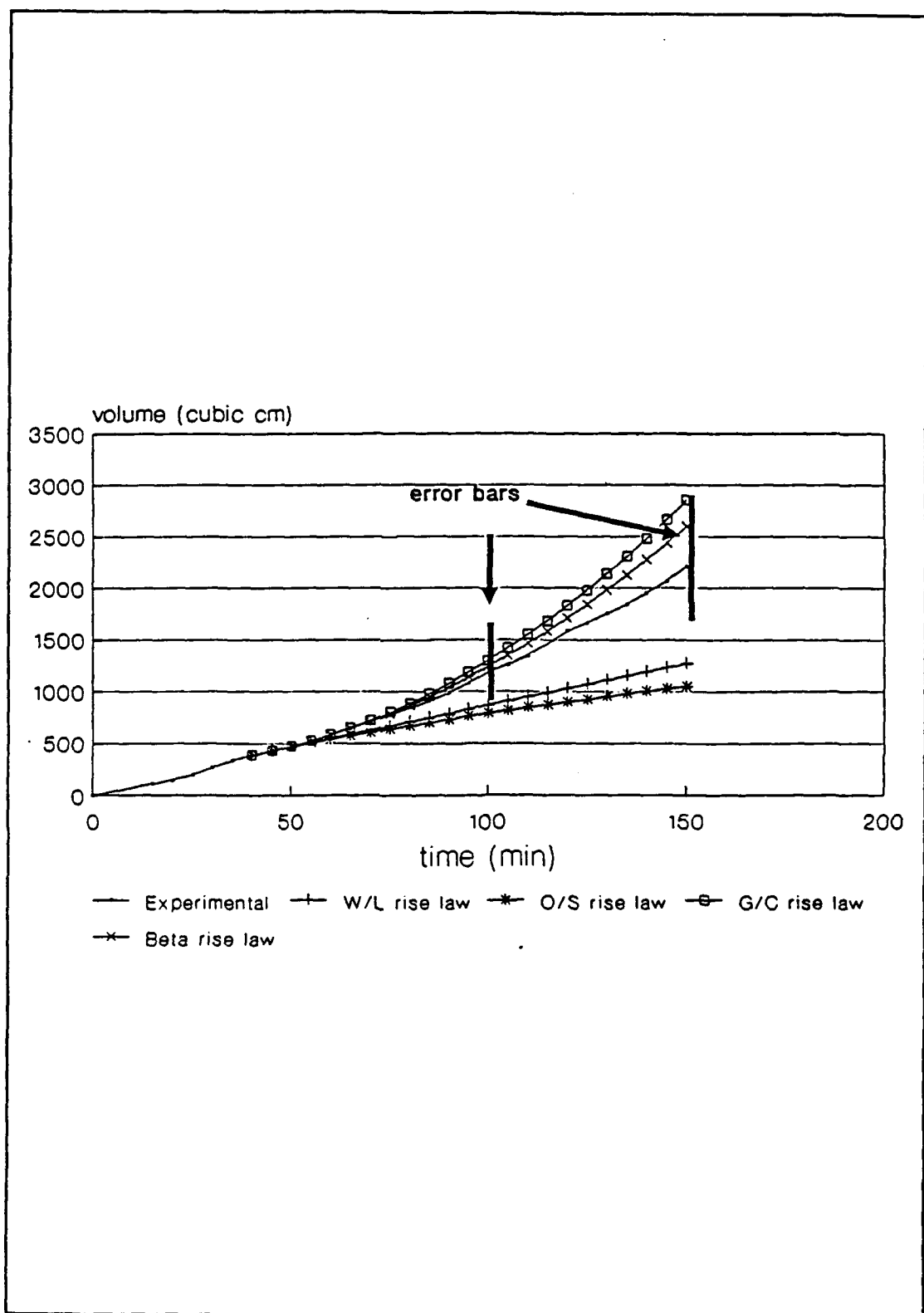
Figure 12. Volume comparison of new rise law and experiment, T_{amb}=0.1C

to present the most severe limitations.

3.9.1 Negligible Conduit Heat Loss

By neglecting the heat lost in the conduit compared to the heat lost in the ball, we assumed that the temperature of the fluid entering the system through the circular surface A in figure 7 was the same as the source temperature of the heater. As the conduit grows in length, this assumption is no longer valid.

To estimate the height at which the conduit length may become important, consider the approximate thermal diffusive thickness,

$$\delta = \sqrt{\frac{\kappa}{t}}.$$

For the conduit, the time scale for this diffusion is U_c/z, where z is the length of the conduit. So, the thermal diffusive thickness becomes

$$\delta = \sqrt{\frac{\kappa z}{U_c}}.$$

Now, as a first approximation, the conduit heat loss will become important when this diffusive thickness equals the conduit radius, r_c. Recalling that

$$U_c = \frac{F}{A_c} = \frac{F}{\pi r_c^2},$$

We have that

$$z_o = \frac{F}{\kappa \pi}$$

where z_o is the height at which conduit heat loss is important.

For the $T_{amb} = 25C$ case, $z_o = 25.2$ cm and for the $T_{amb} = 0.1C$ case, $z_o = 18.8$ cm. This scaling argument, of course, only gives a rough estimate of z_o, but these calculations indicate that heat lost through the conduit may be significant even for

the heights observed in the experimental studies.

3.9.2 Balloon-On-A-String Shape

In describing the system used for the analysis, we implicitly assumed that the plume structure could be modelled as a sphere trailing a narrow conduit. The $T_{amb} = -26.1C$ case did not exhibit this structure. As shown in section 3.8, the new rise law did not apply to this case since the appropriate choice of β was negative, violating the assumption of nonnegative β.

To help understand some of the factors that determine when the balloon-on-a-string shape will occur, consider the theoretical analog of a sphere in an infinite tank of syrup. The sphere has radius a and maintains a vacuum internally (figure 13). The sphere is also able to immediately heat the syrup and reduce its viscosity to zero.

At the surface of the sphere, the normal stress must be continuous, so $\sigma_n = -P + \mu u_r$ (where σ_n is the normal stress) is continuous. Inside the sphere, however, $P = \mu = 0$, so we must have

$$\Delta P = \mu u_r.$$

This idealized situation is analogous to the heater in the tank. For the experiment, then, this ΔP roughly represents the pressure difference needed to pull cold syrup onto the heater surface. If this pressure difference is not available, the heater will draw preheated syrup rather than ambient syrup.

The total pressure head available in the plume is roughly $\Delta \rho H$, where H is the total height of the plume. This total must supply the head to send fluid up the conduit and to draw ambient fluid onto the heater. While the ball is forming on the heater, the pressure head is increased by increasing the size of the ball. When the ball radius is large enough to generate the pressure difference needed to draw ambient fluid, the ball lifts away from the heater and trails the narrow conduit. In
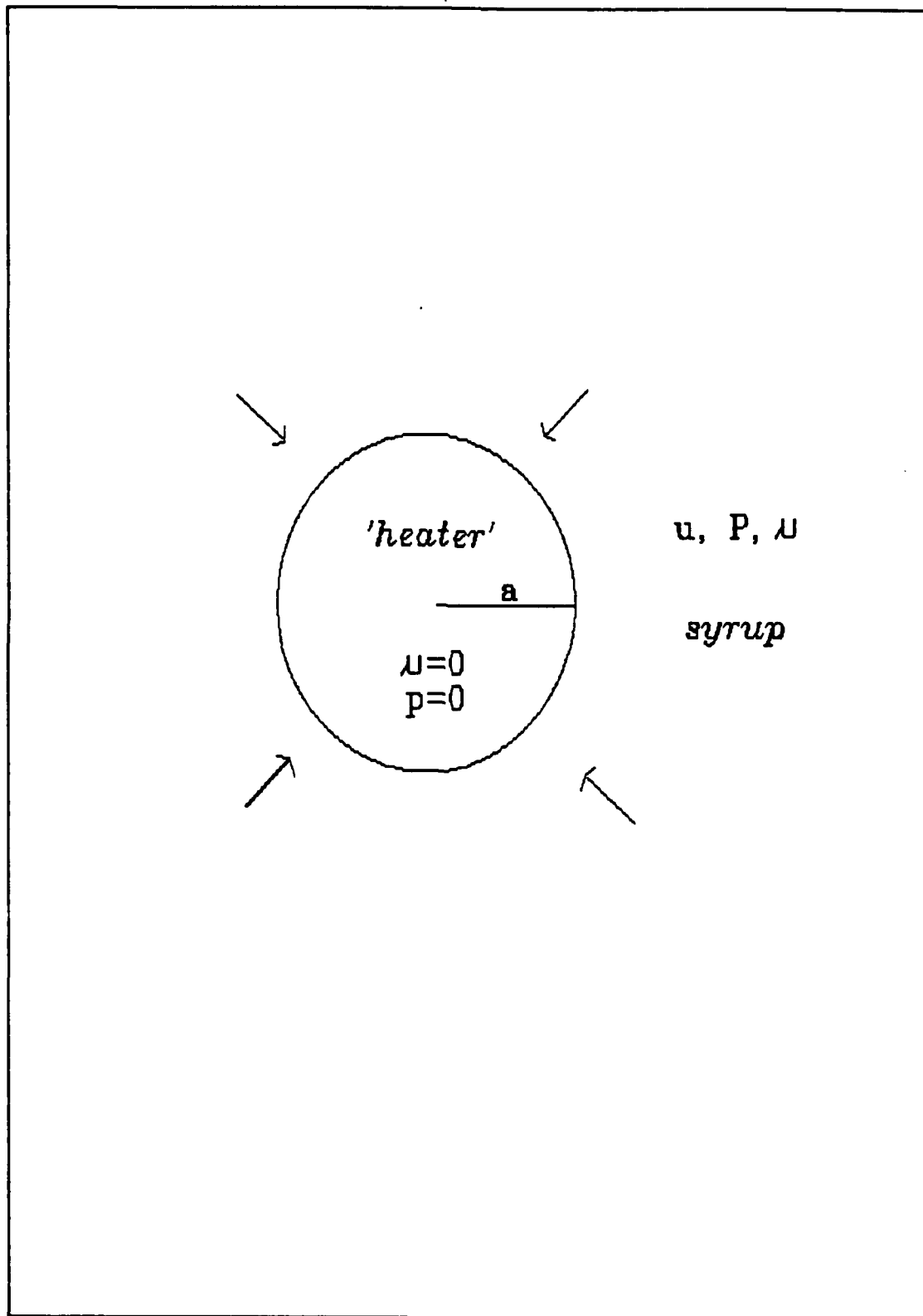
Figure 13. Theoretical analog of heater and tank.

the $T_{amb} = -26.1C$ case, μu_r is so large that the ball is never able to generate enough head to pull in new ambient fluid, so it recycles previously heated fluid.

Using the idealized spherical geometry analog, we can estimate the height needed for liftoff. Since

$$\Delta P = \Delta \rho g H_o = \mu u_r |_{heater\ radius}.$$

and

$$u_r \sim \frac{u}{r_h}$$
$$F = 2\pi r_h^2 u$$

we can solve for the height needed for liftoff,

$$H_o \sim \frac{\mu F}{2\pi \Delta \rho g r_h^3}$$

where r_h is the heater radius

H_o is the height needed for sphere liftoff.

Using this relationship with the experimental parameters, we have

$$H_o|_{25C} \sim .02\ cm$$
$$H_o|_{0.1C} \sim 1.1\ cm$$
$$H_o|_{-26.1C} \sim 3.5 \times 10^3\ cm.$$

For the experiment, liftoff for the $T_{amb} = 25C$ case occurred at approximately 3.5 cm. For the $T_{amb} = 0.1\ C$ case, liftoff occurred at approximately 13 cm. No liftoff occurred for the $T_{amb} = -26.1C$ case.

CHAPTER 4

NUMERICAL MODELLING

4.1 Purpose

An accurate numerical model of starting plume development provides several

significant advantages over the experimental investigation. First, a numerical model

allows the investigation of parameter spaces that were not or could not be explored

in laboratory experiments. Such models also allow more detailed observations than

laboratory experiments. For example, while velocity values may only be observed at

points where instrumentation is available for the experiment, the velocity is known

at each computational node in the numerical model. There are, in general, many

computational nodes throughout the domain of interest, and they are more dense in

regions of rapid flow change. These nodes, therefore, serve as a network of 'sensors'

that are distributed much better than usually allowed in the laboratory environment.

Since a good numerical model will provide the means to run more detailed

'experiments' in a wider parameter range than the laboratory case, verification of

the numerical model is essential. The experimental study of chapter 2 provides an

excellent opportunity to perform such verification. The goal of the numerical model

in this study is to accurately predict the observed behavior of the experiments,

principally the height of the plume as a function of time. In subsequent studies it

may be used to predict creeping thermal plume behavior in other cases with some

confidence.

4.2 Governing Equations

The physical problem is well-described by the continuity equation for incompressible fluids, the Navier-Stokes equations and the energy equation, with the Boussinesq approximation. These equations are given:

$$\frac{\partial u_i}{\partial x_i} = 0 \tag{32}$$

$$\rho \frac{\partial u_i}{\partial t} + \rho u_j \frac{\partial u_i}{\partial x_j} - \rho g_i + \rho g_i \alpha (T - T_{ref}) - \frac{\partial \tau_{ij}}{\partial x_j} = 0 \tag{33}$$

with,

$$\tau_{ij} = -P \delta_{ij} + \mu \left(\frac{\partial u_i}{\partial x_j} + \frac{\partial u_j}{\partial x_i} \right) \tag{34}$$

$$\rho c_p \frac{\partial T}{\partial t} + \rho c_p u_j \frac{\partial T}{\partial x_j} + \frac{\partial q_j}{\partial x_j} = 0 \tag{35}$$

with,

$$q_j = -k \frac{\partial T}{\partial x_j}. \tag{36}$$

and μ varies with temperature as indicated in figure 2 of chapter 2, i. e.,

$\log_{10} \mu = 20.606 - 14.991(1000/T) + 3.0762(1000/T)^2$

Where μ has units mPa-sec and T is in Kelvin units. In equations (32) through (36) t is the time, u_i is the velocity component in the x_i coordinate direction, P is the non-hydrostatic pressure, T is the temperature, ρ is the density, τ_{ij} is the stress tensor, q_i is the heat flux vector, μ is the dynamic viscosity, c_p is the heat capacity, k the thermal conductivity and α is the coefficient of thermal expansion. T_{ref} is a reference temperature for which buoyant forces are zero, δ_{ij} is the identity tensor, and g_i is the gravitational acceleration.

4.3 Boundary Conditions

The computational domain and boundary conditions have been chosen to model the physical situation in the experimental apparatus. The axisymmetry of the plume suggests making the domain axisymmetric with the radial coordinate measured out from the center of the heater. Boundary conditions include the no-slip condition along the top, side, and bottom walls. (Since a relatively thick layer of dried syrup formed on the surface of the fluid, the boundary conditions are set assuming that the vessel is completely enclosed.) Along the axis above the heater, normal velocity and heat flux are zero due to symmetry considerations. Along the bottom, perfect insulation is assumed, excluding the heater. The temperature is assumed to be ambient on the top and side. The heater input is specified as a boundary condition on the bottom, corresponding to the physical size of the heater in the experiment. The value of heat flux was calculated from the resistance of the heater and the applied voltage across the heater. Figure 14 presents a graphical interpretation of the domain and boundary conditions.

4.4 Computational Method

The most common tools for solving incompressible flow problems, such as that

$u = v = 0 \quad T = T_{amb}$

axis of symmetry

$\dot{q} = 0$

$v = 0$

$u = v = 0$

$T = T_{amb}$

heater

$u = v = 0 \quad \dot{q} = 0$ (outside heater)
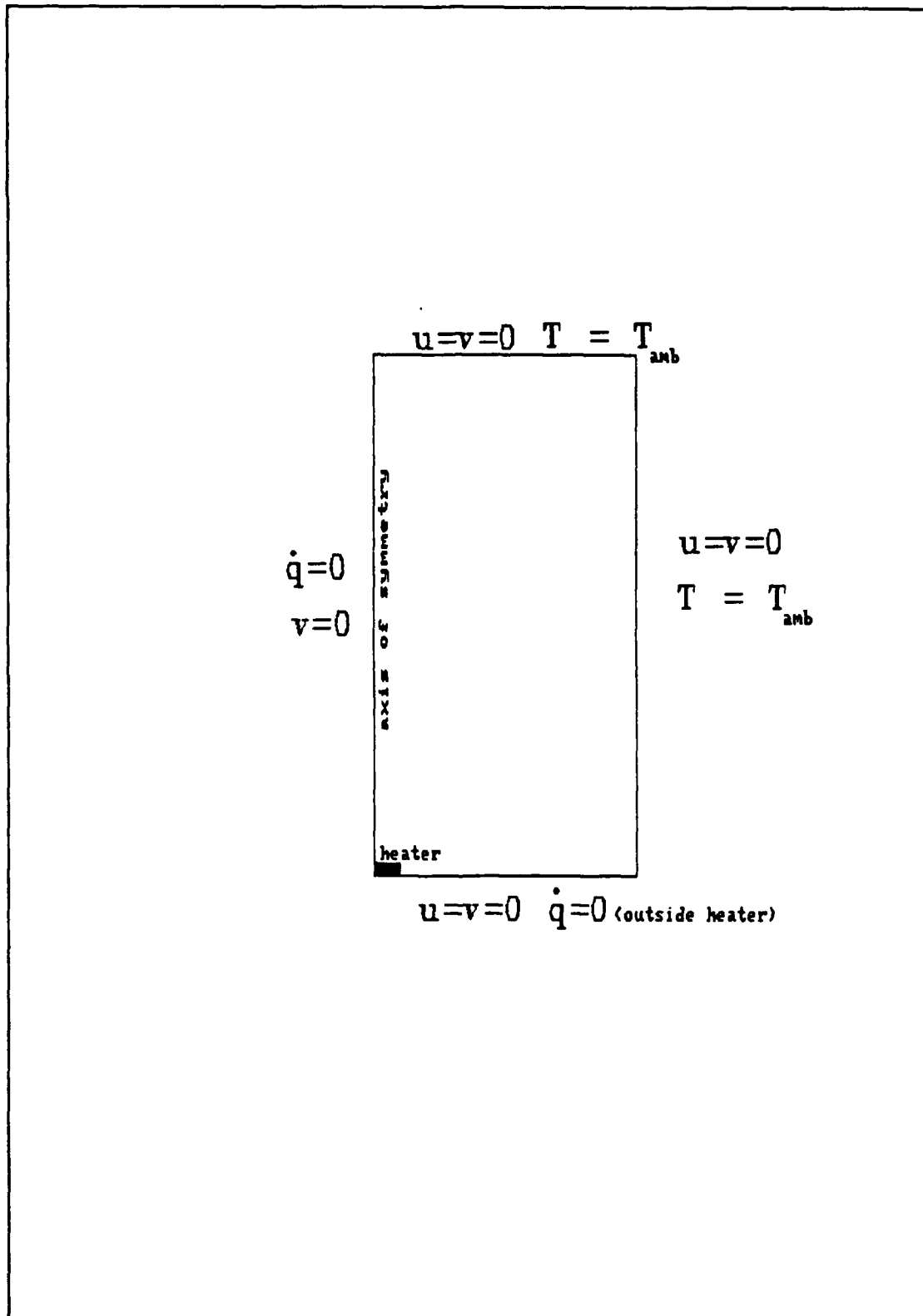
Figure 14. Computational domain and boundary conditions.

described in the previous section, are the finite-difference method (FDM) and the finite-element method (FEM). The technique chosen to construct the numerical model for the plumes was the FEM. The FEM has been the method of choice in the computational fluid dynamics literature for the last few years. The major reasons that FEM was chosen for this problem were the flexibility it provides in choosing the computational grid and the availability of an existing code that was well-suited to the plume problem. The FEM allows a variable mesh to be used when discretizing the domain; the FDM requires that the nodal spacing be equal throughout the domain. This selection flexibility provides the opportunity to make the mesh dense in areas where large gradients occur. For this specific problem, the finer mesh may be used to resolve the large temperature gradients on the boundary of the plume. The finite-element code used to produce the numerical model is named NACHOSII. NACHOSII, written by D. Gartling (1986) at Sandia National Laboratories, is designed for two-dimensional planar or axisymmetric analysis of viscous, incompressible flows, including the effects of buoyancy and heat transfer. A more complete description of NACHOSII will be given in section 4.9.1.

The brief description of the FEM presented here is practically and computationally oriented. A large body of literature describes the more theoretical aspects of the technique. Two excellent references that address the FEM from theory and application to fluid flow problems are Gunzburger (1989) and Cuvelier, et. al. (1986). The following discussion, based largely on Gartling (1986), describes the FEM in general terms; specific application to the plume problem is given in section 4.10.

The FEM begins by subdividing the domain of interest into a number of geometrically simple regions called finite elements. Within each element, the desired unknowns (u_i, P, T) are located at specified points called nodes. These unknowns are

interpolated by some suitable interpolation function at the nodes. The proper choice

of the elements and interpolation functions is crucial to the success of the FEM.

Requirements for this choice will be considered in a later section. Using the

notation of Gartling (1986), the unknowns, $\bar{u}_j$, $\bar{P}$, and $\bar{T}$ at a general point x_i within

an element may be written as a vector product of the interpolation functions Φ, Ψ,

and Θ, and the corresponding nodal values:

$$u_j(x_i,t) = \bar{\Phi}^T(x_i)\bar{u}_j(t)$$
$$P(x_i,t) = \bar{\Psi}^T(x_i)\bar{P}(t)$$
$$T(x_i,t) = \bar{\Theta}^T(x_i)\bar{T}(t).$$

The superscript T denotes transpose.

Substituting these expressions into the governing equations (32) - (36) yields

the following set of equations.

Momentum:

$$\bar{f}_{u_1}(\bar{\Phi},\bar{\Psi},\bar{\Theta},\bar{u}_i,\bar{P},\bar{T}) = \bar{R}_{u_1}$$
$$\bar{f}_{u_2}(\bar{\Phi},\bar{\Psi},\bar{\Theta},\bar{u}_i,\bar{P},\bar{T}) = \bar{R}_{u_2}$$

Continuity:

$$\bar{f}_P(\bar{\Phi},\bar{u}_i) = \bar{R}_P$$

Energy:

$$\bar{f}_T(\bar{\Phi},\bar{\Theta},\bar{u}_i,\bar{T}) = \bar{R}_T$$

These equations will, of course, no longer be an exact representation of the physical

interactions described by (32) - (36). The amount that they differ due to the

interpolation approximation is represented by the residuals, or errors, denoted by R_{u1}, R_{u2}, R_P, R_T. The FEM seeks to minimize these residuals in some weighted sense.

The particular FEM used to model the plumes is a Galerkin method. In this technique, the residuals are minimized by making them orthogonal to the interpolations functions over each element. This condition may be expressed as

$$
\begin{aligned}
\langle \vec{\Phi}, \vec{R}_{u_1} \rangle &= \langle \vec{\Phi}, \vec{f}_{u_1} \rangle = 0 \\
\langle \vec{\Phi}, \vec{R}_{u_2} \rangle &= \langle \vec{\Phi}, \vec{f}_{u_2} \rangle = 0 \\
\langle \vec{\Psi}, \vec{R}_P \rangle &= \langle \vec{\Psi}, \vec{f}_P \rangle = 0 \\
\langle \vec{\Theta}, \vec{R}_T \rangle &= \langle \vec{\Theta}, \vec{f}_T \rangle = 0
\end{aligned}
\tag{37}
$$

where $\langle .,. \rangle$ is defined as

$$
\langle \vec{a}, \vec{b} \rangle = \int_{\Omega} \vec{a} \cdot \vec{b} \, d\Omega
$$

with Ω being the area of an element.

The Galerkin method reduces the governing partial differential equations (32) - (36) to a nonlinear system of ordinary differential equations in time. The unknowns of this system are $(\vec{u}_j, \, \vec{P}, \, \vec{T})$ for each element. The coefficients of the system are derived from the integrals represented by the inner products in equation (37). The details of this manipulation are described in the appendix. The results can be expressed in matrix form as follows

momentum:

$$
M \frac{d\vec{U}}{dt} + C(\vec{U})\vec{U} - Q\vec{P} + K(\vec{U}, \vec{T})\vec{U} + B(\vec{T})\vec{T} = \vec{F}(\vec{T})
\tag{38}
$$

continuity:

$$-Q^T \vec{U} = \vec{0} \tag{39}$$

energy:

$$N\frac{d\vec{T}}{dt} + D(\vec{U})\vec{T} + L(\vec{T})\vec{T} = \vec{G}(\vec{T},\vec{U}) \tag{40}$$

where

$$\vec{U}^T = (\vec{u}^T_1, \vec{u}^T_2) \tag{41}$$

Each of these element matrices and vectors has a physical meaning associated with the terms in the governing equations. The M and N matrices represent the mass and heat capacity terms in the momentum and energy equations, respectively. C and D are the result of the advection terms in the momentum and energy equations. K and L represent the diffusion terms. The Q matrix is the gradient operator while Q^T is the divergence operator. The B matrix represents the buoyancy term from the Boussinesq approximation. $\vec{F}$ and $\vec{G}$ allow for forcing functions in the system; for this problem, $\vec{F}$ is zero. These physical interpretations are very helpful in analyzing the method's performance for the given plume application. The exact integral expressions for these matrices are given in the appendix. Once the matrices are developed for one element, the global matrix system may be assembled from the element matrices by addition, i. e.,

$$M_{global} = \sum_{e=1}^{nelm} M^{(e)}$$

$$C_{global} = \sum_{e=1}^{nelm} C^{(e)}$$

etc.

where nelm is the total number of elements in the grid. Note that the global system has the identical form of (38) - (41), where the matrices represent global matrices.

Equations (38) - (41) may then be combined into a single matrix equation

$$\begin{pmatrix} M & 0 & 0 \\ 0 & 0 & 0 \\ 0 & 0 & N \end{pmatrix} \begin{pmatrix} \dfrac{d\vec{U}}{dt} \\ \dfrac{d\vec{P}}{dt} \\ \dfrac{d\vec{T}}{dt} \end{pmatrix} + \begin{pmatrix} C(\vec{U})+K(\vec{U},\vec{T}) & -Q & B(\vec{T}) \\ -Q^T & 0 & 0 \\ 0 & 0 & D(\vec{U}) + L(\vec{T}) \end{pmatrix} \begin{pmatrix} \vec{U} \\ \vec{P} \\ \vec{T} \end{pmatrix} = \begin{pmatrix} \vec{F}(\vec{T}) \\ \vec{0} \\ \vec{G}(\vec{T},\vec{U}) \end{pmatrix} \quad (42)$$

or,

$$\overline{M}\frac{d\vec{V}}{dt} + \overline{K}(\vec{U},\vec{T})\vec{V} = \overline{F}(\vec{U},\vec{T}) \quad (43)$$

where

$$\vec{V}^T = (\vec{u}_1{}^T, \vec{u}_2{}^T, \vec{P}^T, \vec{T}^T).$$

There are two common methods for solving the matrix system (42): the mixed or integrated FEM and the penalty FEM.

4.4.1 Integrated Finite Element Method

The integrated FEM is a straightforward extension of the process described

above. The system of ordinary differential equations in time is solved for velocity, pressure and temperature at each time step

4.4.2 Penalty Finite Element Method

In contrast to the integrated FEM, the penalty FEM eliminates pressure as an unknown in the matrix system. Since a large part of the cost of any FEM is the solution of the matrix system, the penalty method generally has reduced computational and storage costs when compared to the integrated FEM. The theoretical background for the penalty method comes from the application of constrained optimization theory to a linearized form of (32) and (33). Let us briefly consider this form in order to develop the equations used in the penalty method. When the advection and buoyancy terms in (32) are dropped, the resulting linear equations are commonly called the Stokes equations

$$\rho \frac{\partial u_i}{\partial t} - \frac{\partial \tau_{ij}}{\partial x_j} = 0$$

$$\frac{\partial u_i}{\partial x_i} = 0$$

This problem may be recast as a minimization problem where the momentum equation is constrained by the continuity equation. A standard method of enforcing such a constraint is the method of Lagrange multipliers with penalization (Girault and Raviart, 1986). This approach explains the use of the term penalty for this method.

Returning now to the nonlinear problem (32) - (36), recall that it has no known equivalent minimization form, but the penalty method may be applied to this problem by using a slightly different approach. When the minimization form of the Stokes problem is solved by the penalty method, the corresponding Euler-Lagrange equations are identical to the Stokes equations, except that the continuity equation is

relaxed, i. e.,

$$\frac{\partial u_i}{\partial x_i} = -\epsilon P.$$

The parameter ϵ is the penalty parameter. Note that the continuity equation is recovered as ϵ goes to zero. One can think of this as a pertubation to the continuity equation that introduces some small compressibility into the system.

Applying this perturbation to the continuity equation (32), approximating the velocity and pressure with the interpolation functions, and using the Galerkin procedure gives

$$\left(\int_\Omega \vec{\Psi} \frac{\partial \vec{\Phi}}{\partial x_i} d\Omega \right) \vec{u}_i = -\left(\int_\Omega \epsilon \vec{\Psi} \vec{\Psi}^T d\Omega \right) \vec{P}.$$

Or, in matrix form

$$Q^T \vec{U} = -\epsilon M_p \vec{P}$$

where

$$M_P = \int_\Omega \vec{\Psi} \vec{\Psi}^T d\Omega.$$

Solving the matrix equation for P gives

$$\vec{P} = -\frac{1}{\epsilon} M_P^{-1} Q^T \vec{U}.$$

This equation allows pressure to be eliminated from the global matrix system. The

global system for the penalty method, therefore, may be written as a matrix equation

$$\begin{pmatrix} M & 0 \\ 0 & N \end{pmatrix}\begin{pmatrix} \dfrac{d\vec{U}}{dt} \\ \dfrac{d\vec{T}}{dt} \end{pmatrix} + \begin{pmatrix} C(\vec{U})+K(\vec{U},\vec{T})+K_P & B(\vec{T}) \\ 0 & D(\vec{U})+L(\vec{T}) \end{pmatrix}\begin{pmatrix} \vec{U} \\ \vec{T} \end{pmatrix} = \begin{pmatrix} \vec{F}(\vec{T}) \\ \vec{G}(\vec{T},\vec{U}) \end{pmatrix}$$

where

$$K_P = \frac{1}{\epsilon} Q M_P^{-1} Q^T.$$

After the system is solved for the velocity, the pressure may be recovered using the matrix form of the perturbed continuity equation.

Note that to allow for easy element-level construction and subsequent global matrix assembly of the K_P matrix, it is necessary that the terms of M_P^{-1} be easily constructed, i. e., M_P must be invertible at the element level. Since M_P is defined in terms of the pressure interpolation functions, Ψ, these functions may only be defined within an element, i. e., they can be discontinuous between elements. For this reason, the pressure interpolation functions for the penalty method will always be discontinuous between elements.

4.4.3 Iterated Penalty Method

Gunzburger (1989) describes an iterated penalty approach that enforces the incompressibility condition using an iterative application of the perturbation of the continuity equation. The algorithm is given as

1. Given P^{n-1}, solve for $\vec{U}^n$, $\vec{T}^n$

$$M\frac{d\vec{U}^n}{dt} + C(\vec{U}^n)\vec{U}^n - Q\vec{P}^{n-1} + K(\vec{U}^n,\vec{T}^n)\vec{U}^n + B(\vec{T}^n)\vec{T}^n = \vec{0}$$

$$N\frac{d\vec{T}^n}{dt} + D(\vec{U}^n)\vec{T}^n + L(\vec{T}^n)\vec{T}^n = \vec{0}$$

2. Update

$$\vec{P}^n = \vec{P}^{n-1} + \frac{1}{e}M_p^{-1}Q^T\vec{U}^n$$

(This step is based on a perturbation to the continuity equation.)

3. If discrete divergence is too large repeat. (The traditional penalty method occurs in the method when $P_o = 0$ and steps 2 and 3 are performed only once.) Results of numerical experiments with this method were generally poorer than those found with the Uzawa algorithm described later (4.9.4). It is included here as a reference to compare with the Uzawa algorithm.

4.4.4 <u>Time Integration</u>

Both the integrated and penalty FEM provide a spatial discretization that results in a system of first-order ordinary differential equations in time. The solution of the system is found by finite differencing in time; see Strikwerda (1989) and Sod (1984). In the NACHOSII code, a predictor-corrector method is employed that uses an explicit time-differencing for the predictor and an implicit method for the corrector. The implicit differencing is unconditionally stable for all choices of time steps and thus avoids severe restrictions in the choice of the time step. A choice of first-order or second-order methods is available. The first-order method uses a forward Euler predictor and backward Euler corrector. The second-order method uses Adams-Bashforth predictor and trapezoid corrector. The second order methods have the advantage of increased accuracy while the first order Euler methods have

damping characteristics that are often helpful in smoothing the starting conditions in the initial stages of a problem. Automatic time-step control is also provided with both methods.

4.5 Element Choice

This choice of elements for a finite-element model is a matter of determining the appropriate geometry (e. g., triangular or quadrilateral) and the order of the interpolation functions defined on the element. The regular, quadrilateral shape of the computational domain suggested the use of quadrilateral elements. NACHOSII provides an element library that includes an eight-node quadrilateral and a nine-node quadrilateral (figure 15). These elements will be considered specifically in the following discussion.

Furthermore, the choice of the order of the interpolation functions is an important consideration. Cuvelier, et. al. (1986) describe necessary conditions for these functions. When Green's formula is applied to the Galerkin form of the governing equations (equation (37) and the appendix), first-order derivatives of the velocity interpolation functions occur, but the pressure interpolation functions are not differentiated. This means that the velocity functions must be continuously differentiable in each element and continuous in the whole domain. The pressure functions, however, need only be continuous in each element; they may be discontinuous between elements. Cuvelier, et. al. (1986) also indicate that, in order to prevent the velocity approximation from being totally specified by the continuity equation, one generally requires that the pressure interpolation functions be at least one order less than the velocity interpolation functions.

NACHOSII gives several interpolation choices that are consistent with these criteria. In each choice, the same interpolation function is used for temperature and
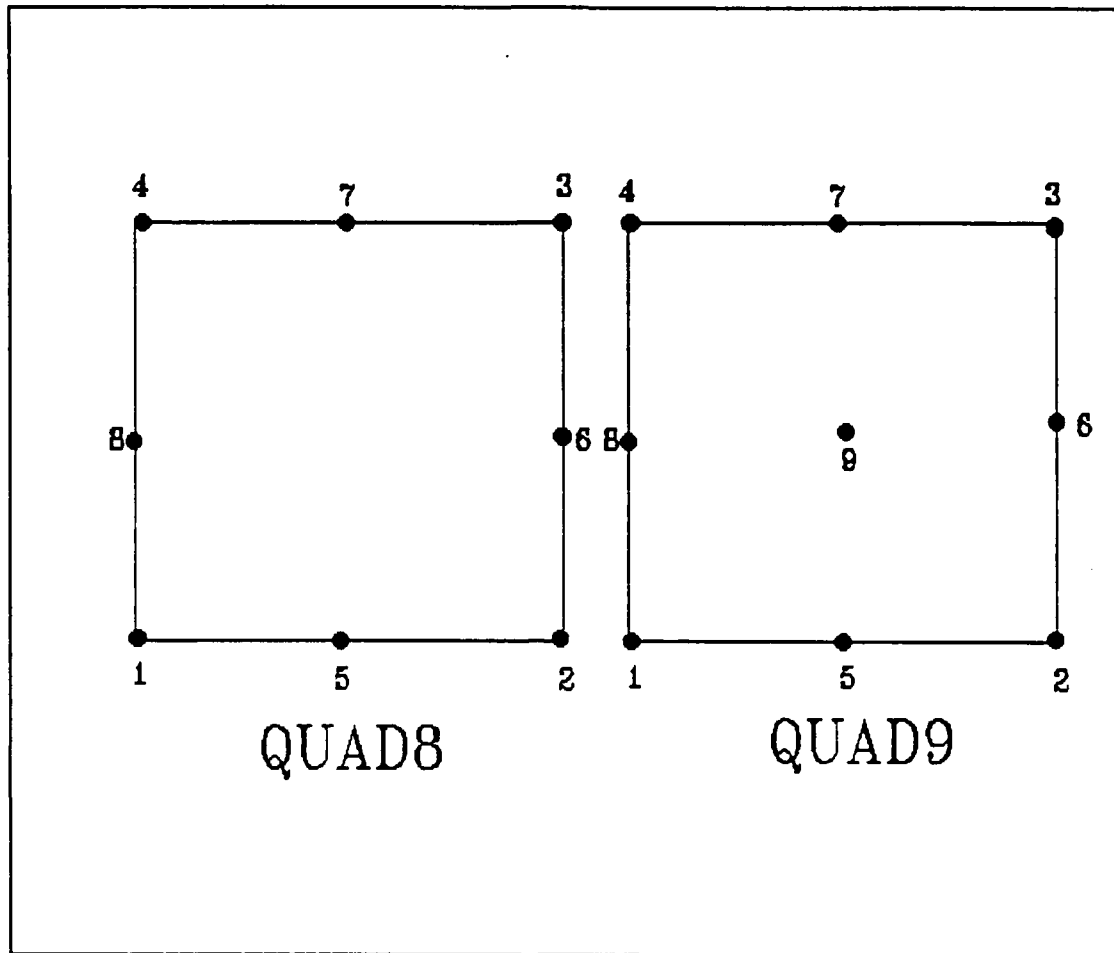
Figure 15. Eight and nine node quadrilateral elements.

velocity components. For velocity, biquadratic, continuous interpolation functions

may be used for the eight-node quadrilateral (QUAD8) or the nine-node

quadrilateral (QUAD9). For the pressure approximation, one may choose continuous,

bilinear functions or discontinuous linear functions.

The element and interpolation choices are crucial to the success of the

Galerkin FEM since they determine which discrete finite-element subspace is used to

approximate the solution. This choice is the topic of much current research. The

following discussion gives some basic theoretical guidlines. Gunzburger (89) gives a

description of which spaces are allowed for approximating equations (32) - (36).

Choosing velocity, pressure, and temperature interpolations arbitrarily will often

lead to poor results. In incompressible flow calculations, the most difficult condition
to satisfy is the divergence-free condition (32). Gunzburger (1989) also discusses a
key theoretical condition that relates to the satisfaction of the continuity equation
(32). It is known as the Ladyzhenskaya-Babuska-Bressi (LBB), the inf-sup, or the
div-stability condition. Girault and Raviart (1986) give a complete discussion of this
condition, along with various proofs for several elements. There are several
equivalent statements of the div-stability condition; proof of this condition is not
trivial and will not be attempted here. One important product of this condition is
that it allows us to predict the convergence rate of the FEM:

$$|\vec{u} - \vec{u}^d|_1 + |P - P^d|_0 + |T - T^d|_1 = O(d^{\min(k,l+1)})$$

where

$$\vec{u} = (u_1, u_2)$$
$$(p,q) = \int_\Omega pq\, d\Omega$$
$$|q|_0 = (q,q)^{1/2}$$
$$|q|_1 = \left(\sum_{i=1}^{n} \left\| \frac{\partial q}{\partial x_i} \right\|_0^2 \right)^{1/2}$$

and the superscript d denotes the computed solution. The parameters k and l are the
orders of the velocity (or temperature) and pressure interpolations respectively.
Note that d is a parameter that relates to the size of the mesh spacing. The QUAD9
elements with continuous and discontinuous pressure approximation satisfy the div-
stability condition (Girault and Raviart, 1986; Gunzburger, 1989). The QUAD8
elements with discontinuous and continuous pressure approximation do not satisfy

the div-stability condition in the global sense. However, they do satisfy the condition in a local sense, and this consideration allows the same rate of convergence to be proven for these elements as for the continuous pressure elements (Girault and Raviart, 1986). So, from a rate of convergence point of view, none of the quadrilateral elements has any theoretical advantage.

Another consideration in choosing appropriate elements is the phenomenon often called mesh locking. Roughly speaking, in satisfying the continuity equation (32), some elements enforce too many incompressibility constraints. When this happens, the only solution is the trivial (or locked) solution. Elements that satisfy ·the div-stability condition will not lock. The mathematical analysis of this condition is beyond the scope of this paper. Hughes (1986) presents a heuristic method to determine an element's propensity to lock. While this method is not rigorous, it provides some means of comparing the effectiveness of different elements to model incompressible flow. The following paragraph is a summary of this method of constraint counting.

On a standard mesh for a two dimensional problem, let n_{eq} be the total number of velocity equations after boundary conditions have been imposed and let n_c be the total number of incompressibility constraints as specified by pressure nodes. Define the constraint ratio, r, by

$$r = \frac{n_{eq}}{n_c}.$$

The idea behind the method is that r should mimic the behavior of the number of equilibrium equations divided by the number of incompressibility conditions for the governing system of partial differential equations (i. e., the number of space dimensions and 1, respectively). In two dimensions, then, the ideal value for r is 2.

A value less than 2 would indicate a tendency to lock while a value greater than 2 indicates that not enough incompressibility constraints are present. A value of r that is less than or equal to 1 indicates more constraints than degrees of freedom and severe locking is expected. For two-dimensional problems, the following rules summarize the method:

r > 2 too few incompressibility constraints

r = 2 optimal

r < 2 too many incompressibility constraints

r ≤ 1 locking

Table 4. Div-stability and mesh locking for elements.

Element	r	LBB satisfied?
QUAD 8, disc P	2	no
QUAD 8, cont P	6	no
QUAD 9, disc P	2 2/3	yes
QUAD 9, cont P	8	yes

The div-stability condition, roughly speaking, insures that locking will not occur, however, it does not guarantee an optimal value of r. Note that a value of r greater than two may imply that the incompressibility condition is not adequately satisfied, so an element may satisfy the div-stability condition (so it won't lock), yet it may not enforce the incompressibility condition adequately. Table 4 summarizes the div-stability and locking characteristics of the elements available in NACHOSII. The r values indicate that none of the elements being considered will lock; QUAD8 discontinuous pressure has the optimal r value.

Pelletier, et. al. (1989) show that a discontinuous pressure approximation is more effective in modelling the divergence-free condition than a continuous

pressure approximation. Their argument is based on element mass conservation and the degrees of freedom required. This latter argument considers the dual role of pressure. In the integral form of the continuity equation (appendix), the pressure approximation must enforce the continuity equation. Additionally, the pressure approximation must balance the viscous and buoyancy terms in the momentum equation. The pressure must adjust itself, then, to satisfy the continuity equation while matching the needed balance in the momentum equation. There must be enough pressure degrees of freedom to satisfy both of these requirements. One way to enlarge the pressure space is to move from a continuous pressure approximation to a discontinuous pressure approximation.

4.6 Discrete Divergence

To this point, we have described the FEM in general terms. We have considered the general procedure, the mixed and penalty methods, and the choice of elements and interpolation functions without applying any methods to the plume problem. From this point forward, we will focus on the plume problem application. The basic theory that we've considered so far provides some assistance in choosing which method and element is best suited for this problem, but we need additional tools to determine which method will give the best results for the plume application. The experience of our calculations will show that computing the discrete divergence is a good diagnostic for making decisions for practical applications like the plume problem.

As suggested by the previous discussion of the div-stability condition, one of the most difficult aspects of numerically modelling incompressible flow is the satisfactions of the continuity equation. This difficulty is compounded in the plume problem by the strong relationship between viscosity and temperature. This

relationship results in a problem with strong coupling between the energy and momentum equations. It also provides regions of high viscosity gradients, for example, at the boundary of the plume.

Pelletier, et. al. (1989) proposed a simple diagnostic tool for measuring the effect of large (constant) viscosity and large viscosity contrast on incompressible flows. They argued that traditional approaches often resulted in poor solutions because of poor satisfaction of the continuity equation or the divergence-free condition (even when the elements used satisfied the div-stability condition!), and they suggested that computing an approximation to the divergence of the velocity field (i. e., a 'discrete divergence') is an inexpensive measure of the reliability of the solution.

In order to study the effects of viscosity variation on the plume problem, NACHOSII was modified to report the discrete divergence at each time step. Following Pelletier, et. al. (1989), the discrete divergence was computed as

$$DDIV = \max_{nelm} \left| Q^T \vec{U}_N \right|$$

where $\vec{U}_N$ is the velocity vector on an individual element, N. The maximum is taken over all elements.

This modification was easy to implement, and relatively inexpensive to compute, since for each element, the matrix equivalent of the divergence operator, Q^T, was already computed. The product $Q^T\vec{U}$ provided the 'components' of the discrete divergence; the maximum of the absolute values of these components was chosen for the discrete divergence. FEM theory predicts that the discrete divergence should be on the order of machine zero (10^{-15} for the Cray-YMP used for the calculations) for integrated FEM and on $O(\epsilon)$ for penalty FEM for a solution demonstrating acceptable mass conservation.

In practical computations, the discrete divergence served as a good indicator of the reliability of the solution. In tests of the mixed and penalty FEM, the discrete divergence would generally increase by one or two orders of magnitude before a problem occurred in the solution. This problem may be a matrix ill-conditioning error or an unrealistic value of velocity or temperature. This behavior of the discrete divergence was confirmed for constant viscosity and variable viscosity applications. Experience has shown that the change in the discrete divergence is a conservative diagnostic, i. e., an increase in discrete divergence does not always signal a problem. It does, however, provide an inexpensive means of testing a solution and we will use it as an indicator of which scaling, element, and method is best suited for modelling the plume problem.

4.7 Scaling

Using a dimensionless form of equations (32) - (36) has several advantages over the dimensional form. One advantage is that such scaling can provide an indication of the relative importance of terms in the equations. Dimensionless forms can also reduce the differences in the magnitudes of different terms in the equations. Most related numerical studies (table 1) cast equations (32) - (36) in Prandtl number-Rayleigh number form by making the following substitutions:

$$t'=\frac{t\kappa}{h^2}, \ x'=\frac{x}{h}, \ u'=\frac{uh}{\kappa}, \ P'=\frac{Ph^2}{\kappa\mu_r}, \tag{44}$$

$$\tau_{ij}'=\frac{h^2\tau_{ij}}{\mu_r\kappa}, \ T'=\frac{T}{\Delta T}, \ \mu'=\frac{\mu}{\mu_r} \tag{45}$$

where ΔT_S is $T_{heater} - T_{amb}$, h is height of tank, μ_r is the viscosity of the ambient fluid. These substitutions put the equations in the following form (dropping primes for nondimensional variables):

$$\frac{\partial u_i}{\partial x_i} = 0$$

$$\frac{1}{Pr}(\frac{\partial u_i}{\partial t} + u_j\frac{\partial u_i}{\partial x_j}) - Ra[(T - T_{ref})]\vec{e}_z - \frac{\partial \tau_{ij}}{\partial x_j} = 0$$

$$\frac{\partial T}{\partial t} + u_j\frac{\partial T}{\partial x_j} - \frac{\partial^2 T}{\partial x_j^2} = 0.$$

with,

$$\tau_{ij} = -P\delta_{ij} + \mu(\frac{\partial u_i}{\partial x_j} + \frac{\partial u_j}{\partial x_i})$$

This Pr-Ra scaling is commonly used for modelling Benard-type problems for a thin layer of fluid. In these types of problems, one may study the effects of increasing buoyancy by increasing the Rayleigh number. One generally associates the Rayleigh number with the temperature difference across the thin layer, or, alternatively, with the heat input to the thin layer. When this type of scaling is applied to the

experiment described in chapter 2, the Rayleigh number is very large due to the large height of the tank. For T_{amb} = 25C, the Rayleigh number is 6.5 X 10^6 and for T_{amb} = 0.1C, the Rayleigh number is 8.5 X 10^4. These large values of Ra place too much weight on the buoyancy term in the momentum equation in the Pr-Ra scaling.

This imbalance potentially creates rounding errors in the solution of the FEM matrix equations which result in a discrete divergence that is too large. The global matrix terms corresponding to the buoyancy force (terms of matrix **B** in equation (42)) are much larger than those of the pressure and viscous terms (terms in matrices **Q** and **K**, respectively, in equation (42)). For some cases, this size difference measured as large as 10^6. These large discrepancies create the possibility of round-off errors and poor matrix conditioning. In fact, these errors accumulate quickly, preventing successful time integration. As a result, no successful Pr-Ra scaled cases ran to completion despite numerous attempts using many different grids. Table 5 illustrates the effect on discrete divergence of increasing Ra on an otherwise unchanged problem. Note that the values in this table were for a mixed method calculation, but similar results hold for penalty methods. The increase in discrete divergence implies that mass is not conserved in the solution for larger values of Ra.

Table 5. Effect of Ra on discrete divergence.

Ra	Discrete Divergence
1.0 X 10^4	~10^{-5}
1.0 X 10^5	~10^{-4}
1.0 X 10^6	~10^{-3}

One alternative to correct this scaling imbalance is to consider a thinner layer of fluid. For example, one may study the plume formation and travel in the bottom

fourth of the tank. A similar approach was used by Olson, et. al. (1987) for studying plume formation. One goal, however, of this numerical study was to test the rise laws found in chapter 3 for the full plume flight path, and to consider the effectiveness of the rise laws in other geometries in later studies. Restricting the depth of fluid would severely hamper the utility of the numerical model for studies of developed plumes.

The approach used, instead, for the numerical model in this study was to rescale equations (32) - (36) to balance the appropriate terms in the equations based on the important physical interactions in the problem. During the ball formation and rise, the key balance of forces in the momentum equation (33) occurs between the buoyancy, pressure, and viscous forces. The inertia terms will have a relatively small effect. With this balance in mind, nondimensionalize the governing equations with the following substitutions:

$$u' = \frac{u}{u_o} \; ; \; t' = \frac{tu_o}{L} \; ; \; x' = \frac{x}{L}$$

$$T' = \frac{T}{\Delta T_s} \; ; \; \mu' = \frac{\mu}{\mu_r} \; ; \; P' = \frac{P}{\rho g \alpha \Delta TL}$$

where

$$L = \sqrt[3]{\frac{\mu_r \kappa}{\rho g \alpha \Delta T_s}}$$

$$u_o = \frac{\kappa}{L}$$

$$\Delta T_s = T_{heater} - T_{amb}$$

$$\mu_r = \mu_{amb}$$

These substitutions put the equations in the following form (dropping primes for

nondimensional variables)

$$\frac{\partial u_i}{\partial x_i} = 0 \qquad (46)$$

$$\frac{1}{Pr}(\frac{\partial u_i}{\partial t} + u_j \frac{\partial u_i}{\partial x_j}) - [(T - T_{ref})]\vec{e}_z - \frac{\partial \tau_{ij}}{\partial x_j} = 0 \qquad (47)$$

$$\frac{\partial T}{\partial t} + u_j \frac{\partial T}{\partial x_j} - \frac{\partial^2 T}{\partial x_j^2} = 0. \qquad (48)$$

with,

$$\tau_{ij} = -P\delta_{ij} + \mu(\frac{\partial u_i}{\partial x_j} + \frac{\partial u_j}{\partial x_i}) \qquad (49)$$

This dimensionless form shows the proper balance between pressure, viscous forces and buoyant forces. Note that this dimensionless form may be readily implemented on any primitive-variable finite-element code (such as NACHOSII) by setting thermal conductivity and acceleration of gravity to 1, heat capacity and coefficient of thermal expansion to Pr, and density to 1/Pr.

This scaling is equivalent to matrix rescaling that has been used successfully in many applications, e. g., Koch (1985) used matrix scaling to reduce the condition number of relevant matrices by as much as five orders of magnitude. For a simplified example, suppose we have the following matrix system:

$$\begin{bmatrix} K & -Q & B \\ -Q^T & 0 & 0 \\ 0 & 0 & D \end{bmatrix} \begin{bmatrix} U \\ P \\ T \end{bmatrix} = \begin{bmatrix} F \\ 0 \\ G \end{bmatrix}.$$

where K and B have elements of greatly different sizes. To rescale them to the same order, let

$$|K| = |\lambda B|$$

which is the same as the change of variable

$$B^* = \lambda B$$
$$P^* = \frac{P}{\lambda}$$
$$T^* = \frac{T}{\lambda}.$$

This rescaling results in a system that has elements whose sizes are comparable which can be solved with less round-off error than the original system

$$\begin{bmatrix} K^* & -Q^* & B^* \\ -Q^{*T} & 0 & 0 \\ 0 & 0 & D^* \end{bmatrix} \begin{bmatrix} U^* \\ P^* \\ T^* \end{bmatrix} = \begin{bmatrix} F \\ 0 \\ G \end{bmatrix}.$$

The new scaling of equations (32)-(36) resulted in marked improvement in the performance of the FEM code over that with the Pr-Ra scaling by forcing the terms in the matrices representing pressure, buoyancy, and viscosity to be roughly the same size (Table 6). This scaling, therefore, minimized the possibility of round-

Table 6. Typical matrix norms for different scalings; mixed FEM, discontinuous P, Ra=6.5 X 10^6.

Scaling	Diffusion Matrix(K)	Buoyancy Matrix(B)	Discrete Divergence
Pr - Ra	~10^{-2}	~10^2	~10^{-10}
new scaling	~10^2	~10^2	~10^{-14}

off errors and provided an effective means of computing the solution.

4.8 Effects of Element Choice

When we discussed elements previously, we gave some criteria for choice based on the div-stability condition and the heuristic argument of mesh locking. From these criteria, we can conclude that all of the available elements have the same theoretical convergence properties, but that the elements with discontinuous pressure interpolation functions have better divergence-constraint properties.

The discrete divergence calculations confirm these characteristics (table 7). Note that these results were calculated using the mixed method (since penalty method requires discontinuous pressure interpolation) on a sample grid for the T_{amb} = 25C conditions. In both QUAD8 and QUAD9 elements, the discontinuous pressure approximation had a smaller discrete divergence than the continuous pressure approximation. Of these two elements, the one with the optimal value of r has the smaller discrete divergence. Note that this element does not satisfy the div-stability condition in the global sense, so while this condition is related to mass conservation, it is not sufficient to insure incompressibility. These results, as well as similar results in other ambient conditions, suggest the best available element to use for the plume calculation is the QUAD8 with linear, discontinuous pressure approximation.

Table 7. Effect of element choice on discrete divergence.

Element	r	Discrete Divergence
QUAD 8, disc P	2	$\sim 10^{-15}$
QUAD 8, cont P	6	$\sim 10^{-3}$
QUAD 9, disc P	2 2/3	$\sim 10^{-14}$
QUAD 9, cont P	8	$\sim 10^{-3}$

4.9 Solution Techniques

The choice of scaling and elements that was discussed in earlier sections kept

the discrete divergence to a minimum for the sample computations performed for

comparison. As the solution progressed in time, however, the discrete divergence

would often grow. Gradual growth was expected due to the larger values of speed

and accumulation of round-off error, but rapid growth served as a good indicator

that the solution would encounter an ill-conditioned matrix error, or that the

computed temperature and velocity would increase to unrealistically large values.

Four different methods were used in attempting to solve the plume problem.

The first two were already coded into the NACHOSII system; the code was modified

to accomodate two additional methods that were variations of the first two methods:

1. The integrated or mixed method

2. The penalty method

3. The Uzawa algorithm.

4. The mixed method using a multistep Newton method

The following paragraphs will report on the results using these methods. For

each method, many different tests involving various ambient conditions and

assumptions were performed. Additionally, several meshes and time steps were used for each problem. Before presenting the results for each of these methods, we will briefly describe the NACHOSII system.

4.9.1 The NACHOSII System

The finite-element code used to produce the numerical model is named NACHOSII. NACHOSII, written by D. Gartling (1986) at Sandia National Laboratories, is designed for planar or axisymmetric two-dimensional analysis of viscous, incompressible flows, including the effects of buoyancy and heat transfer. NACHOSII represents a significant improvement over its predecessor, NACHOSI. Enhancements include a wider choice of elements, interpolation functions, and time solution procedures. This flexibility provided a combination of factors that produced a more effective numerical model than that allowed by NACHOSI. Another key difference between NACHOSI and NACHOSII is that NACHOSII solves the momentum and energy equations as one system. NACHOSI solves each equation individually and then uses the solution to solve the remaining equation.

NACHOSII provides a choice of triangular or quadrilateral elements. The velocity and temperature are approximated by quadratic functions that are continuous between elements while the pressure is approximated by a linear function. The pressure may be continuous or discontinous between elements. The assembly of the global matrix equations is by the direct stiffness approach where the equations for nodes common to adjacent elements are added. The majority of the computational time is spent solving the nonlinear equation (43). NACHOSII uses the Newton method to linearize the equation by computing the Jacobian of the system. More details on the implementation of this method will be presented in section 4.9.5.

The Newton method and the FDM reduce the problem to a linear system that

is nonsymmetric (for the nonlinear Navier-Stokes problem) and indefinite. The solution method in NACHOSII is a special form of Gaussian elimination called the frontal solution method. This method combines the global matrix assembly process with Gaussian elimination so that unknowns are solved in the system as soon as the assembly for each element is completed. This combination minimizes the amount of memory used since only a portion of the global system is 'active' in main memory. For large problems, e. g., three-dimensional problems, iterative linear solvers (e. g. Conjugate-Gradient) are more efficient than Gaussian elimination. Since such iterative systems require the assembly of the global matrix first, no attempt was made to modify the frontal assembly process to allow the use of iterative solvers.

Besides in-house projects at Sandia, NACHOSII has been successfully used for the solution of a variety of problems. NACHOSII results compared favorably with FIDAP results in Gartling (1990). Koch and Yuen (1985) used a modified version of NACHOSI to model mantle convection.

4.9.2 The Integrated Method

Recall that this method solves the continuity equation as part of the global system of equations. Due to shortcomings in the method of solving the nonlinear system of equations (43), this method did not keep the discrete divergence small enough to allow an accurate solution. The problem with the method of solution will be addressed in section 4.9.5. Typically, the discrete divergence would remain small for a period of time, then increase sharply (usually by at least two orders of magnitude) before an error would occur. Figure 16 shows the change in discrete divergence for a case where $T_{amb} = 25C$ using the QUAD8 element with discontinuous pressure approximation. Following the large increase in discrete divergence at step 269, the temperature increased to an unrealistically large value. This variation in discrete divergence is even more pronounced in the $T_{amb} = 0.1C$ case.
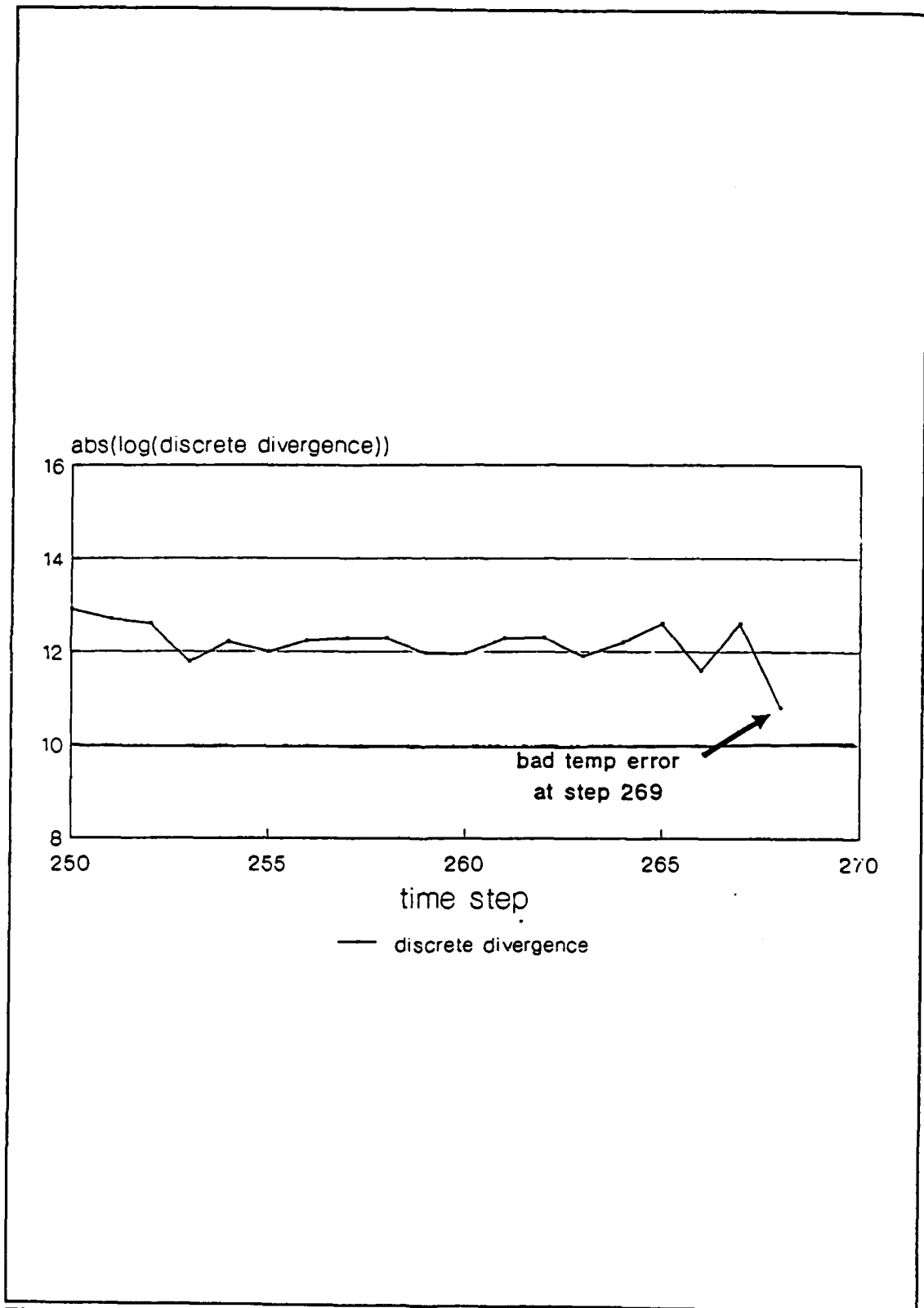
abs(log(discrete divergence))

bad temp error
at step 269

time step

— discrete divergence

Figure 16. Discrete divergence for mixed method.

4.9.3 The Penalty Method

Table 8. How e affects discrete divergence.

Penalty Parameter	Discrete Divergence
1.0×10^{-15}	$\sim 10^{-8}$
1.0×10^{-14}	$\sim 10^{-5}$
1.0×10^{-13}	$\sim 10^{-3}$

As discussed earlier, the penalty method uses a fixed parameter to approximate the incompressibility condition. The choice of this parameter is often difficult since choosing it too small will ill-condition the problem and choosing it too large will introduce too much compressibility into the solution. Table 8 illustrates how changing the penalty parameter will change the discrete divergence. Note that these calculations were for the $T_{amb} = 25C$ case using the dimensional form of the equations and a QUAD8 element with discontinuous pressure approximation; similar results (at smaller discrete divergences) hold for a properly scaled system. The method used to determine the appropriate penalty parameter was to make several sample runs and observe which number gave the best discrete divergence behaviour. As a result, early steps in the calculations showed great promise, but the discrete divergence would increase sharply at some point later in the calculation. When this increase occured, the solution soon encountered an ill-conditioning error. As a result of these errors, no simulation ran to the point of showing a liftoff of the ball. Figure 17 illustrates this performance for a case where $T_{amb} = 0.1C$ and $e = 1.0 \times 10^{-13}$ using a QUAD8 element with discontinuous presssure approxmation. The penalty method, however, did lower computing time when compared to the mixed method

since it solves a matrix system for fewer degrees of freedom. The penalty method

typically used about 35% less time than the mixed method on the same problem.

4.9.4 The Uzawa Algorithm

The Uzawa algorithm is a specific application of an augmented-Lagrangian

method to solve the minimized form of the plume problem. An augmented-

Lagrangian method adds an additional (or augmented) term to the momentum

equation. The advantage of this method is that, due to the presence of this

additional term, the exact solution of the Stokes problem may be found without

making the penalty term go to zero (with the resulting ill-conditioning). It contains

an iterative procedure that corrects the velocity field if the discrete divergence is

too large. Detailed theoretical background for this method, with applications for

Navier-Stokes equations may be found in Fortin and Glowinski (1983). Note that

they mention the application of the Uzawa algorithm to the time-dependent Navier-

Stokes problem, but they show no supporting calculations. In fact, no application

with supporting calculations for the time-dependent Navier-Stokes problem has been

found in the literature.

In the Uzawa method, the matrix equation (38) has an additional term:

$$M\frac{d\vec{U}}{dt}+C(\vec{U})\vec{U}-Q\vec{P}+K(\vec{U},\vec{T})\vec{U}+B(\vec{T})\vec{T}+\frac{1}{e}Q^TQ\vec{U} = F(\vec{T})$$

where the $1/e\ Q^TQ\vec{U}$ term is the augmented-Lagrangian term and the energy

equation is unchanged. e is a small constant that is usually called a penalty

parameter. This method has the same advantage as the penalty method in that it

eliminates pressure as an unknown in the matrix system and thus decouples velocity

and pressure. This decoupling reduces the size of the matrix system and saves

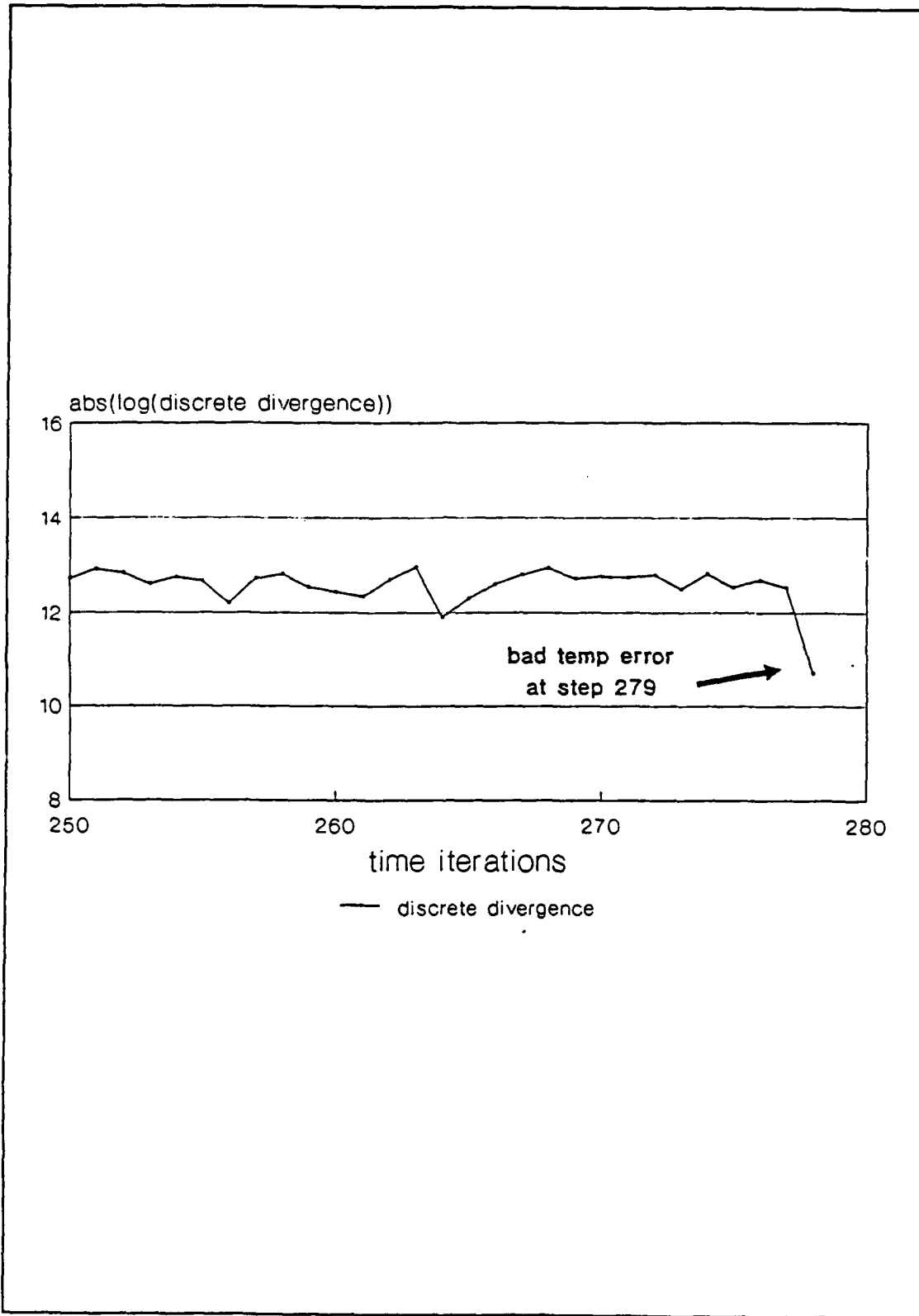memory and computing time. However, the pressure solution must be found

abs(log(discrete divergence))

bad temp error
at step 279

time iterations

— discrete divergence

Figure 17. Discrete divergence for penalty method.

iteratively. Now, to decouple U from P, start with an initial guess for P and solve

for U, then update P and solve again if the discrete divergence is too large, i. e.,

1. Given $\vec{P}^{n-1}$, solve for $\vec{U}^n$, $\vec{T}^n$

$$M\frac{d\vec{U}^n}{dt} + C(\vec{U}^n)\vec{U}^n - Q\vec{P}^{n-1} + K(\vec{U}^n,\vec{T}^n)\vec{U}^n + B(\vec{T}^n)\vec{T}^n + K_p\vec{U}^n = \vec{0}$$

$$N\frac{d\vec{T}^n}{dt} + D(\vec{U}^n)\vec{T}^n + L(\vec{T}^n)\vec{T}^n = \vec{0}$$

where

$$K_p = \frac{1}{\epsilon}QM_p^{-1}Q^T$$

$$M_p = \int_\Omega \vec{\Psi}\vec{\Psi}^T d\Omega.$$

2. Update

$$\vec{P}^n = \vec{P}^{n-1} + \frac{1}{\epsilon}M_p^{-1}Q^T\vec{U}^n$$

(This step is based on a perturbation to the continuity equation.)

3. If discrete divergence is too large repeat. (The traditional penalty method

occurs in the method when $P_o = 0$ and steps 2 and 3 are performed only once.)

Note that the augmented-Lagrangian theory supports this choice of the

additional term in the step 1 equation only for the linear Stokes problem, i. e., $C = D$

$= 0$. Since the linear problem can be expressed as an equivalent minimization

problem, the minimization theory indicates the appropriate choice of the extra term.

The nonlinear momentum and energy equations that describe the plume problem

have no known equivalent minimization form. Experience has shown, however, that

using the same additional term as the corresponding Stokes problem produces results

that are comparable to results using the mixed or integrated method (Cuvelier, et. al. (1986), Fortin and Glowinski (1983), Fortin and Fortin (1985)). This Uzawa method, incidentally, is not difficult to implement in most finite-element programs, since all of the component matrices are available.

The Uzawa algorithm seemed very promising, particularly in light of the excellent results shown by Pelletier, et. al. (1989). They stated that for small e, convergence of the discrete divergence values to $O(e)$ occurred with only one or two iterations in the Stokes flow problem that they solved. Rapid convergence is necessary for this method since the global system must be solved for each penalty iteration. Since this solution is the most expensive part of the solution, if more than two or three iterations are used, the cost advantages of the penalty method are lost.

Table 9. Sensitivity of Uzawa to changes in e.

e	Subiterations to convergence	Rate of Decrease in Discrete Divergence
1.0×10^{-13}	1	One order of magnitude per subiteration
3.0×10^{-13}	5-7	18% decrease per subiteration
1.0×10^{-12}	10	10% decrease per subiteration

Initial testing of the Uzawa algorithm showed very good results for short periods of time. The value of e greatly affected the performance of the algorithm. On a benchmark plume problem with a 15 X 20 grid and $\Delta t = .0003$ (50 steps) for the $T_{amb} = 25C$ parameters, $e = 1.0 \times 10^{-12}$ required ten iterations per time step to reduce the discrete divergence to $O(e)$. On the same problem, $e = 3.0 \times 10^{-13}$ required between 5 and 7 iterations per time step while $e = 1.0 \times 10^{-13}$ required only one iteration. This sensitivity is also reflected in the rate of convergence. When the $e =$

1.0×10^{-13} case required more than one iteration (after 100 time steps), only two or

three iterations were required since the discrete divergence decreased by roughly one

order of magnitude per iteration. In contrast, the $e = 3.0 \times 10^{-13}$ case saw a decrease

in discrete divergence of about 18% per iteration while the $e = 1.0 \times 10^{-12}$ case

droppped by about 18% per iteration . These results are summarized in table 9.

These observations are consistant with results reported by Pelletier, et al. (1989) and

Fortin and Glowinski (1983). The rapid convergence for small e also confirmed that

the coding modifications for the Uzawa algorithm were correct.

Extensive testing of the Uzawa algorithm for the plume problem, however,

consistently demonstrated that the performance deteriorated as time progressed.

Simulations that started with ony one or two Uzawa iterations per time step would

often required 4 or 5 after 100-200 time steps. A typical case was a simulation of the

$T_{amb} = 25C$ experiment on a 25 X 30 grid with $\Delta t = .01$. The first 70 time steps

usually required only one Uzawa iteration; only on 3 occasions were 3 iterations

used. The subsequent 50 time steps, however, required 5 or 6 iterations per time step.

Table 10. Change in convergence rates in Uzawa.

Time Step	Subiteration	Discrete Divergence
100	1	6.944×10^{-10}
	2	6.051×10^{-13}
150	1	3.656×10^{-8}
	2	6.218×10^{-10}
	3	3.992×10^{-10}
	4	3.921×10^{-10}
	5	3.920×10^{-10}
	6	3.856×10^{-10}

This excessive number of Uzawa iterations makes this method less efficient than the integrated FEM. For this case, 120 steps using the Uzawa algorithm required 48 minutes of cpu time; the identical case ran 500 steps using the integrated method in just 68 minutes. Table 10 illustrates how the rate of convergence changes as the time integration progresses. Note that these results are for another sample case where a 15 by 20 grid was used for the $T_{amb} = 0.1C$ case and $e = 1.0 \times 10^{-13}$. These results are presented graphically in figure 18. Since the convergence was highly dependent on the choice of e, and a single, acceptable value for e was never determined. These results coincide with comments made by Fortin and Glowinski (1983) for similar nonlinear problems. Without an adequate choice of e, the convergence was too slow to be economical when compared with the mixed method. These poor results led to abandonment of this technique as described here. Other similar methods, perhaps involving an automatic choice of e, may be more effective in the future.

4.9.5 Multistep Newton Method

NACHOSII uses Newton's method to solve the nonlinear system of algebraic equations that are formed in the FEM (equation (43)). Newton's method gives quadratic convergence to the solution provided that the initial guess is close enough to the solution. Since NACHOSII uses a predictor/corrector type time integration (either forward/backward Euler or Adams-Bashforth/trapezoid integration), the predicted solution value will generally be close to the correct solution for each time step. This assumption provides the basis for NACHOSII to use a one-step Newton method for the solution of the nonlinear system. This method is justified, with examples given, in Gresho, Lee, and Sani (1980).

The modification made to NACHOSII is a simple extension of the base logic. After the first Newton iteration, the discrete divergence is used as a test of convergence. If the discrete divergence is too large, complete another Newton

abs(log(discrete divergence))

5-6 subiterations per time step

1-2 subiterations per time step
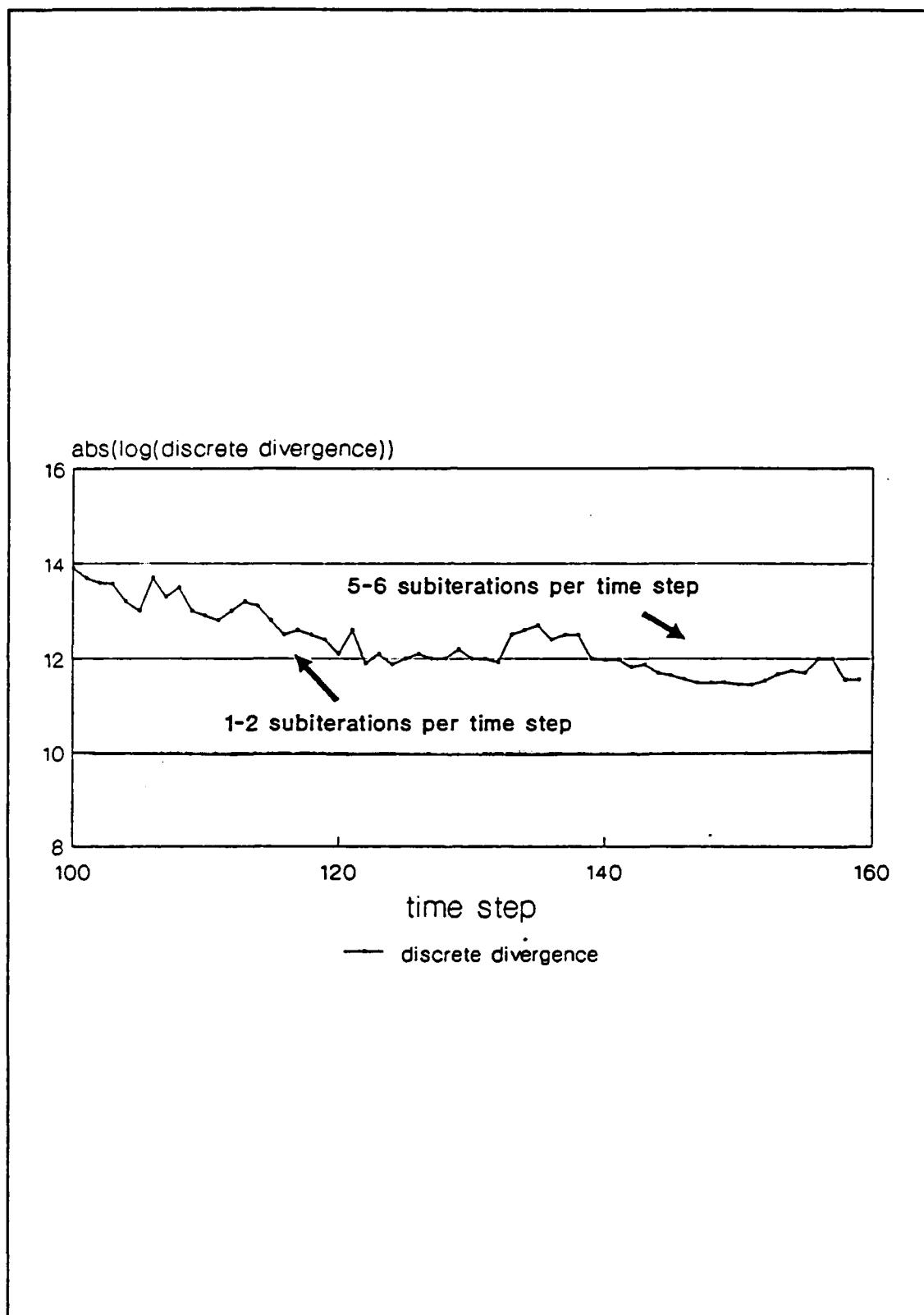
time step

—— discrete divergence

Figure 18. Discrete divergence for Uzawa method.

iteration and check the divergence again. Repeat until the discrete divergence is small enough.

This method gave acceptable results, as reported in the next section. Since most time steps normally required only one Newton iteration, the additional cost was not significant compared to the original one-step Newton method. Typically, those time steps requiring additional Newton iterations needed only two or three iterations to reduce the discrete divergence to a small value. A plot of discrete divergence versus time for this method is given in figure 19 for a 15 X 50 grid in the $T_{amb} =$ 0.1C case. Table 11 illustrates the rate of convergence for this method when multiple subiterations per time step are required.

4.10 Application to Plume Problem

The arguments and computational data presented above suggested that the

Table 11. Typical convergence for multistep Newton method.

Subiteration	Discrete Divergence
1	3.31×10^{-9}
2	3.81×10^{-12}

best approach available for solving the plume problem was to use a QUAD8 element with discontinuous pressure approximation in a mixed FEM that employed a multistep Newton method to solve the nonlinear matrix problem. The goal of this numerical work was to develop a model that would predict the laboratory plume behavior. The following results will show that this method gave a very accurate prediction of the laboratory results.

4.10.1 Ambient Temperature = 25C

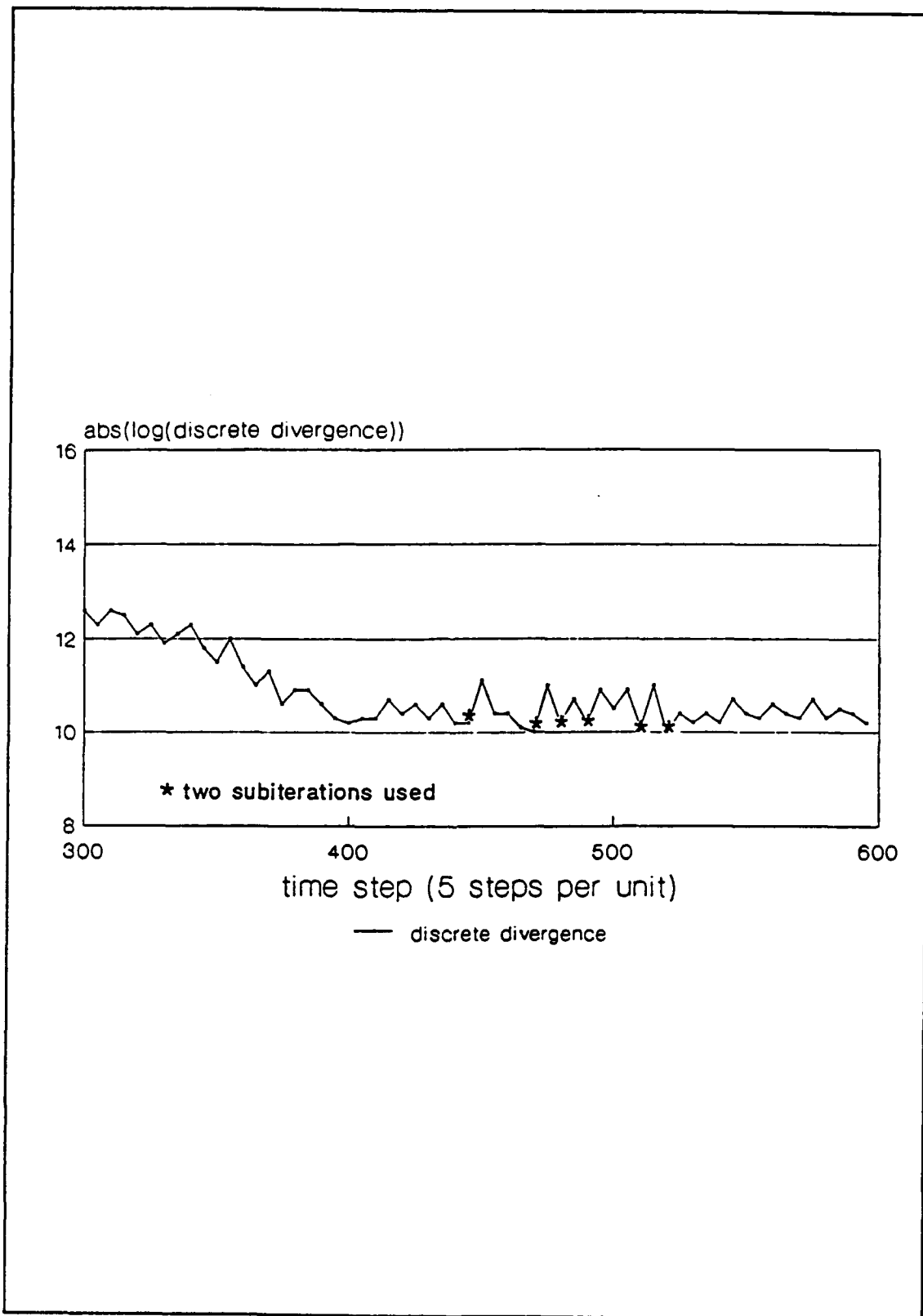The mesh used for the simulation was a 15 X 50 (figure 20a). The node

Figure 19. Discrete divergence for multistep method.

spacing in the radial direction was most dense near the axis of the heater; the node spacing in the height direction was even. For all cases, the maximum element size and time step was determined by the fundamental length and time scales used or the problem. Based on the theoretical accuracy of the FEM, these choices also insured that the numerical resolution was greater than the error in the experimental measurements. The heater was represented by specifying the heat flux along the bottom of the first four elements. Euler time integration (forward Euler predictor/backward Euler corrector) was used early in the problem since its damping characteristics removed temporal oscillations in the solution during the rapid heater initiation (the trapezoid method, in contrast, has no damping characteristics). Smaller time steps were used during this time due to the reduced accuracy of Euler integration compared to trapezoidal integration. Later in the problem, larger time steps were used when the second-order time integration method (Adams-Bashforth predictor/trapezoid corrector) was used.

The best tool for plume visualization is temperature contours, or isothermal lines. Some typical plots are given in figure 20b. These plots also provide the most effective way to compare the numerical results with the experimental results. Figure 20c shows the results of plotting the height versus time for the top of the ball for the experimental data (top plot) and the numerical results (bottom plot). For this plot, the top of the plume was defined by the T = 25C contour. The numerical plot is shifted later in time when compared to the experimental plot due to the slower heater start-up. Note that both plots display a relatively constant speed throughout most of the flight. For the experimental data, this average speed is .055 cm/sec; for the numerical simulation, this average speed is .056 cm/sec. These results agree within the error tolerance of the experimental data.

4.10.2 <u>Ambient Temperature = 0.1C</u>

A 15 X 50 mesh similar to the T_{amb}=25C case was used for this case (figure 21a). Note that the grid is placed on the same physical dimensions as the T_{amb} = 25C grid. The coordinate values are different due to the change in the length scaling. The element spacing in the radial direction is different from the T_{amb} = 25C case. This spacing was chosen to place smaller elements near the border of the larger ball. The same time-integration approach was used for this case also. The only difference between this case and the previous case was in the heater start-up. A time-dependent heat flux boundary condition was used along the bottom of the first three elements. The heat flux was increased gradually over a time period of 1.3 hours to the full power used in the experiment. This gradual increase, along with the damping from the Euler time integration, smoothed large temporal oscillations in the early steps of the solution. This slow heating also shifted the plots of height versus time further apart than in the T_{amb}=25C case (figure 21c). For this plot the top of the plume was defined by the T = 15.4C contour. The average speed results, however, agree to within experimental accuracy--the speed of the experiment was .0055 cm/sec and the numerical results gave .0053 cm/sec. Figure 21b shows typical temperature contour plots.

4.10.3 Ambient Temperature = -26.1C

No successful runs were completed for this case. The difference between the size of the terms of the global matrix corresponding to viscous forces (matrix K in equation (42)) created too much round-off error and let to ill-conditioning errors in the solution. This difference is not due to scaling as discussed earlier, but due to the wide variance in the value of viscosity between fluid inside and outside the plume. The difference was as high as 10^7 for this case.

A method that may have promise for resolving this problem in the future has been suggested by Pelletier et. al. (1989). They suggested scaling the matrix

equations on an element level. This scaling could show a similar improvement as the global scaling of the full equations did in the earlier discussion.
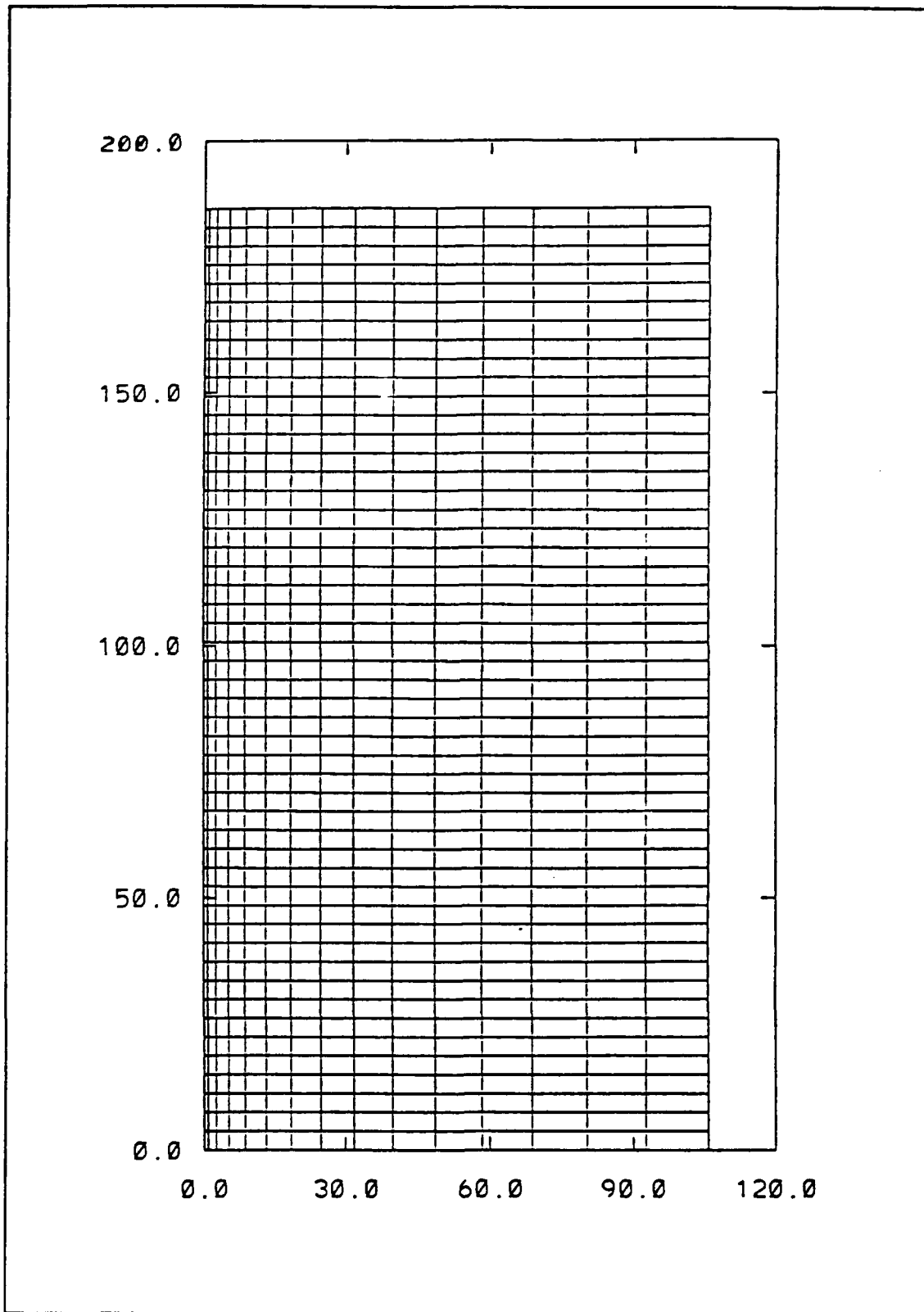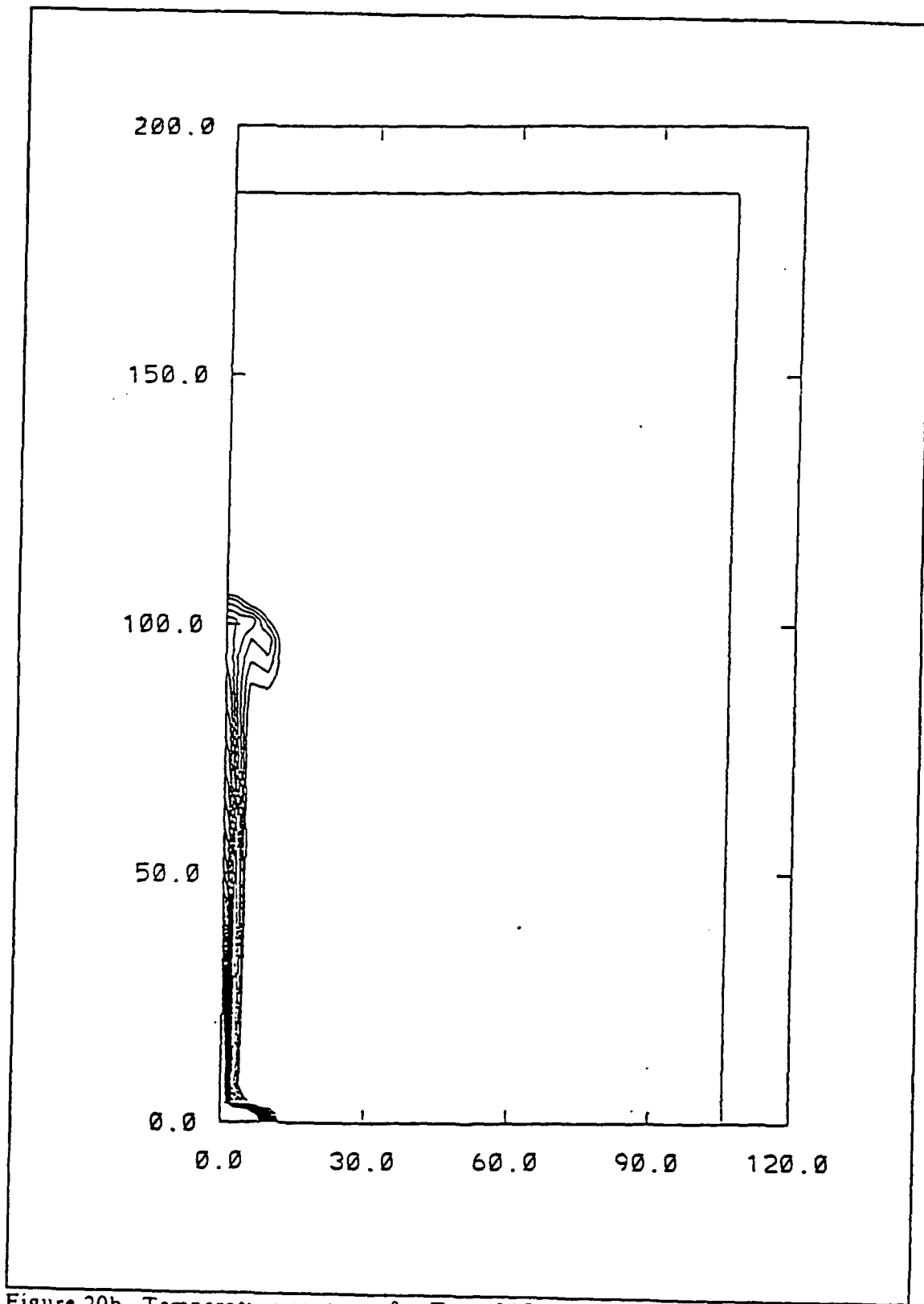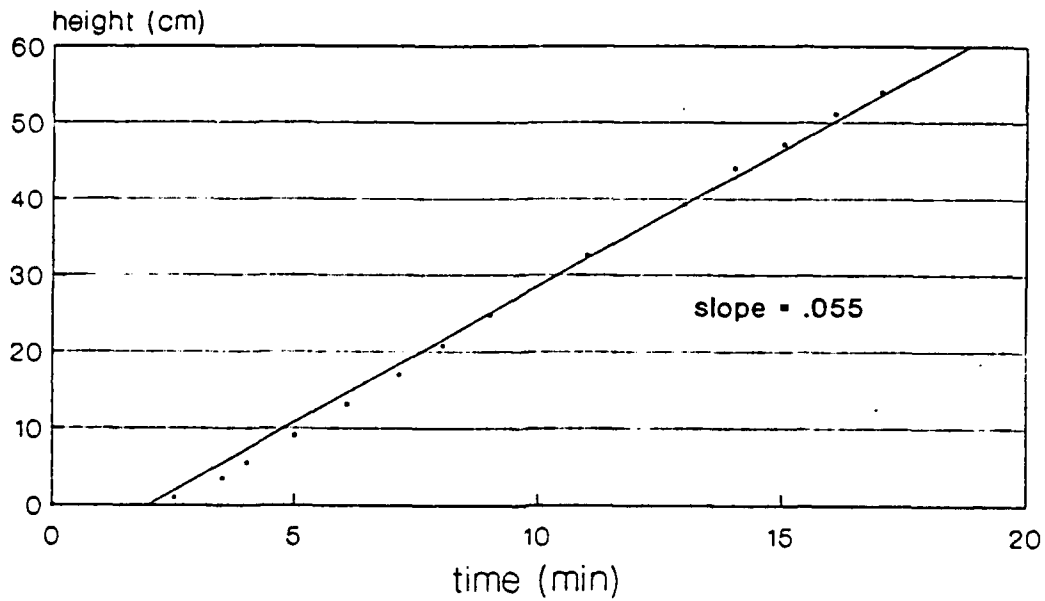
Figure 20a. Grid used in T_{amb}=25C case.

Figure 20b. Temperature contours for T_{amb}=25C case, time=15.7 minutes.

Experimental Result

Numerical Result

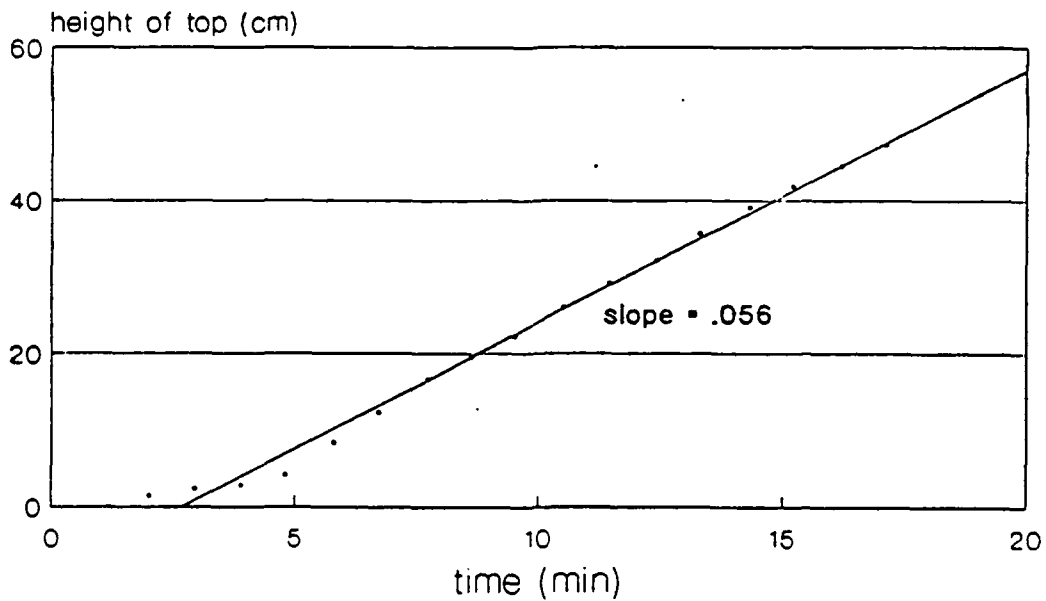Figure 20c. Results for T_{amb}=25C case.
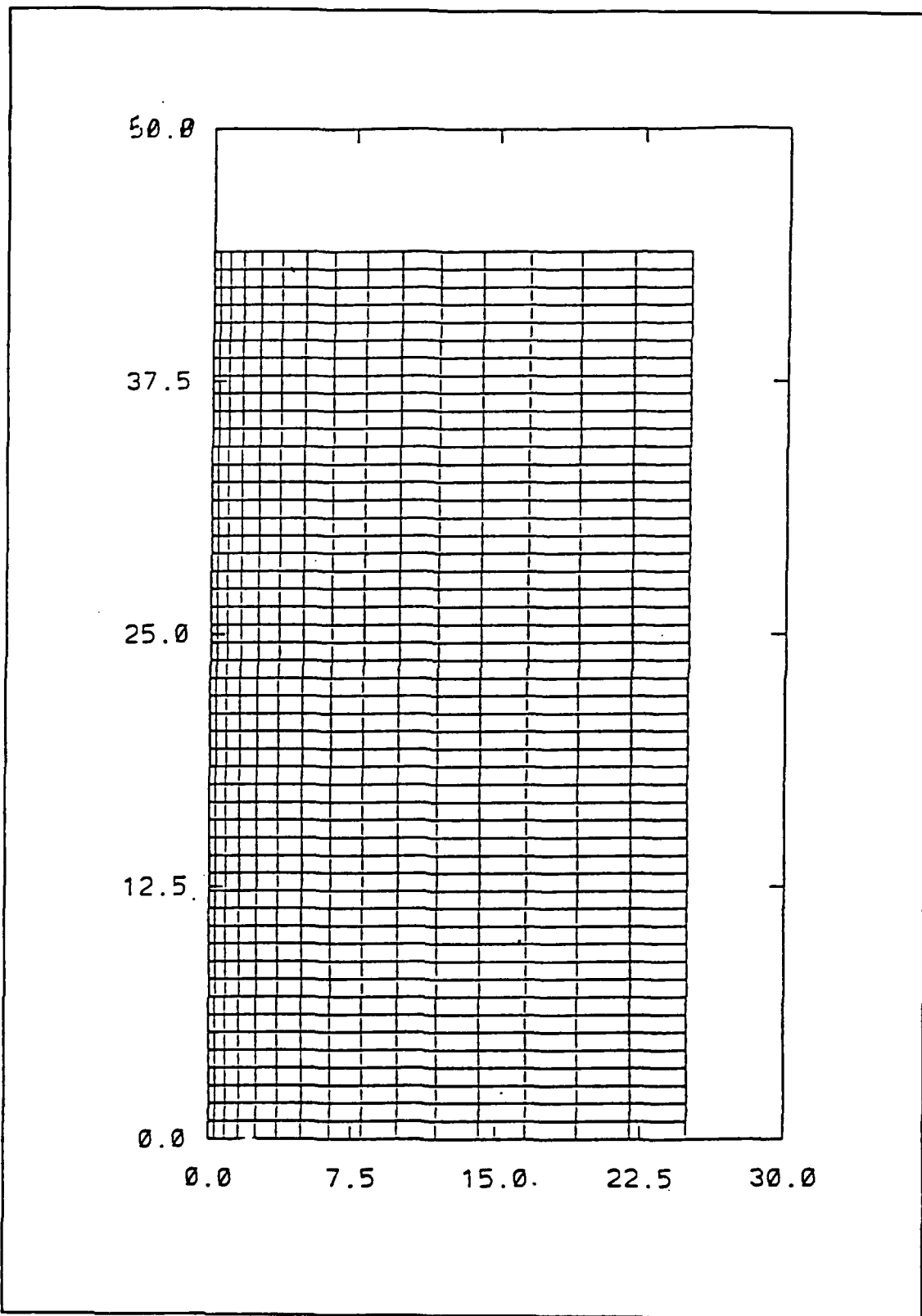
Figure 21a. Grid used for $T_{amb}=0.1C$ case.

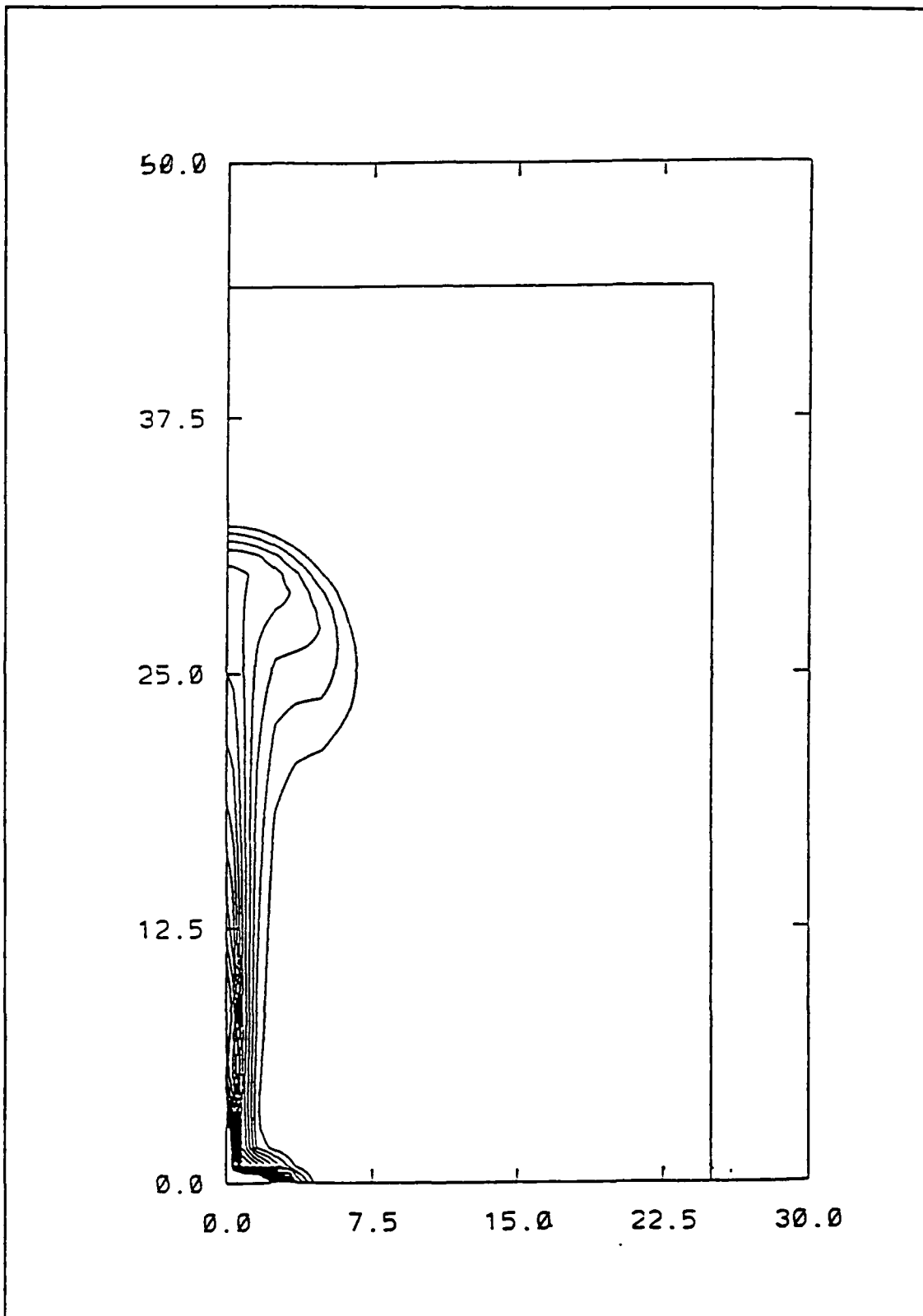Figure 21b. Temperature contours for $T_{amb}=0.1C$ case, time=3.1 hours.

Experimental Result

height(cm)

slope = .0055

time(min)

Numerical Result
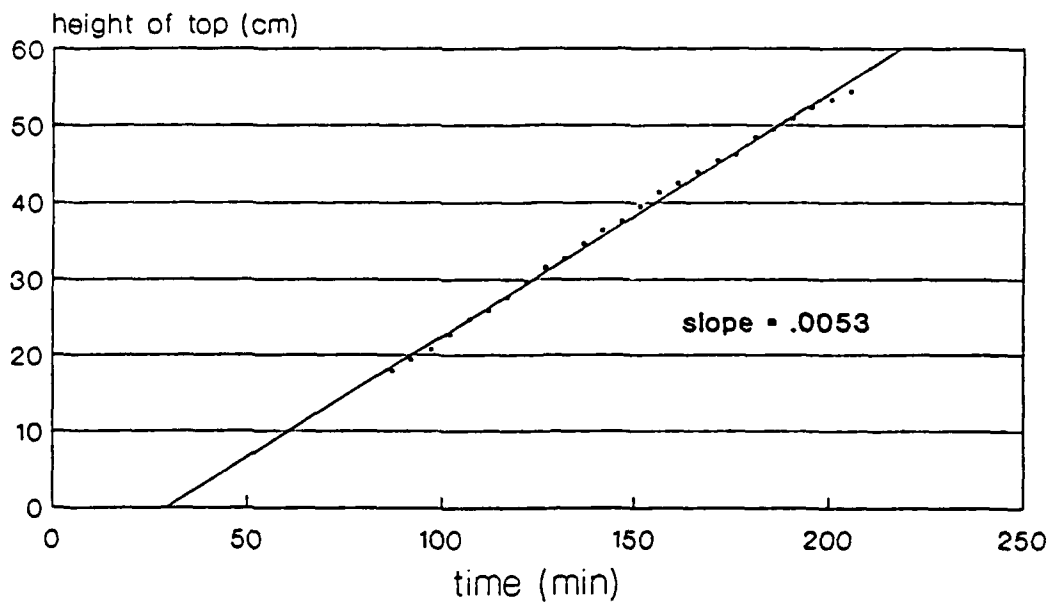
height of top (cm)

slope = .0053

time (min)

Figure 21c. Results for T_{amb}=0.1C case.

CHAPTER 5

SUMMARY AND CONCLUSIONS

5.1 Experimental Study

The experiment described in chapter 2 explored the interaction of buoyancy and diffusion at higher viscosity contrasts than earlier studies. Although the method of plume generation (heater) differed from the related experiment (injection of warmer fluid) of Griffiths and Campbell (1990), the plume structure appears to be dynamically similar to their results. The experiment, then, may be viewed as an extension of their work to larger viscosity contrasts.

The results of the experiment (figures 4a, 5a, and table 3) demonstrated that previous analytical models are inadequate for describing the motion of the ball. The flow structure of the T_{amb} = -26.1C case (figure 6b) suggested that heat loss from the ball is an important factor that may account for some of the discrepancies in the earlier models.

Two improvements in the experimental apparatus and procedure would make the study more effective. First, a more powerful heater would provide the ability to study the effects of heater power on the plume structure and speed. The heater used in the experiment of chapter 2 required full power to produce the tracer bubbles. Second, accurate temperature measurements would improve the utility of the results markedly. Measurement of the temperature of the heater surface would indicate what rate of heater startup should be used in the numerical model. The temperature

on the ball perimeter would indicate which temperature contour in the numerical

model to use to mark the plume boundary. These improvements would allow for

more accurate comparison of the experimental results with the numerical model.

5.2 Analytical Modelling

The efforts in analytical modelling focused on refining the Griffiths and

Campbell (1990) model by adding the effects of thermal detrainment. The relative

amount of mass entrainment and heat loss was varied by introducing a heat loss term

that depends on a parameter β. For all finite values of this parameter, the new

model is more effective in modelling the experiment than previous models.

The next steps in improving the analytical model will involve relaxing the

assumption that heat loss in the conduit is negligible and refining the relationship

between the entrained fluid layer and the thermal boundary layer. Calculations of

heat flux from the numerical models suggest that the heat loss in the conduit may be

as large as 30% of the heat loss from the ball. This percentage will increase as the

conduit length grows. Adding this effect to the energy equation in chapter 2 will

improve the accuracy of the model, particularly for longer flight times. Recall that

to develop the relationship in equation (16), we assumed a linear temperature profile

through the thermal boundary layer. Making this profile more realistic will result in

algebraic complication, but may also improve the model.

5.3 Numerical Modelling

By reducing the round-off error and using the discrete-divergence as a

diagnostic to choose the best element/interpolation combination, numerical results

that agreed with the experimental data to within the experimental errors were found

for two experimental cases by making a small modification to the nonlinear matrix

solution procedure. In the T_{amb} = 0.1C case, the viscosity contrast of 10^5 was higher than in previous numerical studies of plumes. These improvement, however, did not allow successful simulation of the T_{amb} = -26.1C case due to the large differences in the magnitude of elements of the diffusion matrix K because of the large viscosity differences.

The successful simulations in the T_{amb} = 25C case and the T_{amb} = 0.1C case will serve a benchmark runs for future improvements in the method of numerical solution. Improvement efforts will concentrate on modelling larger viscosity contrast and in making the solution more efficient. The use of element matrix scaling may reduce the large discrepancies in the size of the elements of the diffusion matrix. A more sophisticated augmented-Lagrangian method may reduce the computational time required for the problem. Finally, since we know roughly where the large temperature gradients are as the plume develops, some method of moving a fine grid with the ball and neck would reduce computational time significantly.

An improved numerical model will allow more detailed applications of numerical experiments in wider parameter ranges than the laboratory allowed. For example, running a numerical simulation in a taller tank will help determine if the new analytical model continues to work well for long flight paths. By developing better flow visualization tools for this problem (e. g., some way of indicating streak lines), we should be able to find a way to measure the relationship between the thermal and fluid boundary layers, and thus determine β from numerical experiments. The overall goal of the future application of an improved numerical model is to simulate mantle plumes and thus test the analytical results in this case.

APPENDIX

FINITE-ELEMENT EQUATIONS FOR THE THERMAL PLUME PROBLEM

Substitute the interpolation expressions for velocity, pressure and temperature into the governing equations (32) - (36).

Momentum:

$$\rho\left(\bar{\Phi}^T(x_i)\frac{\partial \bar{u}_i}{\partial t} + \bar{\Phi}^T(x_i)\bar{u}_j\frac{\partial \bar{\Phi}^T}{\partial x_j}\bar{u}_i\right) = -\frac{\partial \bar{\Psi}^T}{\partial x_j}\bar{P}$$
$$+ \frac{\partial}{\partial x_j}\left(\mu\left(\frac{\partial \bar{\Phi}^T}{\partial x_j}\bar{u}_i + \frac{\partial \bar{\Phi}^T}{\partial x_i}\bar{u}_j\right)\right) - \rho g_i \alpha(\bar{\Theta}^T\bar{T} - \bar{T}_{ref}) \tag{A1}$$

Continuity:

$$\frac{\partial \bar{\Phi}^T}{\partial x_i}\bar{u}_i = 0 \tag{A2}$$

Energy:

$$\rho c_p\left(\bar{\Theta}^T(x_i)\frac{\partial \bar{T}}{\partial t} + \bar{\Phi}^T(x_i)\bar{u}_i\frac{\partial \bar{\Theta}^T}{\partial x_i}\bar{T}\right) = \frac{\partial}{\partial x_i}\left(k\frac{\partial \bar{\Theta}^T}{\partial x_i}\right) \tag{A3}$$

The Galerkin FEM minimizes the residuals by making them orthogonal to the interpolation functions. Take the inner product of equations (A1)-(A3) with the

interpolation functions to get

Momentum:

$$\left(\int_\Omega \rho \vec{\Phi} \vec{\Phi}^T d\Omega\right)\frac{\partial \bar{u}_i}{\partial t} + \left(\int_\Omega \rho \vec{\Phi} \vec{\Phi}^T \bar{u}_j \frac{\partial \vec{\Phi}^T}{\partial x_j}d\Omega\right)\bar{u}_i$$

$$+ \left(\mu \int_\Omega \frac{\partial \vec{\Phi}}{\partial x_j}\frac{\partial \vec{\Phi}^T}{\partial x_j}d\Omega\right)\bar{u}_i + \left(\int_\Omega \mu \frac{\partial \vec{\Phi}}{\partial x_j}\frac{\partial \vec{\Phi}^T}{\partial x_i}d\Omega\right)\bar{u}_j \qquad (A4)$$

$$- \left(\int_\Omega \frac{\partial \vec{\Phi}}{\partial x_i}\vec{\Psi}^T d\Omega\right)\vec{P} = \left(\int_\Omega \rho g_i \alpha \vec{\Phi}\vec{\Theta}^T d\Omega\right)(\vec{T} - \vec{T}_{ref})$$

$$+ \left(\int_\Gamma \vec{\Phi}^T \tau_{ij} n_j d\Gamma\right)$$

Continuity:

$$-\left(\int_\Omega \vec{\Psi}\frac{\partial \vec{\Phi}^T}{\partial x_i}d\Omega\right)\bar{u}_i = \vec{0} \qquad (A5)$$

Energy:

$$\left(\int_\Omega \rho c_p \vec{\Theta}\vec{\Theta}^T d\Omega\right)\frac{\partial \vec{T}}{\partial t} + \left(\int_\Omega \rho c_p \vec{\Theta}\vec{\Phi}^T \bar{u}_j \frac{\partial \vec{\Theta}^T}{\partial x_j}d\Omega\right)\vec{T}$$

$$+ \left(\int_\Omega k \frac{\partial \vec{\Theta}}{\partial x_i}\frac{\partial \vec{\Theta}^T}{\partial x_i}d\Omega\right)\vec{T} = \left(\int_\Gamma \vec{\Theta}q_i n_i d\Gamma\right). \qquad (A6)$$

In arriving at equations (A4)-(A6), we used the divergence theorem to reduce the second-order diffusion terms in (A1) to first-order terms plus a boundary integral.

We also allow the variable material properties in (A4)-(A6) to have explicit spatial variation within an element as follows:

$$\mu(x_p t) = \tilde{\Psi}^T(x_p)\hat{\mu}(t)$$

$$k(x_p t) = \tilde{\Psi}^T(x_p)\hat{k}(t)$$

$$\alpha(x_p t) = \tilde{\Psi}^T(x_p)\hat{\alpha}(t)$$

where Ψ is an interpolation function and the $\wedge$ quantities are vectors of nodal point material properties. Since the dependent variables are known at the nodes, this is an effective means of evaluating material property values.

The integrals in (A4)-(A6) may be evaluated via numerical quadrature to produce coefficient matrices for the following system:

Momentum and Continuity:

$$
\begin{pmatrix} M & 0 & 0 \\ 0 & M & 0 \\ 0 & 0 & M \end{pmatrix}
\begin{pmatrix} \dfrac{\partial \vec{u}_1}{\partial t} \\ \dfrac{\partial \vec{u}_2}{\partial t} \\ \dfrac{\partial \vec{P}}{\partial t} \end{pmatrix}
+
\begin{pmatrix} C_1(\vec{u}_1) + C_2(\vec{u}_2) & 0 & 0 \\ 0 & C_1(\vec{u}_1) + C_2(\vec{u}_2) & 0 \\ 0 & 0 & 0 \end{pmatrix}
\begin{pmatrix} \vec{u}_1 \\ \vec{u}_2 \\ \vec{P} \end{pmatrix}
$$

$$
+
\begin{pmatrix} 2K_{11} + K_{22} & K_{21} & -Q_1 \\ K_{12} & K_{11} + 2K_{22} & -Q_2 \\ -Q_1^T & -Q_2^T & 0 \end{pmatrix}
\begin{pmatrix} \vec{u}_1 \\ \vec{u}_2 \\ \vec{P} \end{pmatrix}
=
\begin{pmatrix} \vec{F}_1(\vec{T}) \\ \vec{F}_2(\vec{T}) \\ \vec{0} \end{pmatrix}.
$$

(A7)

Energy:

$$N\frac{\partial \vec{T}}{\partial t} + [D(\vec{u}_1) + D(\vec{u}_2)]\vec{T} + [L_{11} + L_{22}]\vec{T} = G(\vec{T})$$

(A8)

where

$$M = \int_\Omega \rho \, \bar{\Phi} \, \bar{\Phi}^T d\Omega$$

$$C_i(\vec{u}_i) = \int_\Omega \rho \, \vec{\Phi} \, \vec{\Phi}^T \vec{u}_i \frac{\partial \vec{\Phi}^T}{\partial x_i} d\Omega$$

$$K_{ij} = \int_\Omega \vec{\Psi}^T \hat{\mu} \frac{\partial \vec{\Phi}}{\partial x_i} \frac{\partial \vec{\Phi}^T}{\partial x_j} d\Omega$$

$$Q_i = \int_\Omega \frac{\partial \vec{\Phi}}{\partial x_i} \vec{\Phi}^T d\Omega$$

$$\vec{F}_i(\vec{T}) = \int_\Omega \rho g_i \vec{\Psi}^T \hat{\alpha} \, \vec{\Phi} \vec{\theta}^T d\Omega (\vec{T} - \vec{T}_{amb}) + \int_\Gamma \vec{\Phi}^T \tau_{ij} n_j d\Gamma$$

$$N = \int_\Omega \rho c_p \vec{\theta} \vec{\theta}^T d\Omega$$

$$D_i(\vec{u}_i) = \int_\Omega c_p \vec{\theta} \vec{\Phi}^T \vec{u}_i \frac{\partial \vec{\theta}^T}{\partial x_i} d\Omega$$

$$L_{ij} = \int_\Omega \vec{\Psi}^T k \frac{\partial \vec{\theta}}{\partial x_i} \frac{\partial \vec{\theta}^T}{\partial x_i} d\Omega$$

$$\vec{G} = \int_\Gamma \vec{\theta} q_i n_i d\Gamma$$

For this problem, if we separate the buoyancy expression from the general force

vector in F, we can write (A7) and (A8) as

$$M\frac{\partial \vec{U}}{\partial t} + C(\vec{U})\vec{U} - Q\vec{P} + K(\vec{U},\vec{T})\vec{U} + \vec{B}(\vec{T})\vec{T} = \vec{F}$$

$$-Q^T\vec{U} = \vec{0}$$

$$N\frac{\partial \vec{T}}{\partial t} + D(\vec{U})\vec{T} + L(\vec{T}) = \vec{G}(\vec{T},\vec{U})$$

where

$$\vec{U}^T = (\vec{u}^T_{1},\vec{u}^T_{2})$$

and

$$\vec{B}(\vec{T}) = \int_{\Omega} \rho g_i \vec{\Psi}^T \hat{\alpha} \, \vec{\Phi}\vec{\Theta}^T d\Omega(\vec{T} - \vec{T}_{amb})$$

REFERENCES

Ansari, A., and Morris, S., 1985. The effects of strongly temperature-dependent viscosity on Stoke's drag law: experiments and theory. JFM, 159: 459-476.

Boss, A. P., and Sacks, I. S., 1985. Formation and growth of deep mantle plumes. Geophy. J. Roy. Astr. Soc., 80: 241-255.

Carey, G., and Oden, J., 1983. Finite Elements, a Second Course, Volume II. Prentice-Hall, New Jersey, 1983.

Cuvelier, C., Segal, A., and vanSteenhoven, A. , 1986. Finite Element Methods and Navier-Stokes Equations. D. Reidel, Dordrecht.

Daly, S. F., and Raefsky, A., 1985. On the penetration of a hot diapir through a strongly temperature-dependent viscosity medium. Geophy. J. Roy. Astr. Soc., 83: 657-681.

Fortin, M., and Fortin, A., 1985. A generalisation of Uzawa's algorithm for the solution of the Navier-Stokes equations. Comm. Appl. Numer. Methods, 1, 205-210.

Fortin, M., and Glowinski, R., 1983. Augmented Lagrangian Methods: Applications to the Numerical Solution of Boundary-Value Problems. North-Holland, Amsterdam.

Gartling, D. K., 1977. NACHOS - a finite element computer program for incompressible flow problems: part I -theoretical background and part II - User's Manual, SAND77-1334. Sandia Laboratories, Albuquerque, New Mexico.

Gartling, D. K., 1986. NACHOSII - a finite element computer program for incompressible flow problems: part I - theoretical background and part II- User's Manual, SAND86-1817. Sandia Laboratories, Albuquerque, New Mexico.

Gartling, D. K., 1990. A test problem for outflow boundary conditions--flow over a backward facing step. Int. J. Num. Meth. Fluids, 11, 953-967.

Girault, V. and Raviart, P., 1986. Finite Element Methods for Navier-Stokes equations. Springer-Verlag, Berlin.

Gresho, P., Lee, R., and Sani, R., 1980. On the time dependent solution of the incompressible Navier-Stokes equations in two and three dimensions. Recent advances in Numerical Methods in Fluids, Volume 1, Pineridge Press, Swansea, 27-81.

Griffiths, R. W., 1986a. Particle motions induced by spherical convective elements in Stokes flow. JFM, 166: 139-159.

Griffiths, R. W., 1986b. Thermals in extremely viscous fluids, including the effects of temperature-dependent viscosity. JFM, **166**: 115-138.

Griffiths, R. W., 1986c. The differing effects of compositional annd thermal buoyancies on the evolution of mantle diapirs. Phys. Ear. Plan. Int., **43**: 261-273.

Griffiths, R. W., 1986d. Dynamics of mantle thermals with constant buoyancy or anomalous internal heating. Earth Plan. Sci. Ltrs., **78**: 435-446.

Griffiths, R. W., and Campbell, I. H., 1990. Stirring and structure in mantle-starting plumes. Ear. Plan. Sci. Ltr., **99**: 66-78.

Gunzburger, M. D., 1989. Finite Element Methods for Viscous Incompressible Flows. Academic Press, Boston.

Happel, J., and Brenner, H. 1983. Low Reynolds Number Hydrodynamics. Martinus Nijhoff Publishers, The Hague.

Hughes, T. J. R., 1987. The Finite Element Method. Prentice-Hall, Englewood Cliffs, New Jersey.

Jarvis, G. T., and Peltier, W. R., 1982. Mantle convection as a boundary layer phenomenon. Geophy. J. Roy. Astr. Soc. , **68**: 385-424.

Jarvis, G. T., 1984. Time-dependent convection in the Earth's mantle. Phys. Ear. Plan. Int., **36**: 305-327.

Koch, M. and Yuen, D. A., 1985. Surface deformation and geoid anomalies over single- and double-layered convection systems. Geophy. Res. Ltr., **12**, 701-704.

Koch, M., 1985. A theoretical and numerical study the determination of the 3-D structure of the lithosphere by linear and nonlinear inversion of teleseismic travel times. Geophy. J. Roy. Astr. Soc., **80**, 73-93.

Loper, D. E., 1984. Structure of the core and lower mantle. Adv. Geophy., **26**: 1-34.

Morgan, W. J., 1971. Convection plumes in the lower mantle. Nature, **230**: 42-43.

Morris, S., 1982. the effects of a strongly temperature-dependent viscosity on slow flow past a hot sphere. JFM, **124**: 1-26.

Olson, P., and Singer, H., 1985. Creeping Plumes. JFM, **158**:511-531.

Olson, P., Schubert, G., and Anderson, C., 1987. Plume formation in the D'-layer and the roughness of the core-mantle boundary. Nature, **327**: 409-413.

Parmentier, E. M., Turcotte, D. L., and Torrance, K. E., 1975. Numerical experiments on the structure of mantle plumes. JGR, **80**: 4417-4424.

Pelletier, D., Fortin, A., and Camarero, R., 1989. Are FEM solutions of incompressible flows really incompressible? (or how simple flows can cause headaches!). Int. J. Num. Meth. Fluids., **9**, 99-112.

Ribe, N. M., 1983. Diapirism in the Earth's mantle: experiments on the motion of a hot sphere in a fluid with temperature dependent viscosity. J. Volcanol., 16: 221-245.

Sato, A., and Thompson, E. G., 1976. Finite element models for creeping convection. J. Comp. Phys., 22: 229-244.

Schubert, G., and Anderson, C. A., 1985. Finite element calculations of very high Rayleigh number thermal convection. Geophy. J. Roy. Astr. Soc., 80: 575-601.

Sod, G., 1985. Numerical Methods in Fluid Dynamics. Cambridge University Press, Cambridge.

Stacey, F. D., and Loper, D. L., 1983. The thermal boundary-layer interpretation of D" and its role as a plume source. Phys. Ear. Plan. Int., 33: 45-55.

Strikwerda, J., 1989. Finite Difference Schemes and Partial Differential Equations. Wadsworth and Brooks, Pacific Grove, California.

Turcotte,D. L., Torrance, K. E., and Hsui, A. T., 1973. Convection in the Earth's mantle. Meth. Comp. Phys., 13: 431-454.

Whitehead, J. A., and Luther, D. S., 1975. Dynamics of laboratory diapir and plume models. JGR, 80: 705-717.

Whitehead, J. A., 1986. Buoyancy-driven instabilities of low viscosity zones as models of magma rich zones. JGR, 91: 9303-9314.

Yuen, D. A., and Peltier, W. R., 1980. Mantle Plumes and the thermal stability of the D" layer. Geophy. Res. Ltr., 7: 625-628.

Zhao, W., and Yuen, D. A., 1987. the effects of adiabatic and viscous heating on plumes. Geophy. Res. Ltr., 14: 1223-1226.

BIOGRAPHY

David Coulliette was born and raised in northwestern Florida. He graduated from Escambia High School in Pensacola, Florida in 1977. He received a B. A. degree in mathematics from Asbury College in 1981. Upon graduation from college, he received a commission in the United States Navy and served for four years as an instructor in the Navy Nuclear Power Program where he was designated a Master Training Specialist. During this assignment, he received a M. S. in mathematical sciences from the University of Central Florida. After transferring to the United States Air Force in 1985, he was assigned to the Defense Communications Agency in Washington, D. C. in support of the Joint Chiefs of Staff. During this assignment, he completed a redesign of the attrition analysis module for the mission planning system of the Tomahawk Cruise Missile. Upon selection in the Air Force Institute of Technology instructor program, he was assigned to duty as a student at Florida State University. His military decorations include the Defense Meritorious Service Medal.

David is married to the former Carol Weaver of Ocala, Florida. They have two children: Caitlin, age 4 and Caleb, age 4 months.